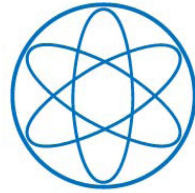


PHYSIK-DEPARTMENT



**Sputtered Tungsten Thin Films and
Composite Detectors for the Application
in the Dark Matter Experiments
CRESST and EURECA**

Diploma thesis

Sabine Roth



**TECHNISCHE UNIVERSITÄT
MÜNCHEN**

Physik-Department E15

19.09.2007

Abstract

Weakly Interacting Massive Particles (WIMPs) are candidates for non-baryonic Dark Matter. Their existence is presently well motivated from theoretical predictions as well as from indirect experimental observations (discussed in chapter 1). WIMPs are expected to interact only weakly or gravitationally. They are supposed to interact with baryonic matter via scattering off nuclei producing a nuclear recoil with energies of a few 10keV with a very low interaction rate of $\leq 10^{-6}$ events per kg of target material and day. The Dark Matter experiments CRESST (Cryogenic Rare Event Search with Superconducting Thermometers) and EURECA (European Underground Rare Event Calorimeter Array) are aimed at the direct detection of WIMPs with the help of very sensitive modularised cryogenic detectors. In chapter 2, the working principle of a cryogenic detector, the CRESST experiment itself and various techniques for background suppression are presented. The cryogenic detectors are equipped with transition edge sensors (TESs) made of tungsten. As a big target mass is required for the CRESST as well as for the EURECA experiment, reproducible production of these sensors is a major issue.

For the production of tungsten thin films that can be used as TESs for the CRESST and EURECA experiments, the rf-sputtering technique and the rf-deposition process have been investigated. The magnetron rf-sputtering facility as well as the applied rf-sputtering process are described in chapter 4.

The successful production of tungsten TESs for CRESST and EURECA requests special properties of the tungsten thin films in terms of their critical temperature (T_c) and the width of the transition from the super- to the normalconducting state. These properties of the grown tungsten thin film are strongly dependent on the lattice structure, the stress state of the crystal lattice, the growth mode (epitaxial or grained growth mode) and the inclusion of impurities. These dependencies of the superconducting transition are described in chapter 3 and are discussed together with the results obtained for the sputtered tungsten thin films (chapter 5). The produced films exhibit the required lattice structure, however, elevated transition temperatures in comparison to the expected one are observed. This difference could be successfully linked to the lattice structure properties and to the production process. Thus, several techniques and adjustments of the production parameters have been identified that are expected to lead to a decrease in temperature and to a narrower width of the transition.

The production of tungsten thin films using a shadow mask technique (chapter 6) together with a method of directly contacting the tungsten thin films make the application of postprocessing steps to the sputtered tungsten thin films, as ,e.g., structuring and etching processes, unnecessary. In this way an

uncontrolled influence on T_c is avoided.

In addition, these tungsten thin films make it possible to fabricate so-called composite detectors in large numbers with pretested TESs (chapter 7). The composite detector design (CDD), where a glueing technique is used to attach a separate small crystal substrate bearing the TES to the absorber crystal complies with the requirements, e.g. of the EURECA experiment, to decouple the TES production process from the choice of absorber material. Two composite detectors that were assembled using different glueing techniques, absorber materials and sizes are described and the results obtained from measurements with these two composite detectors are discussed. It can be deduced that the CDD exhibits a promising potential for the application to detectors for the CRESST and EURECA experiments.

On the basis of an existing thermal detector model for cryogenic detectors, an extension to this model, including the CDD, has been developed to further investigate and understand the performance of these composite detectors (chapter 8). With this extended model the observed signal shape of the composite detectors can be explained and described consistently. Thus, this extended model can be expected to provide an enormous help when tailoring composite detectors to the requirements of various experiments.

Contents

1	Introduction	1
1.1	Dark Matter	1
1.1.1	First Indications for Dark Matter	1
1.1.2	Baryonic and Non-Baryonic Dark Matter	2
1.1.3	The Cosmic Microwave Background Radiation and the Concordance Model	3
1.1.4	Observations of two Colliding Galaxy Clusters	4
1.2	Experimental Search for Dark Matter	5
1.3	Aim of the Present Work	8
2	The CRESST Experiment	9
2.1	Working Principle of Cryogenic Detectors	9
2.2	The CRESST Detectors	11
2.2.1	The CRESST Detector Module	12
2.2.2	The Phonon-Light Technique for Background Suppres- sion	12
2.2.3	The Phonon Detector	14
2.2.4	The Light Detector	15
2.2.5	Stabilisation of the Detectors	17
2.3	The CRESST Low-Background Setup	17
2.4	The CRESST Cryostat	18
2.5	Results of the CRESST Experiment	20
2.6	EURECA	23
3	Properties of Tungsten	25
3.1	General Properties of Tungsten	25
3.2	Properties of Bulk Tungsten	26
3.2.1	Bulk α -Tungsten	26
3.2.2	Bulk β -Tungsten	26
3.3	Properties of Tungsten Thin Films	27
3.3.1	Crystal Structure of Tungsten Thin Films	28
3.3.2	Thin Film α -Tungsten	29
3.3.3	Thin Film β -Tungsten	30
3.3.4	Thin Film γ -Tungsten	30
3.4	Superconductivity of Tungsten	30
3.5	Summary of Tungsten Properties	33

4	Experimental Setup of the RF-Sputtering Magnetron Facility	35
4.1	Working Principle	35
4.2	Description of the Facility	37
4.3	Operation of the Ion Source	39
4.3.1	Working Principle	40
4.3.2	Operation Parameters	42
4.4	Start-up of the Substrate Heater	44
4.5	The RF-Sputtering Process	45
5	Results and Properties of the Sputtered Tungsten Thin Films	49
5.1	Experimental Techniques	49
5.1.1	Contacting Tungsten Thin Films	49
5.1.2	$\vartheta - 2\vartheta$ Measurement	50
5.1.3	Residual Resistance Ratio (RRR) Measurement	50
5.1.4	Transition Temperature Measurement	51
5.2	Results	51
5.2.1	$\vartheta - 2\vartheta$ Measurements	52
5.2.2	Residual Resistance Ratio	54
5.2.3	Specific Resistivity	54
5.2.4	Transition Temperature	56
5.2.5	Summary of Properties of the Produced Tungsten Thin Films	58
5.3	Discussion	58
5.3.1	Production Parameters	58
5.3.2	Crystal Structure	59
5.3.3	Transition Temperatures	61
5.3.4	Conclusions	63
6	Production and Properties of "Small" Tungsten Thin Films	65
6.1	Motivation	65
6.2	Production	65
6.3	Results	66
6.4	Discussion	68
7	Composite Detectors	71
7.1	Composite Detector Design (CDD)	71
7.1.1	Basic Design	71
7.1.2	Advantages of the Application of the CDD	71
7.1.3	Setup of the Two Realised Composite Detectors	73
7.2	Composite Detector 1	76
7.2.1	Measurements	76
7.2.2	Results and Discussion	76
7.3	Composite Detector 2	77
7.3.1	Measurements	77

7.3.2	Results and Discussion	78
7.4	Conclusions	79
8	Thermal Detector Model for Composite Detectors	81
8.1	Basic Thermal Detector Model (BTDM)	81
8.1.1	Processes in the Absorber	81
8.1.2	Graphical Representation of the BTDM	82
8.1.3	Non-thermal and Thermal Phonons and Pulse Shape	83
8.2	Properties of the Investigated Composite Detectors	86
8.2.1	Setup of the Three Composite Detectors	87
8.2.2	The "TES-substrate - TES" system	87
8.2.3	Signal Shape Observed for the Investigated Composite Detectors	88
8.3	Thermal Detector Model for a Composite Detector (TDM-CD)	89
8.3.1	Processes in the Absorber	90
8.3.2	Graphical Representation of the TDM-CD	90
8.3.3	Propagation of Non-Thermal and Thermal Phonons	90
8.3.4	Case 1: Non-thermal Phonons from the Absorber	94
8.3.5	Case 2: Thermal Phonons from the Absorber	104
8.3.6	Conclusions	108
8.3.7	Future Experimental Tests of the Model	110
9	Summary and Outlook	113
	List of Figures	I
	List of Tables	VII
	Bibliography	XI

Chapter 1

Introduction

In the 1930s first evidence for the existence of what is referred to today as Dark Matter was discovered by F. Zwicky [1]. The Dark Matter problem still remains one of the most puzzling of present physics as no direct detection of Dark Matter particles has yet been possible.

1.1 Dark Matter

During the last 70 years many observations have been made that indicate the presence of Dark Matter in our universe. A first clue for the existence of much more matter than described in the Standard Model of Particle Physics, so-called non-baryonic Dark Matter, was provided by the observation of a discrepancy between measured and expected galactic rotation curves (see 1.1.1). Other strong hints were given by the interpretation of the Cosmic Microwave Background Radiation (CMBR) from the Wilkinson Microwave Anisotropy Probe (WMAP) data (see 1.1.3). Investigations of the evolution and formation processes of our universe have led to a model which is now widely accepted: the Concordance Model. Among other evidence for the existence of non-baryonic Dark Matter, one very recent observation will be presented in section 1.1.4: the interpretation of observations of 1E0657-558, a cluster merger at $z = 0.296$ that independently strengthens the hypothesis of the existence of Dark Matter without any assumptions regarding the nature of the gravitational force. The two colliding galaxy clusters and their gravitational potentials are presented.

1.1.1 First Indications for Dark Matter

In the early 1930s F. Zwicky [1] found that the measured orbital velocities of stars in the outer regions of eight spiral galaxies that he was observing in the Coma Cluster did not fit the expected values calculated on the basis of Kepler's third law and the Newtonian gravitational r^{-2} force law.

From Kepler's third law one would expect for the orbital velocities:

$$v_{\text{orb}}(r) = \sqrt{\frac{GM}{r}} \quad (1.1)$$

$$\Rightarrow v_{\text{orb}}(r) \sim r^{-\frac{1}{2}} \quad (1.2)$$

where:

- v_{orb} : orbital velocity
- r : radial distance to the galactic center
- G : gravitational constant
- M : visible (here: luminous) mass of the galaxy disc within r

Instead observations show that the rotation curves flatten out and indicate $v_{\text{orb}} \approx \text{const.}$ This behaviour could be explained by so-called Modified Newton Dynamics (MOND theories) which suggest that gravity on such large scales does no longer follow the Newtonian law [2] or that the particles response differs on large distances from the one on smaller scales [3]. Another explanation would be the existence of a non-luminous Dark Matter halo around the galaxy that accounts for the missing mass. Up to this point it was hardly possible to specify the nature of this Dark Matter.

In 1937 Zwicky was again confronted with a "missing mass problem" when he was investigating the properties of Nebulae and Nebulae Clusters in the Coma Cluster [4]. Comparing the expected light to mass ratio with the one he calculated using the virial theorem of classical mechanics¹ and the measured luminosity of the cluster he found a discrepancy in the order of two magnitudes (with today's value² of h inserted one would find a difference of a factor of ~ 50 [1]). This could either be explained by some unexpected property of the matter in the nebulae concerning its radiation (increasing the light to mass ratio) or again by the existence of some sort of matter that exhibits gravitational effects but could, however, not be detected by its luminosity.

1.1.2 Baryonic and Non-Baryonic Dark Matter

The question whether the Dark Matter in the halo of galaxies is of baryonic or non-baryonic nature was a long standing question. Many suggestions have been made, e.g. that the Dark Matter in the halo could be explained by the existence of brown dwarfs or white dwarfs, by neutron stars, faint stars or substellar objects in the mass range of $(10^{-7} - 10^{-2}) M_{\odot}$ (where M_{\odot} is the solar mass) [5]. To investigate this possibility of explaining the Dark Matter in the halo with the help of these so-called MACHOs (Massive Compact

¹The virial theorem gives the mass of the cluster in terms of the average square velocities of the nebulae constituting this cluster.

² h is a dimensionless parameter representing the observational uncertainty of the present Hubble expansion rate H_0 ; $h = \frac{H_0}{100 \text{ km s}^{-1} \text{ Mpc}^{-1}}$

Halo Objects) microlensing experiments (like the MACHO and EROS experiments) were performed [6]. In fact, substellar Dark Matter candidates and light stellar objects were ruled out. These microlensing observations in the end lead to an upper bound of the contribution of MACHOs (and therefore baryonic matter) to the Dark Matter in the galaxy halo of at most 5% [7].

Taking into account measurements of the primordial deuterium to hydrogen fraction together with the standard Big Bang Nucleosynthesis (BBN) calculations one is also able to put constraints on the total baryon density of the universe. This yields a fraction of $\sim 2\%$ [8] with respect to the total energy density of the universe which can be assigned to baryons. On the other hand, from observations of the magnitude versus redshift relation of Standard Candles one can estimate the total matter density of the universe to be larger by a factor of 5-8 [9], than the values obtained for the baryon density. Therefore, one can conclude that most of the matter in the universe is made up of non-baryonic matter.

1.1.3 The Cosmic Microwave Background Radiation and the Concordance Model

Another evidence for the existence of non-baryonic Dark Matter can be deduced from measurements and interpretations of the CMBR and from the resulting model of our universe, the Concordance Model. The CMBR was measured for the first time by Penzias and Wilson in 1964 - 1965 [10] exhibiting a temperature of $3.5 \pm 1.0\text{K}$ at 4080Mc/s, which, within the limits of their observations was isotropic, unpolarized and free from seasonal variations, thus confirming a Hot Big Bang Model of our universe. Only in 1992 temperature anisotropies (with an angular resolution of about 10 degrees) in the CMBR at a level of 10^{-5} were detected by the Differential Microwave Radiometers (DMR) experiment on the COBE satellite [11]. These anisotropies represent primordial fluctuations of the gravitational potential. Next generation observations as the satellite experiment WMAP have been able to measure the anisotropy so accurately that density fluctuations of the baryon-photon fluid that was exhibiting acoustic oscillations can be seen. From the peak positions and the peak amplitudes of the multipole expansion of these oscillations the parameters of the standard model of presentday cosmology, the Concordance Model (based on the isotropic and homogeneous Friedmann-Lemaître-Robertson-Walker model (FLRW model) [9]), could be evaluated to quite a good accuracy (see table 1.1.3).

The FLRW model is described by the Friedmann equation that is a function of the cosmological parameters H_0 , the Hubble parameter, η , the baryon to photon ratio during nucleosynthesis and Ω_{tot} , the total energy density of the universe, describing the time evolution of distances in the universe and hence its dependency on the total energy density of the universe, Ω_{tot} . Therefore, the value of Ω_{tot} controls whether the expansion rate of the universe is for-

ever accelerating ($\Omega_{\text{tot}} > 1$) or if we live in an possibly collapsing universe ($\Omega_{\text{tot}} < 1$). $\rho_{\text{crit}} = \frac{3H_0^2}{8\pi G}$ corresponds to the critical energy density separating these two models. In the presently accepted model of the universe it is assumed that $\Omega_{\text{tot}} \approx 1$, hence, $\Omega_{\text{tot}} \approx \rho_{\text{crit}}$.

There are three main contributions to the total energy density:

- $\Omega_M = \frac{8\pi G\rho_0}{3H_0^2}$, energy density due to matter
with $\Omega_M = \Omega_B + \Omega_{\text{CDM}}$, energy density due to baryons and Cold Dark Matter³ (CDM) respectively
- $\Omega_K = -\frac{k}{a_0^2 H_0^2}$, energy density due to curvature
- $\Omega_\Lambda = \frac{\Lambda}{3H_0^2}$, energy density due to Dark Energy

where, ρ_0 is the present matter density, G is the gravitational constant, k gives the curvature of space-time⁴, a_0 is the present value of the scale factor, describing the expansion of our universe and Λ is the cosmological constant, describing the contribution of so-called Dark Energy or vacuum energy to the total energy density of the universe. Of the Dark energy up to now almost nothing is known.

With these parameters one has been able to determine a Dark Energy Cold Dark Matter (Λ -CDM) model explaining the observed anisotropies of the CMBR and with this also consistently the structure formation processes in the early universe. Hot Dark Matter (HDM), for example neutrinos, was ruled out by structure formation arguments as it would not allow structures to be formed due to the "smearing out" of the HDM distribution.

From the CMBR measurements the parameters of the Concordance Model can be derived [12]. The density parameters, ρ_x ($x = M, K, \Lambda$), are expressed in terms of the critical density ρ_{crit} , where $\rho_{\text{crit}} = \frac{3H_0^2}{8\pi G}$ holds true. Therefore $\Omega_x = \frac{\rho_x}{\rho_{\text{crit}}}$.

1.1.4 Observations of two Colliding Galaxy Clusters

Recently another observation was made alluding to the existence of Dark Matter. Combining weak lensing observations of the cluster merger 1E0657-558 at $z = 0.296$ of two galaxy clusters with X-Ray and optical images obtained by the Chandra Telescope and the Hubble Space Telescope (ACS images), respectively, a direct evidence for the existence of Dark Matter could be found that is independent of assumptions regarding the nature of

³Hot Dark Matter (HDM) is ruled out, see the following discussion. For details concerning possible Cold Dark Matter candidates, see section 1.2.

⁴Today, the curvature term (k takes values in the range from -1 to +1) can be neglected as the fast expansion makes the universe look flat, nonetheless what value k takes. For a more detailed explanation, see [9].

Parameter	Value
$100\Omega_b h^2$	2.229 ± 0.073
$\Omega_M h^2$	$0.1277^{+0.0080}_{-0.0079}$
Ω_M	0.241 ± 0.034
H_0	$73.2^{+3.1}_{-3.2}$
Ω_Λ	0.716 ± 0.055
$\Omega_K h^2$	-0.014 ± 0.017
η	$6.116^{+0.197}_{-0.249}$
Age of the universe	$13.73^{+0.16}_{-0.15}$ Gyr

Table 1.1: Parameters of the Concordance Model (assuming a simple flat Λ -CDM model; values on the basis of the WMAP 3-year dataset) [12]

the gravitational force [13]. This system gives the unique chance of observing the involved baryonic matter spatially segregated from the inferred Dark Matter. The X-Ray emitting fluid-like plasma of the clusters, accounting for about 5-15% of the clusters' masses, is decelerated by the ram pressure due to the shock waves during the merging [14]. The stellar components, the galaxies (accounting for about 1-2% of the masses), interpenetrate each other collisionlessly. The masses of the stellar components and of the plasma are determined directly from X-Ray and optical images independently of any gravity or Dark Matter models. Thus, if a Dark Matter halo would not be present, the observed gravitational potential should trace the dominant mass components of the clusters which would then be the plasma distributions. In contrary to this, the gravitational potential reconstructed by weak gravitational lensing observations shows that the centres of mass of the two clusters do not coincide with the plasma clouds but are located near the BCGs (Brightest Cluster's Galaxies). Assuming the existence of "collisionless" Dark Matter halos these would trace the stellar component distributions and therefore explain the observed gravitational potential. In the alternative gravity models it is suggested that the lensing potential of a central peak is suppressed by a gas disc located between the the two subclusters. In addition to other contradictions to this model, Clowe et al. [13] claim that within the noise level of their reconstruction, the relative signal of such a disc should be clearly visible. However, in their reconstruction no evidence for such a central gas disc can be found and therefore these alternative gravity models can be ruled out. Therefore, the observation of the two colliding galaxy clusters can be referred to as a direct proof for Dark Matter.

1.2 Experimental Search for Dark Matter

As a result of the above mentioned observations and indications for the existence of Dark Matter, experiments all around the world are aimed at the

detection of Dark Matter and at the determination of the properties of these Dark Matter particles. From theory different well motivated Dark Matter candidates arise. As a first candidate light neutrinos were discussed, but, as described in section 1.1.3, these were ruled out in favour of CDM models. At the moment two possible Dark Matter candidates remain as favoured ones: the WIMP (Weakly Interacting Massive Particle), arising from the MSSM (Minimal Supersymmetric Standard Model), an extension of the Standard Model, and the Axion, providing a solution of the strong CP problem [8]. Both these candidates exhibit different properties. The WIMP which could be motivated as the Lightest Supersymmetric Particle (LSP) in the SUSY theory, a relic particle thermally produced in the early universe, should exhibit a mass of $O(GeV)$ to reproduce the mass density Ω_M . The WIMPs are expected to exhibit interaction cross sections comparable to the ones of the weak interaction [8, 15]. The coupling of these non-relativistic WIMPs has two terms, a scalar, spin-independent (SI) part and an axial spin-dependent (SD) part. Axions on the other hand, if existent, would have masses of $O(1eV)$ as they would be produced in a totally different way: they would result as the relaxation of the field energy of the axion field. They appear in the extension of the Standard Model through the Peccei-Quinn symmetry [8].

In the frame of this work only experiments searching for WIMPs will be given a short review (for a review on Axion search experiments see [16]). One can distinguish between two classes of Dark Matter experiments: direct and indirect search experiments.

The detection principle of indirect Dark Matter experiments is based on the detection of a possible self-annihilation signal of WIMPs from astrophysical objects like for instance neutrinos from the center of the earth or the sun, where Dark Matter may accumulate due to gravitational capture. In this context, the following experiments should be mentioned (for further description see e.g. [17]):

- the BESS95-97, BESS-98, AMS and Caprice experiments, searching for an antiproton signal
- the AMS detector on board of the ISS (International Space Station), searching for an antideuteron signal
- the HEAT detector, searching for a positron signal
- the EGRET detector and the HESS detector, searching for a gamma ray signal
- the SuperKamiokande, Bhaksan and Amanda experiments, searching for neutrinos from the earth and the sun

Also accelerator experiments as for example the LHC (Large Hadronic Collider) where WIMPs could possibly be produced and then detected via their

annihilation signal rank among the indirect search experiments. Currently, most of these experiments begin to enter the regime of the parameter space suggested by the MSSM.

The basis of direct detection experiments is the recoil signal of a WIMP-nucleon elastic scattering event in a suitable absorber material. The signal is recorded either by a heat, ionization or scintillation light signal of the target material. By measuring two of these signals at the same time it is possible to reject electron recoil events, such as γ induced background. To detect the expected signal with its very low interaction rate of $\sim 10^{-6}$ events $\text{kg}^{-1}\text{d}^{-1}$ [18], some major requirements for direct WIMP detectors are settled: a very low energy threshold ($\sim 10\text{keV}$ or lower) due to the small expected signal, a possibility for large target masses ($>10\text{kg}$) and a low particle background (therefore, minimal radioactive contamination of used materials and an experimental setup in an underground laboratory are required). Also active and passive shielding of the experiment are required to successfully suppress the background. In the following, a list of running experiments is given (without claim of completeness) that more or less fulfill these requirements (it was attempted to give the most recent data):

- HDMS, p-type Ge-Detector (202g), ionization detector (SI), 9.9kg·d exposure (2000) [19]
- IGEX, Germanium Detector (2.2kg), ionization detector (SI), 80kg·d exposure (2002) [20]
- GERDA (successor experiment of IGEX) [21]
- NAIAD, several NaI(Tl) crystals ($\sim 55\text{kg}$), scintillation detector with Pulse Shape Discrimination (PSD) (SI and SD), 15984.4kg·d exposure (2000-2003) [22]
- DAMA/NaI, NaI(Tl) crystals ($\sim 100\text{kg}$), scintillation detector / modulation rate detector (SI and SD), 107731kg·d exposure (1995-2002) [23]
- DAMA/LIBRA, NaI(Tl) crystals ($\sim 250\text{kg}$), scintillation detector / modulation rate detector (SI and SD), $\sim 1.5 \cdot 10^5\text{kg}\cdot\text{d}$ (03/2006-03/2007) [23]
- KIMS, 4 CsI(Tl) crystals (34.8kg), scintillation detector with statistical used PSD / modulation rate detector (ran in counting rate) (SI and SD), 3407kg·d exposure [24]
- CDMS, Ge and Si crystals (4kg Ge, 0.9kg Si), phonon and ionization detector (SI and SD), 430kg·d exposure (10/2006-03/2007) [25, 26]
- EDELWEISS I, 3 Ge crystals (960g) phonon and ionization detector (SI and SD) (possible PSD to reject surface events), 62kg·d exposure (2000-2003) [27, 28]

- EDELWEISS II (successor experiment of EDELWEISS I), 7 Ge crystals and 1 Sapphire crystal (1.8kg Ge, 50 g Sapphire), phonon and ionization detector (SI and SD) / phonon and scintillation detector, since 01/2006 commissioning runs [27, 28]
- ROSEBUD, BGO and Sapphire crystals with Ge light detector (46g BGO and 92g Sapphire, 25g Ge and 50g Ge), double bolometers: phonon and scintillation detector (SI and SD), (1999-2006) [29, 30]
- CRESST I, 2 Sapphire crystals with Si light detector (514g), double bolometers: phonon and scintillation detector (SI and SD), 20.5kg·d exposure (2000-2002) [31]
- CRESST II, 3 CaWO₄ crystals with SOS light detectors (~1kg), double bolometers: phonon and scintillation detector (SI and SD), since 2004 commissioning runs and data taking, e.g. 3kg·d exposure (01/2007) [32, 33]
- XMASS, liquid Xe (3kg), scintillation detector with PSD (SI and SD), presently upgrading to a 100kg liquid Xe target [34]
- ZEPLIN I, two-phase (liquid/gas) Xe (31kg), scintillation and ionization detector, 225kg·d exposure (01/2007) [35]
- XENON 10, two-phase (liquid/gas) Xe (15kg), scintillation and ionization detector (time-projection chamber), 375kg·d exposure (2006-2007) [36, 37]
- WARP, two-phase (liquid/gas) Ar (2.3kg), scintillation and ionization detector (SI), 100kg·d exposure (2006) [38]

1.3 Aim of the Present Work

The main goal of the presented work is the investigation and development of the rf-sputtering technique for a reproducible production of large numbers of tungsten thin films that can be used as transition edge sensors (TES) for detectors employed in the direct Dark Matter search experiment CRESST. Hence, as described in chapter 2 the reproducible fabrication of α -W thin films with low transition temperatures (~ 10 mK) is aimed at. Additionally, the properties of so-called composite detectors (chapter 7 and 8) using sputtered α -W thin films are investigated concerning their applicability to direct Dark Matter search experiments, as e.g. the CRESST and the planned EURECA experiment.

Chapter 2

The CRESST Experiment

The CRESST (Cryogenic Rare Event Search with Superconducting Thermometers) experiment is located in hall A of the Gran Sasso Underground Laboratory (LNGS - Laboratori Nazionali del Gran Sasso) in Italy (3600m w.e.). It is aimed at the detection of WIMP-nucleus elastic scattering events with the help of cryogenic detectors. This chapter gives an introduction to the working principle of cryogenic detectors relying on the so-called phonon-light technique for background suppression, as well as to the CRESST experiment itself.

2.1 Working Principle of Cryogenic Detectors

The CRESST experiment uses cryogenic detectors equipped with superconducting transition edge sensors (TESs) operated at a few mK (~ 10 mK) to detect possible WIMP scattering events. The working principle is based on the detection of an energy deposition ΔE by an incident particle scattering in an absorber crystal (here: CaWO_4). The deposited energy generates phonons in the absorber crystal. The generated phonons cause a temperature rise ΔT in the TES attached to the absorber crystal. The temperature rise ΔT of the TES is related to the deposited energy ΔE in the TES by the relation:

$$\Delta T = \frac{\Delta E}{C} \quad (2.1)$$

where C is the heat capacity of the thermometer. Hence, a small C is necessary to obtain an as big as possible change in the temperature of the thermometer and therefore a high sensitivity of the detector. As the heat capacity contributions scale with T (electron system) and T^3 (phonon system) respectively, low working temperatures are desirable. The resulting dependency (in a rough approximation: indirect proportionality) of the signal amplitude on the heat capacity of the TES can also be seen in more detail from the basic thermal detector model described in [39, 40, 41].

In principle, the cryogenic calorimeters used in CRESST consist of three

parts (see figure 2.1): the absorber crystal, a thermometer that is thermally coupled to the absorber and a weak thermal link from the thermometer to the heat bath. Via the weak thermal link to the heat bath the energy is removed from the system and the equilibrium condition is restored.

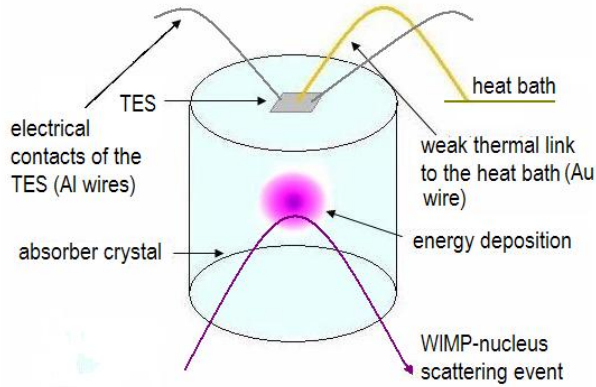


Figure 2.1: Sketch of the principle setup of a cryogenic calorimeter. The main parts are shown: the absorber crystal, the TES and the weak thermal link to the heat bath, as well as the thermal contacts of the TES. Additionally, the energy deposition of an incident particle in the absorber crystal is illustrated.

The TES is a thin metal film which becomes superconducting at low temperatures. To detect temperature changes one takes advantage of the fact that in the phase transition region from the superconducting to the normalconducting state the resistance R_T of the thin film is a function of the temperature T of its electron system, as shown in figure 2.2. Therefore, a temperature rise ΔT in the thermometer leads to a resistance change ΔR . Under ideal conditions this relation can be linearised in the phase transition region (figure 2.2) and results in:

$$\Delta R = \frac{\delta R}{\delta T} \cdot \Delta T = \frac{\delta R}{\delta T} \cdot \frac{\Delta E}{C} \quad (2.2)$$

Therefore, the TES is cooled to its transition temperature T_c (typically 10-100mK) and then the temperature of the TES is stabilised in the phase transition region by application of a current to the TES.

For the read out of the resistance change ΔR a dedicated circuit (figure 2.2) is used where a constant bias current I_0 is applied to the parallel branches of the circuit (see also [42]). Thus, a resistance change in the thermometer leads to a change in the branching of the current. The current I_I through the input coil L_I is therefore temperature dependent:

$$I_I(T) = I_0 \frac{R_T(T)}{R_T(T) + R_S} \quad (2.3)$$

- $I_I(T)$: current through the input coil
- I_0 : constant bias current
- $R_T(T)$: thermometer resistance
- R_S : constant shunt resistance

This current change induces a change in the magnetic flux of the SQUID (Superconducting Quantum Interference Device) input coil L_I in the right branch of the circuit, which is then measured with a DC SQUID [43].

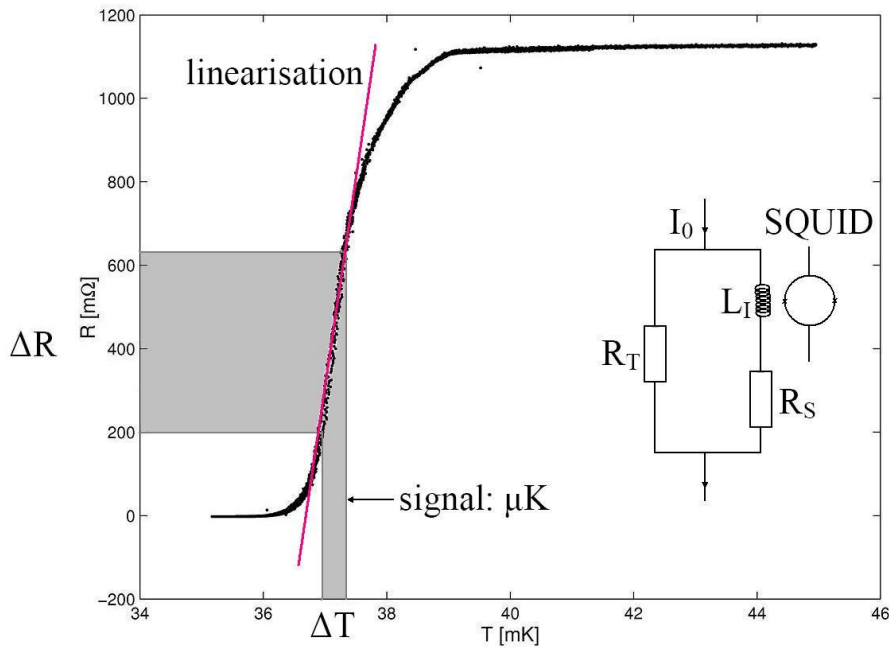


Figure 2.2: Resistance of a tungsten thin film in the transition region from the super- to normalconducting state. A small change in temperature ΔT leads to a measurable change in resistance ΔR . Under ideal conditions this relation can be linearised. Inset: Sketch of the read out circuit for the TES used in CRESST with R_T : thermometer/ TES resistance, R_S : constant shunt resistance, L_I : SQUID input coil, I_0 : constant bias current. A change in R_T changes the branching of I_0 and therefore the magnetic flux through L_I which is read out by a SQUID.

2.2 The CRESST Detectors

The interaction of WIMPs with baryonic matter is expected to appear as elastic scattering off nuclei. The CRESST detectors are sensitive to coher-

ent spin-independent (SI) WIMP-nucleus scattering events¹ on the whole nucleus.

2.2.1 The CRESST Detector Module

With CRESST-II it is attempted to detect these SI scattering events with modular detectors [18] based on scintillating CaWO_4 crystals (cylindrical shape, $\varnothing = 40\text{mm}$, $h = 40\text{mm}$) of $\sim 300\text{g}$ as target material. The phonon signal and the scintillation light originating from an event are measured simultaneously. The CaWO_4 crystal with a tungsten TES (W-TES) on top is operated as a cryogenic calorimeter to detect the energy, in form of phonons, that is deposited in the crystal by a scattering particle (see chapter 8) - the phonon channel. Another cryogenic detector is installed nearby and optimised for the efficient detection of the scintillation light of the CaWO_4 crystal - the light channel. The light detector consists either of a silicon wafer ($30 \times 30 \times 0.4\text{mm}^3$) or of an SOS (silicon on sapphire) substrate ($\varnothing = 40\text{mm}$, $h = 0.43\text{mm}$) [45] and is also equipped with a W-TES.

The detector module is positioned in a reflective housing (a copper holder with a reflective foil installed on the inside) to increase the efficiency of light collection (see figure 2.3). A polymeric multilayer foil (several layers of foil supported by a carrier foil) is used as reflective foil which has its maximum reflectivity at room temperature at a wavelength of the scintillation light of the CaWO_4 crystal ($\sim 420\text{nm}$).

2.2.2 The Phonon-Light Technique for Background Suppression

The CRESST detectors are designed for a simultaneous measurement of the phonon signal and the scintillation light produced by an event in the detector. The application of this so-called phonon-light technique is necessary to discriminate β and γ scattering events (electron recoils) from the expected nuclear recoils in the region of interest (recoil energies up to 40keV [18]). β and γ particles interact with the electron shell of the target atoms. Electron recoil events produce more light than nuclear recoil events. Hence, this technique is a powerful tool to efficiently suppress this background. This event-by-event discrimination can only be applied successfully down to energies where the two event bands, the electron and nuclear recoil band (figure 2.4) can be clearly distinguished. This energy range (typically $\sim 10\text{keV}$) is determined by the energy resolution and the threshold of the light detector (figure 2.4) as the amount of the detected light delivers the information for this distinction.

¹The cross section for coherent WIMP-nucleus interaction includes a factor of A^2 , where A is the relative atomic mass [44]. Therefore, materials containing heavy nuclei are favoured to detect WIMP-nucleus interactions, as e.g. CaWO_4 which contains W with $A=183.85$ (natural isotopic abundance).

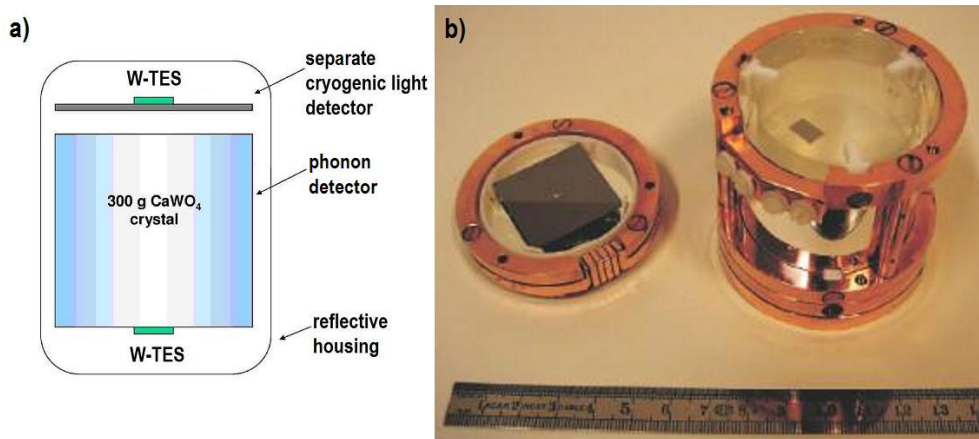


Figure 2.3: a) Schematic drawing of a CRESST-II detector module consisting of a CaWO_4 phonon detector and a separate light detector, both enclosed in a reflective housing. The tungsten TESs are read out via SQUIDs. b) Photo of a CRESST detector module, with (left) the light detector (silicon) and (right) the phonon detector (CaWO_4).

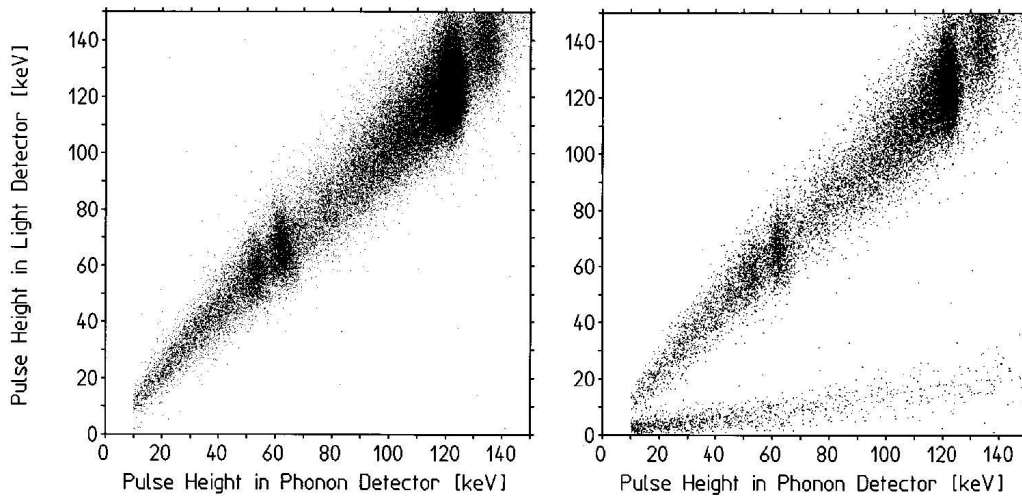


Figure 2.4: Pulse height in the light detector versus pulse height in the phonon detector (CaWO_4 crystal) [46]. The scatter plot on the left side was measured with an electron (^{90}Sr source) and a photon source (^{57}Co). Hence, the events in the resulting band are due to electron recoils. To measure the plot on the right a neutron source was added. Therefore, the events in the lower band are caused by nuclear recoil events in the detector leading to a reduced light generation compared to electron-like interactions.

The technique mentioned above is described with the help of the quenching factor [47] which is the reduction factor by which the light output for an

electron recoil event is divided to find the light output for a nuclear recoil event of the same energy, as shown by equation (2.4). Thus, at a fixed energy, the light output for a nuclear recoil event is proportional to the inverse of the quenching factor, which is hence normalised to the light output of an electron recoil event.

$$\text{light}_{\text{ion}} = \frac{1}{\text{quenching factor}} \text{light}_{\text{electron}} \quad (2.4)$$

This technique of identifying incident particles with the help of the scintillation light also allows to identify neutron-nucleus recoils which can easily mimic a WIMP. For kinetic reasons neutron events that can be observed in the detector are most likely to occur due to scattering off oxygen and calcium nuclei, whereas WIMP interactions in the detector are expected to result predominantly from scattering off tungsten nuclei. Up to now different experiments have been performed showing that recoils from different target nuclei produce different amounts of light [47]. Thus, it is possible to associate different quenching factors with calcium, oxygen and tungsten and to distinguish neutron scattering events from WIMP scattering events [48]. For this purpose accurate neutron calibration experiments have to be performed [49, 50].

Another class of events that could mimic WIMP interactions are surface events due to α -decays of elements (especially radon daughters) resulting from contaminations on the crystal or the reflector foil surface. A dangerous scenario would be that an atom situated on the surface of the crystal decays by α decay and the produced α particle goes away from the crystal while the slow nucleus enters the crystal. This nucleus could mimic a WIMP interaction. However, the carrier foil of the reflective foil scintillates at low temperatures when hit by an α particle [18]. Therefore, the escaping α -particle produces additional light by hitting the reflective foil [51]. Hence, these events are moved in the phonon-energy/light-energy plane (figure 2.4) from the nuclear recoil band upwards to the electron recoil band.

2.2.3 The Phonon Detector

The CaWO_4 crystal from which the phonon detector is built [18] is supported by silver coated copper beryllium springs to thermally decouple it from the copper holder. Phonons produced by a particle interaction in the crystal are scattered at the crystal surfaces until they are absorbed by the electron system of the TES where they thermalise and lead to a resistance change. The phonon detector TES is a $6 \times 8 \text{mm}^2$ superconducting tungsten film deposited on the crystal via e-gun evaporation with a thickness of 200nm [45]. After

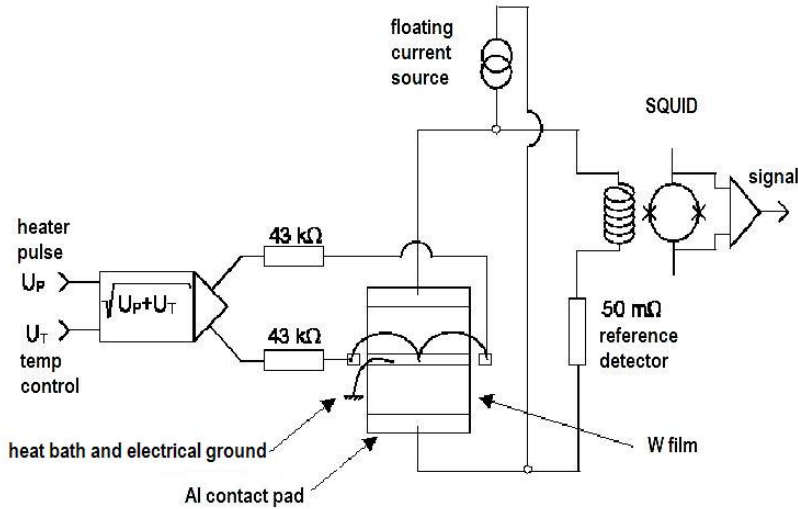


Figure 2.5: Detailed schematic drawing of a CRESST-II phonon detector TES with thermal and electrical contacts, as well as the SQUID read out circuit.

deposition the TES is structured by chemical etching (figure 2.5) [18]. Before deposition of the tungsten thin films on the CaWO_4 crystal a SiO_2 buffer layer is grown onto the crystal surface to prevent inter-diffusion between the tungsten thin film and the CaWO_4 crystal.

The thermal connection to the heat sink and electrical grounding of the detector is realised by two $25\mu\text{m}$ thick gold wires. The gold wires connect a gold bond pad which is deposited onto the middle of the tungsten thin film with the copper holder. The copper holder serves as the thermal heat sink as it is coupled to the mixing chamber which is in turn stabilised at a temperature of $\sim 6\text{mK}$. The thermal link to the heat bath defines the decay time of the detector pulses. Electrical contacts for the bias current and the SQUID read out circuit are realised by superconducting aluminum bond wires ($25\mu\text{m}$) which connect aluminum bond pads, deposited onto each end of the tungsten thin film, with isolated contact pads on the copper holder. These are then connected to the SQUID read out circuit. A heater circuit is connected to the gold bond pad in the middle of the thermometer. With this heater the tungsten thin film is heated up until its resistance is in the super-to normalconducting transition region (working point) and then stabilised there (see section 2.2.5).

2.2.4 The Light Detector

The light detector consists of a silicon wafer or a silicon on sapphire (SOS) substrate with a W-TES of 1200\AA thickness (figure 2.6). This light detector

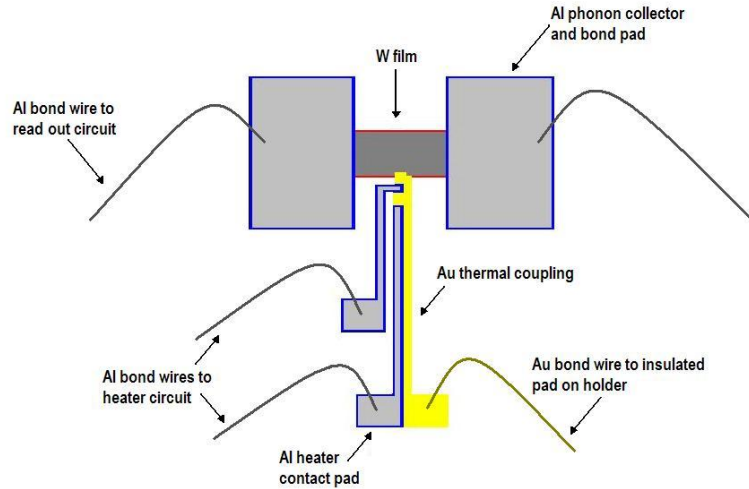


Figure 2.6: Schematic drawing of a CRESST-II light detector TES and its thermal and electrical contacts.

needs to be very efficient regarding light detection since only $\sim 1\%$ of the energy deposited in the crystal leads to scintillation light emission that is then recorded by the light detector. The working principle of the W- TES is the same as of the one deposited on the CaWO_4 crystal. However, there are two differences that should be mentioned. First, the thermal link to the heat bath is again delivered by a gold bond wire which, however, in this case is not directly bonded onto the copper holder but onto a contact pad on the copper holder, which is electrically isolated from the copper holder to reduce electronic interference. Second, the aluminum bond pads on the thermometer are replaced by much larger (0.5mm^2 each, $1\mu\text{m}$ thick) aluminum phonon collection pads. These pads cover almost the whole tungsten thermometer, leaving only a small area uncoated which then acts as the effective thermometer. The aluminum-covered area of the tungsten thin film is superconducting with a transition temperature close to the transition temperature, T_c , of aluminum (1.2K). This is required because inside the silicon phonons are known to decay due to scattering off the surface and therefore are "lost" for the signal generation. Due to the large surface to volume ratio of the silicon wafer this is a critical issue. The phonons are absorbed in the aluminum tungsten bilayer where they are transported to the effective tungsten TES almost without dissipation. Another strategy to improve the phonon transport to the TES is the use of an SOS substrate [45]. In the silicon-coating layer the scintillation light is absorbed while the phonon transport properties are improved due to the use of the Al_2O_3 substrate.

2.2.5 Stabilisation of the Detectors

Temperature stabilisation of both detectors is achieved by taking the baseline of the SQUID output voltage between pulses as a reference for the TES temperature (sampling rate: 10Hz). With this information the current through the heater on the TES is then adjusted. With this method a stabilisation of the temperature within a few μK can be obtained. Energy calibration and response stability of the detectors are monitored in terms of detector response to heater test pulses (electronically produced current pulses through the heater circuit) that have a number of discrete energies spread over the range of interest [18].

2.3 The CRESST Low-Background Setup

Due to the very low expected event rate in the order of less than $10^{-2}\text{cts keV}^{-1}\text{kg}^{-1}\text{day}^{-1}$ of the rare event search it is very important for the CRESST experiment to be shielded efficiently against all kinds of background. Possible sources of background are all sorts of particles that can interact in the detector and mimic a WIMP scattering event. In order to realise a low-background setup different strategies are applied.

The CRESST experiment is setup in a three-level building (figure 2.7) in hall A of the LNGS which provides a $\sim 3500\text{m w.e.}$ shielding. Therefore, the surface muon flux is reduced by a factor of 10^6 to $\sim 1\text{m}^{-2}\text{h}^{-1}$.

The top level of the building houses the control room and is additionally equipped with a small laboratory and a laminar flow area where detectors are prepared before being mounted in the cryostat. The ground floor and the first floor house the experiment itself. The experimental setup with all shieldings and also the primary electronics are surrounded by a Faraday cage which is divided into two parts. The lower part houses the clean room, containing all shieldings and the detectors, while the upper part includes the electronics and the service area with the top plate of the cryostat. The data acquisition system as well as the gas handling and the pumping system of the cryostat are positioned outside of Faraday cage.

The detectors themselves are shielded against ambient radioactivity by 14cm of ultra pure copper and 20cm of low-radioactivity lead (figure 2.8). Inside the shielding only radiopure materials are used. This shielding with the experiment inside is surrounded by an air-tight aluminum box (the radon box) that is constantly flushed with nitrogen and kept at a slight overpressure to prevent radon from penetrating into the shielding. For CRESST-II also a muon veto consisting of plastic scintillator panels and a 50cm thick polyethylene (PE) neutron moderation shield were installed outside the radon box. From simulations one would expect a count rate of approximately $47\text{-}69\text{cts kg}^{-1}\text{y}^{-1}$ due to neutrons in the energy range of 15-25keV without the polyethy-

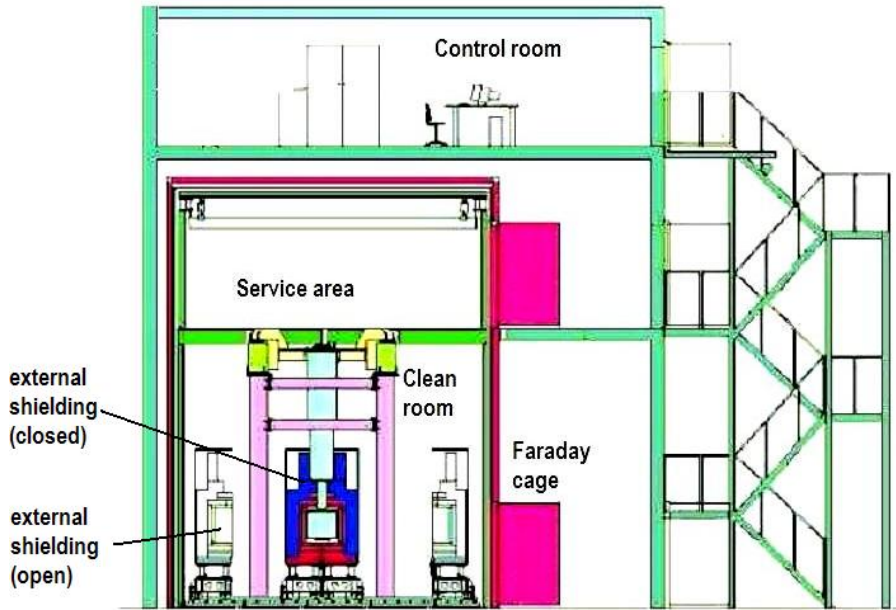


Figure 2.7: Cross section of the CRESST building in Hall A (3600m.w.e.) at the LNGS (Laboratori Nazionali del Gran Sasso). The external shielding is shown in both its open (green-white) and closed (blue-red) positions.

lene shield while with the 50cm thick shield a rate of only $6\text{-}36\cdot 10^{-3}\text{cts kg}^{-1}\text{y}^{-1}$ in this energy range is estimated [52]. Thus, a good background suppression of low energy neutrons² can be achieved. The neutron induced background is then dominated by high energy neutrons that are produced by muon interactions in the rock³ and the experimental shielding. These contributions can be partly suppressed with the help of the muon veto which is installed inside the neutron moderator and by exclusion of multiple scattering events.

2.4 The CRESST Cryostat

The CRESST detectors are stabilised at $\sim 10\text{-}15\text{mK}$ to assure high sensitivity of the experiment. A commercial $^3\text{He}\text{-}^4\text{He}$ dilution refrigerator unit⁴ has been chosen in combination with a 1.5m long cold finger consisting of low-background copper that transfers the cold temperature to the experimental setup [44] (figure 2.8).

The refrigerator and the pumping lines are designed such that a base-temperature of 6mK and a cooling power of 1mW at 100mK are reached. The dilution refrigerator consists of a liquid nitrogen cooling stage, a liquid he-

²Low energy neutrons are caused by fission and (α,n) reactions due to uranium and thorium activities in the surrounding rock and concrete and by fission in the shielding

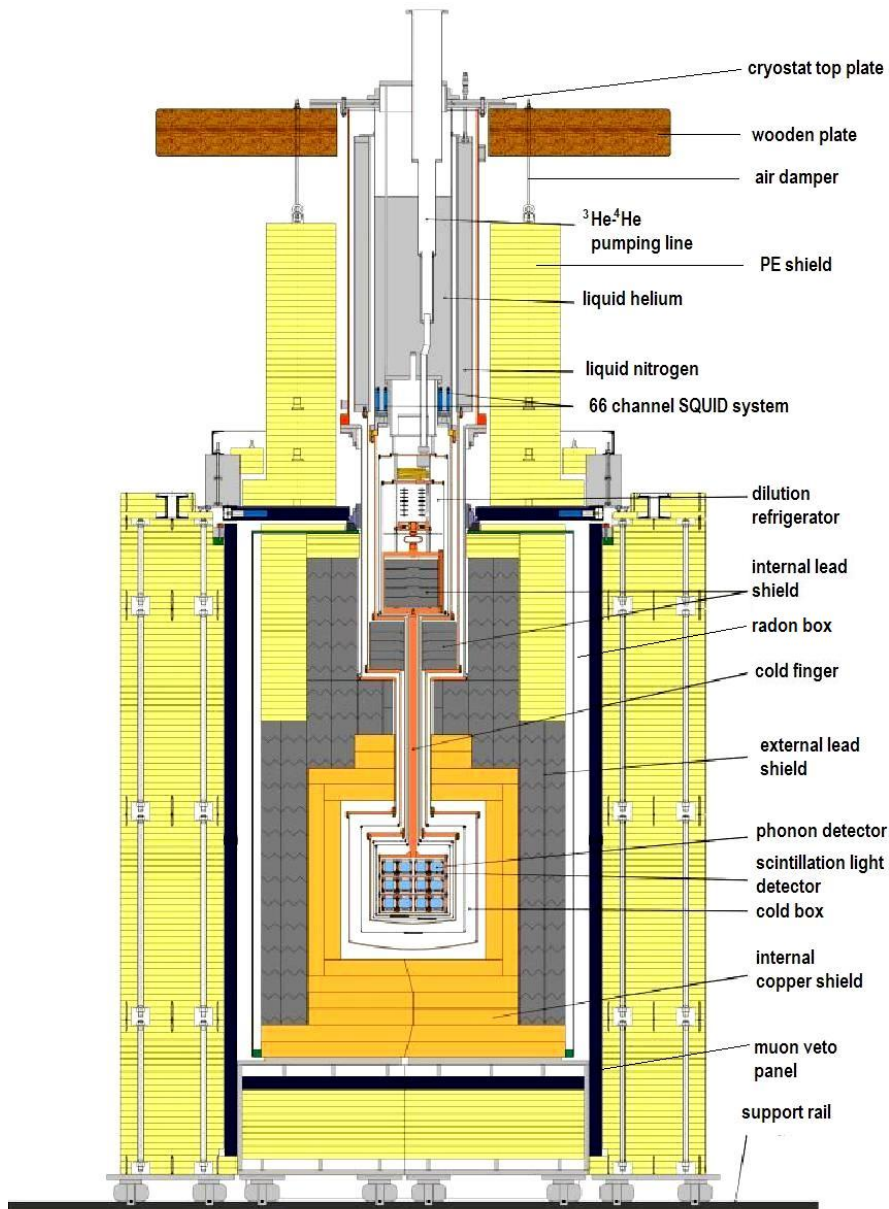


Figure 2.8: Sketch of the CRESST-II Cryostat [54].

lium cooling stage, a 1-K pot stage, where the temperature of liquid helium is lowered to about 1.2K by pumping on the gaseous phase above the liquid helium, and a mixture circuit where the ^3He - ^4He mixture is circulated to reach base temperature.

Between the dilution unit and the cold finger a 20cm thick lead shield (lead surrounding the experiment.

³These neutrons can produce additional neutrons by spallation in the shielding materials.

⁴An overview of the working principle of a ^3He - ^4He dilution refrigerator is given in [53].

with a ^{210}Pb activity of less than 3.6Bq/kg) inside a copper can is installed to avoid any line of sight between the detectors and components made of other materials, as e.g of the dilution unit.

This shield is continued with a lead shield around the cold finger containing the detectors. This external lead shield out of 20cm of "Bolidean" lead, with a ^{210}Pb activity of 35Bq/kg, contains an additional copper shield of 14cm of radiopure copper, which directly houses the experimental volume. By adopting this approach it is expected to achieve an efficient shielding of the detectors from radiation due to the material of the dilution unit. The detectors themselves are thermally shielded by a cold box that consists of five concentric radiation shields. The cold box shields are also made from low-background copper with high-purity lead used for the vacuum seals. To avoid activation of the low-background copper by muons the time the copper spent above ground was minimised⁵. However, it is not sufficient to use high-purity materials but it is also necessary to keep the surfaces clean. Therefore all surfaces are electropolished and then kept clean. All work on the low-background parts can be performed in a class 100 clean room that surrounds the whole experimental setup, the cold box, the inner and outer shieldings, the PE neutron moderation shield, the muon veto and the dilution refrigerator up to the top plate.

The dilution unit, with the cold box housing the experimental setup, is hung from a wooden plate which is placed on air dampers to reduce the influence of microphonics. To additionally decouple the dilution unit which could cause vibrations due to the boiling of cryogenic liquids from the experimental setup itself, the detector carousel is mounted on the cold finger via a spring. With this construction up to 100 kg of detector and shielding material can be supported.

For CRESST-II the electronics and the detector support construction were upgraded to 66 channels so that currently 33 detector modules, i.e., 10kg of target material, can be accommodated.

2.5 Results of the CRESST Experiment

In early 2004 several short runs with detector modules similar to the ones described above (with a silicon light detector) were performed [18]. In figure 2.9 data taken with two detector modules (Julia/BE14 and Daisy/BE13) are presented. The exposure time for Daisy/BE13 used for this plot was 39.043 days. After cuts this yields an exposure of 10.724 kg days. The exposure time for Julia/BE14 used for this plot was 37.572 days. After cuts this yields an exposure of 9.809 kg days. With this data, assuming a quenching factor of 7.4 for nuclear recoils [48, 18] (see 2.2) and a standard halo model

⁵The copper was stored in Munich in a cellar that provides a 10m water equivalent shielding. Therefore, the hadronic component is reduced by a factor of ~ 500 .

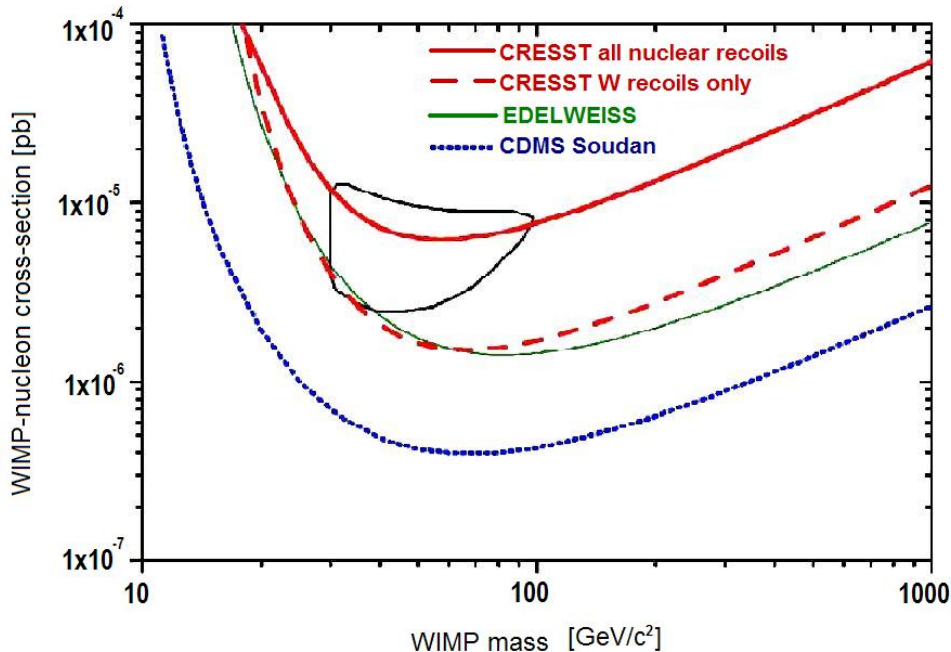


Figure 2.9: Exclusion limits in terms of coherent (spin-independent) scattering from first data taking with detector modules developed for CRESST-II [18]. Assuming a quenching factor of 7.4 to identify nuclear recoils the solid red curve is obtained. Applying a quenching factor of 40 to identify tungsten recoils to the data of the module Daisy/BE13 the dashed red line is obtained [18]. Regions above the curves are excluded at 90% CL. The closed region represents the claim of a positive WIMP modulation signal by the DAMA collaboration [55]. The green line represents the exclusion limit set by the EDELWEISS experiment [56], while the blue line gives the exclusion limit of the CDMS experiment [57].

(isothermal halo, WIMP characteristic velocity: 220 km/s, mean Earth velocity: 232 km/s, local WIMP density: $0.3 \text{ GeV}/c^2/\text{cm}^3$), it was possible to set a competitive limit on the WIMP interaction cross section. In figure 2.9 this exclusion plot, see solid red curve, is shown together with the DAMA 3σ signal region [55] and exclusion limits from EDELWEISS [56] and CDMS [57]. The dashed red curve is calculated from the same data but applying a quenching factor of 40 for tungsten recoils [48, 18]. This corresponds to zero events in the acceptance region (10keV to 40keV). This result remains the same even when reducing the quenching factor down to 35.8, where the first event enters the region of interest.

Another run with CRESST-II detector modules (these modules are equipped

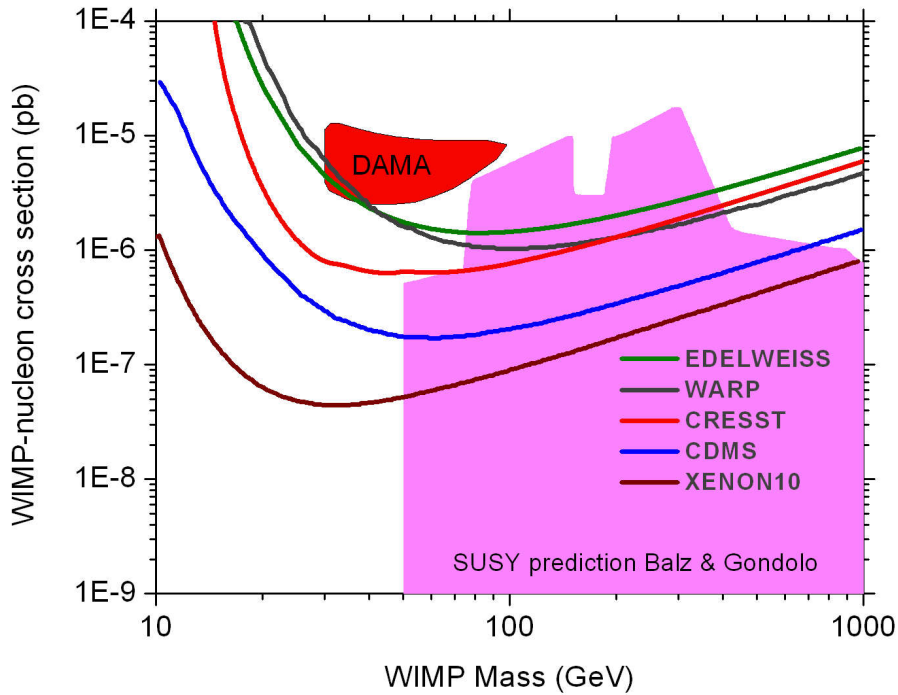


Figure 2.10: Current exclusion limits from the direct search Dark Matter experiments, the EDELWEISS experiment (green line) [56], the CRESST-II experiment [58] (red curve), the current WARP limit [38] (dark grey line), an improved CDMS limit [26] (blue line) and the current limit set by the XENON10 experiment, a noble gas experiment, (brown line) [59] are shown together with the DAMA 3σ signal region (red area) and the parameter space favoured by the SUSY theory (pink area) [60].

with SOS light detectors) was performed from october 2006 to the middle of 2007 resulting in an improved limit. In figure 2.10 the new limit obtained with the CRESST-II experiment from tungsten recoils only, as described above, can be seen [58] (red line). Additionally, the current limit set by the EDELWEISS experiment (green line) [56], the current WARP limit [38] (dark grey line), an improved CDMS limit [26] (blue line) and the current limit set by the XENON10 experiment, a liquid noble gas experiment, (brown line) [59] are shown together with the parameter space favoured by the SUSY theory [60] (pink area) and the DAMA 3σ signal region [55] (red area).

2.6 EURECA

For the future a further scaling up of the absorber mass of direct Dark Matter experiments (as e.g. EDELWEISS, CRESST and ROSEBUD) is aimed at to fully exploit the parameter space favoured by the SUSY theory for the WIMP mass and WIMP interaction. Apart from experiments using cryogenic detectors, experiments using liquid noble gases (as e.g. the XENON10 experiment) recently proved to offer a promising potential for the detection of Dark Matter.

EURECA (European Underground Rare Event Calorimeter Array) [61] is a project using cryogenic detectors to search for Dark Matter and is mainly a collaboration of the present groups of EDELWEISS, CRESST and ROSEBUD. EURECA is planned as a multi-target experiment of ~ 1 tonne for WIMP identification. Hence, the investigations and the development done in the course of the collaborating experiments can already be seen as research and development (R&D) for EURECA.

Chapter 3

Properties of Tungsten

In the CRESST experiment tungsten (W) thin films are used as TESs. Due to their low transition temperature (T_c) of $\sim 15\text{mK}$ they allow to reach an extraordinarily high sensitivity, which is essential for Dark Matter detection. However, the T_c of tungsten thin films can vary over a large range of temperatures (from $\sim 5\text{mK}$ to $\sim 6\text{K}$). It is therefore very important to investigate and understand the properties of tungsten in general and of tungsten thin films in particular in order to reproducibly fabricate W-TESs with the required T_c of $\sim 10\text{-}15\text{mK}$.

3.1 General Properties of Tungsten

Tungsten is a 5d transition element. Its atomic number is 74 and its average relative atomic mass is 183.85 ± 0.03 [62]. The tungsten isotopes with the largest natural abundances (^{182}W , ^{183}W , ^{184}W , ^{186}W) are stable [62]. Other tungsten isotopes exhibit β decay (^{185}W , ^{187}W) with half-lives of $T_{1/2}=75.1\text{d}$, $T_{1/2}=23.9\text{h}$ [62], respectively α decay (^{180}W) with a half-life of $T_{1/2}=(1.8 \pm 0.2) \cdot 10^{18}\text{y}$ as determined by CRESST [63].

With its specific heat capacity of $0.116\text{J}/(\text{gK})$ (at 298K) [62] tungsten ranges among the materials with the lowest heat capacities. The heat capacity at low temperatures is dominated by the electronic specific heat coefficient while the phononic contribution can be neglected at very low temperatures. As reported by T. R. Waite et al. [64] the specific heat of tungsten at very low temperatures (up to 40K) can be described by:

$$c [J/(gK)] = \gamma \cdot T + 10.57 \cdot \left(\frac{T}{\Theta}\right)^3 \quad (3.1)$$

where γ is the specific electronic heat capacity and Θ is the Debye temperature. In the range from 4 to 15K values of $\gamma=6.04 \cdot 10^{-6}\text{J}/(\text{gK}^2)$ and $\Theta=378\text{K}$ are found. A value of γ for lower temperatures ($\leq 1\text{K}$) is given by J. Rayne [64]: $\gamma=7.94 \cdot 10^{-6}\text{J}/(\text{gK}^2)$. This yields a low-temperature heat capacity for

tungsten of:

$$c [J/(gK)] \approx 7.94 \cdot 10^{-6} \cdot T \quad (3.2)$$

where the phononic contribution is neglected. This small heat capacity at low temperatures (for comparison, aluminum has a low-temperature value of $1.350 \cdot 10^{-3} J/(gK^2)$ [65]) is important for the application of tungsten as a TES, as already described by equation 2.1.

3.2 Crystal Structure and Electronic Properties of Bulk Tungsten

For bulk tungsten, an amorphous phase and two crystal structures are known to occur - the so-called α -W and the β -W structures, described in the following sections.

3.2.1 Bulk α -Tungsten

The only stable crystal structure is reported to be the α -W structure, the bcc-lattice structure (body centered cubic) [62]. The lattice constant is $a=3.165\text{\AA}$. In figure 3.1 a crystal unit cell and an X-ray diffraction diagram of α -W is shown (2ϑ -values obtained with the Cu- K_{α_1} line, $\lambda_{\text{Cu},\alpha_1}=1.541\text{\AA}$). The α -W structure has the largest cohesive energy of all elements [62] (including diamond). The cohesive energy can be interpreted as the bonding energy of tungsten in the bcc-lattice structure at 0K. This is the difference of the crystalline bulk energy and the total energy of the free atom. The experimental value, derived from extrapolations amounts to 8.9eV/atom.

The electrical resistivity ρ can be described with Mattheissens's law as the sum of two terms:

$$\rho(T) = \rho_0 + \rho(T) \quad (3.3)$$

where the first term ρ_0 represents resistivity due to electron scattering at defects of the crystalline lattice as e.g. impurities or inner and outer surfaces. The second term $\rho(T)$ is due to the temperature dependent collision of electrons with quasiparticles such as phonons or other electrons. The lower the electron scattering rate at crystal defects, the smaller the first term in equation 3.3.

The resistivity at room temperature for bulk tungsten is $\rho_\alpha \approx 5.3\mu\Omega\text{cm}$, the electron mean free path for bulk tungsten at room temperature is around $l \approx 41\text{nm}$ [66].

3.2.2 Bulk β -Tungsten

A metastable configuration that is also found to occur for bulk tungsten is the β -W modification which corresponds to the cubic A15 lattice structure

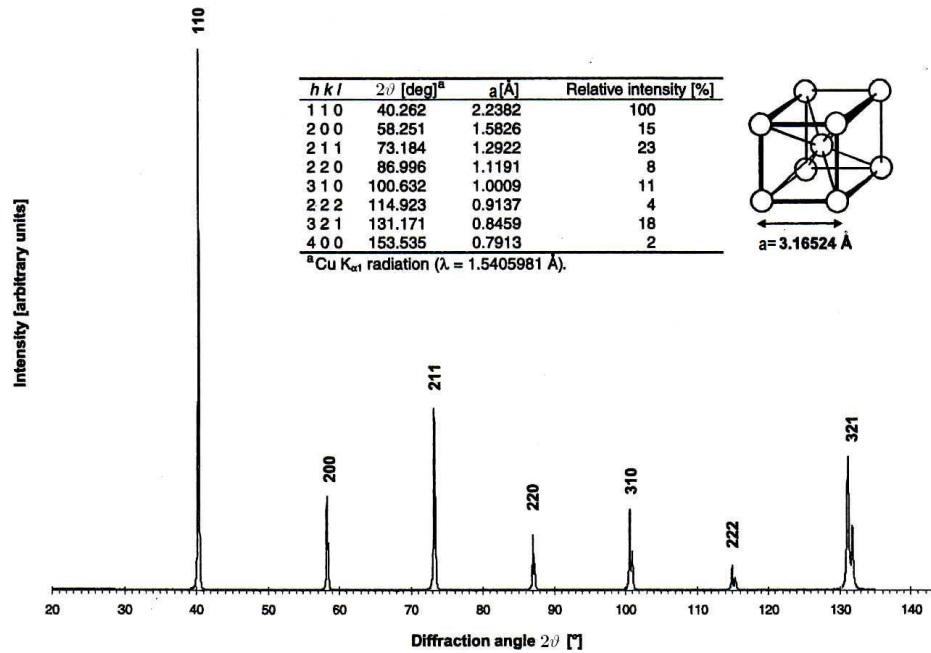


Figure 3.1: X-ray diffraction pattern and crystal unit cell (bcc structure) of α -W. ϑ - 2ϑ measurements were performed with the Cu- $K_{\alpha 1}$ line [62].

[62]. This crystal structure is of the Cr_3Si type and can be described as a bcc structure where to each cube edge of the unit cell an additional atom is assigned. The lattice constant amounts to $a=5.051\text{Å}$ [62]. In figure 3.2 a crystal unit cell and an X-ray diffraction diagram of β -W is shown (2ϑ values obtained with the Cu- $K_{\alpha 1}$ line, $\lambda_{Cu, \alpha 1}=1.541\text{Å}$).

β -W is known to transform to α -W when heated above $600\text{ }^\circ\text{C}$ [62]. Several other elements, such as P, As, Al, K [62] and O [67] are known to promote the formation of β -W and also have a stabilising effect at higher temperatures when included as impurities in the bulk material.

For β -W a much higher electronic resistivity is reported [62] than for α -W: $\rho_\beta \geq 10 \cdot \rho_\alpha$.

3.3 Crystal Structure and Electronic Properties of Tungsten Thin Films

Crystallographic structures that differ from the ones of bulk materials are known to exist in thin films ($\sim \mu\text{m}$ to nm range) for a number of metals. For tungsten thin films 3 different crystal structures or mixtures of these are reported to occur: the α -W structure [62, 68], the β -W structure [62, 68, 67, 69] and the so-called γ -W structure, the latter exhibiting an fcc-lattice structure [62, 68, 70].

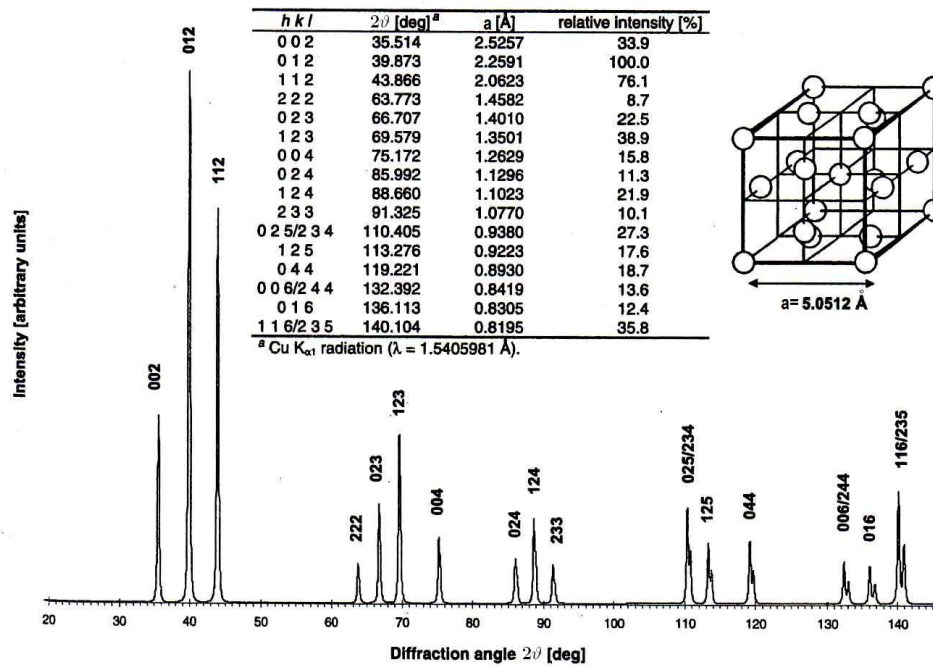


Figure 3.2: X-ray diffraction pattern and crystal unit cell (Cr_3Si structure) of β -W. ϑ - 2ϑ measurements were performed with the $\text{Cu-K}_{\alpha 1}$ line [62].

For tungsten thin films the electrical resistivity is dependent on different film properties. The film's crystal structure as well as the grain size and the film thickness can affect the electron mean free path and therefore the resistivity.

3.3.1 Crystal Structure of Tungsten Thin Films

The content of each crystal phase in a tungsten thin film is reported to be very sensitive to the deposition conditions, the film thickness as well as the substrate material and its crystal structure and orientation used for the deposition [67, 71, 70, 69]. These dependencies are very complex and cannot be easily generalised to the use of different deposition techniques (e-gun evaporation, dc- or rf-sputtering, laser ablation etc.). Also the deposition parameters (deposition rate, substrate temperature, pressure during deposition, residual pressures of e.g. oxygen etc.) need to be modified to obtain similar results. As a general tendency it could be extracted that for substrate temperatures during the deposition process of ≥ 400 °C an increased appearance of the pure

α -W phase (with low defect densities) in the thin films can be observed [72]¹. For lower deposition temperatures an enhanced occurrence of the β -W or γ -W phases is reported and non-epitaxial growth is observed [69, 66, 70]. Another general rule that seems to hold true is that if the background pressure during deposition, especially the oxygen residual pressure, increases the β -W content in the thin film also increases [67, 71].

3.3.2 Thin Film α -Tungsten

For thin films exhibiting the α -W structure a lattice constant of $a \approx 3.17 \text{ \AA}$ ranging among the bulk value is reported [67]. The α -W thin films show room-temperature resistivities ranging from $5.3 \mu\Omega\text{cm}$ (bulk value) for films deposited at substrate temperatures $\geq 400\text{-}500 \text{ }^\circ\text{C}$ [72] and containing a pure α -W phase up to values of $\sim 40 \mu\Omega\text{cm}$ [68] for α -W films that form after transformation from the β -W structure. These relatively high resistivity values are attributed to scattering from impurities and grain boundaries. For thin films with a thickness $\leq 10\text{nm}$ even higher resistivity values are reported, which can be assigned to a so-called size effect [66]. The size effect includes the scattering of conduction electrons on the film's surface. In [66] a relation, describing the size effect, for the resistivity ρ and the film thickness t is given:

$$\rho = \rho_\alpha \cdot \left[1 + 0.375 \cdot l \cdot (1 - p) \frac{1}{t} \right] \quad (3.4)$$

where ρ_α is the bulk resistivity value, l the bulk value of the electron mean free path and p the scattering coefficient at the surface². However, it has to be pointed out that this equation does not include effects on the resistivity due to "internal" processes in the thin film, as e.g. scattering on grain boundaries or due to surface roughness. Hence, this equation only contains surface scattering as an additional effect on the bulk resistivity value. Therefore, it gives a resistivity value for "ideal" epitaxially grown α -W thin films, where the resistivity is only influenced by the film thickness through scattering on the surfaces. Typical values for the resistivity (300K) obtained for α -W thin films range among $\sim 20 \mu\Omega\text{cm}$ or more [71]. At helium temperature (4.2K) resistivity values of down to $0.2 \mu\Omega\text{cm}$ have been measured [72].

The typical grain size for α -W films³ is reported to be $\sim 100\text{-}150\text{nm}$. An indicator for the crystalline quality of the film is the so-called RRR-value, the residual resistance ratio. It relates the resistivity at room temperature

¹In [72] the used deposition technique, laser ablation, is presumed to lead to an even higher effective growth temperature.

² p ranges from 0 to 1 corresponding to diffusive and purely elastic scattering. For thin films mostly complete diffusive scattering appears [66].

³These films were directly grown as α -W films and did not undergo a β - to α -W transformation.

to the resistivity at liquid helium temperature.

$$\text{RRR} = \frac{R(300K)}{R(4.2K)} = \frac{\rho(300K)}{\rho(4.2K)} \quad (3.5)$$

As can be seen from equation 3.3 at lower temperatures the resistivity mainly originates from scattering at crystal defects or grain boundaries. Hence, this ratio offers a measure of crystallinity and impurity traps in the film. In literature values for epitaxially grown α -W thin films in the range from ~ 7 up to 20 are found [72].

3.3.3 Thin Film β -Tungsten

Thin films containing the pure β -W phase are reported to exhibit a lattice constant $a \approx 5.05 \text{ \AA}$ in the range of the bulk value for β -W [67]. The pure β -W thin films exhibit a much higher room-temperature resistivity in the range of $\sim 100\text{-}300 \mu\Omega\text{cm}$ [68, 71] than thin films of α -W. This is usually attributed to the β -W grain size which is reported to take values in the range of 5-10nm [68]. Hence, the electron scattering on grain boundaries causes additional resistivity in contrary to α -W films [68].

The β -W to α -W transformation is again reported to occur at elevated temperatures of $\geq 150 \text{ }^\circ\text{C}$ [68] in most cases. In some cases this transformation was observed to occur also at room temperature [66].

3.3.4 Thin Film γ -Tungsten

The γ -W structure corresponds to the fcc-lattice structure (face centered cubic) with a lattice constant of $a = 4.13 \text{ \AA}$ [62]. This crystal structure is metastable and transforms to the α -W structure when heated above $700 \text{ }^\circ\text{C}$ [62]. The transformation can also occur at lower temperatures of $\sim 200 \text{ }^\circ\text{C}$ depending on the production process of the tungsten thin films and thus, depending on the crystallinity of the film [70].

A crystalline γ -W phase is only reported to be observed in films sputtered onto rock salt maintained at a temperature of $\sim 250\text{-}400 \text{ }^\circ\text{C}$ during deposition [70]. Specific resistivities for γ -W thin films range from $\sim 100\text{-}1000 \mu\Omega\text{cm}$ [73]. A grain size down to $\sim 1\text{-}2 \text{ nm}$ is reported for non-epitaxial γ -W films deposited at room temperature [70].

3.4 Superconductivity of Tungsten

Bulk tungsten exhibiting the α -W phase is a type I superconductor [74] with a transition temperature of $T_c = 15.4 \pm 0.5 \text{ mK}$ [62].

The transition temperature T_c of tungsten thin films depends on different thin film properties as e.g. the crystal structure [67, 70, 71], strain or stress

in the thin film [75], magnetic or other impurities [76, 77].

For pure crystalline α -W films the transition temperature corresponds to the bulk value of $\sim 15\text{mK}$ [71]. For tungsten thin films mainly exhibiting the β -W phase T_c values in the range from 1 to 4K are reported [71]. γ -W films are measured to exhibit a T_c up to 6K [70, 62]. For tungsten thin films containing a mixture of the α -W and the β -W phase the transition temperature is dependent on the abundance ratio of the two crystal structures in the thin film [71]. As already depicted in section 3.2.2 the formation of β -W is promoted by the abundance of some elements, especially oxygen (this also holds true for β -W thin films). Hence the concentration of special impurities in the thin film can be in the end connected to the transition temperature. It is indicated in [71] that for $T_c \leq 66\text{mK}$ only the α -W phase is found in the thin film. The nonetheless increased transition temperature of an α -W film could under certain conditions be attributed to stress in the thin film⁴ [71].

The effect of stress in tungsten thin films, induced by lattice mismatch with the substrate surface, or by differential thermal contraction of the substrate and the thin film, on the transition temperature can be due to two different mechanisms. First the crystal phase composition of the tungsten thin films can be affected by a stressed crystal lattice. In films with tensile stress, the amount of the β -W phase increases at the cost of the α -W phase, while in compressively stressed films only a very small amount of β -W is found to occur [78]. This difference in the lattice phase composition can then be linked to different transition temperatures. The other possibility of a stress induced variation of T_c can be associated to a deformation of the lattice structure and, hence, to a resulting change of the phonon frequencies and the electron density of states $N(E)$. According to the weak-coupling BCS theory [75] T_c is expressed by

$$k_B T_c = 1.13 \hbar \omega_D e^{-\frac{1}{\lambda}} \quad (3.6)$$

where k_B is the Boltzmann constant, \hbar is the Planck constant, ω_D is the Debye frequency and $\lambda = N(E) V_{\text{eff}}$, where V_{eff} is the effective coupling between the electrons mediated by the electron-phonon coupling. As described in [75] ω_D commonly increases the more the lattice is compressively stressed (phonon hardening) while the average value of the electron density of states $N(E)$ is expected to decrease in a compressively stressed lattice due to a band-broadening effect of the pressure on the lattice. The pressure dependency of V_{eff} is even more complicated and, in addition, this simple model for the T_c dependency should be extended as tungsten is not very well described by the weak-coupling BCS theory. However, the principle mechanism is given by equation 3.6. For a more detailed description see [75].

⁴This stress may also be induced by differential thermal contraction of the substrate and/or changes in the phase composition at cryogenic temperatures compared to room temperature [71].

For pressure acting on the crystal structure - a reduction of the volume or lattice constant - a decrease of T_c is expected while for tensile stress acting on the crystal structure - an enlargement of the volume or lattice constant - an increase of T_c is expected.

Additionally, the crystallinity of the thin film can also have an impact on its superconducting properties. If the thin films contain small grains in comparison to the usual electron mean free path, its resistivity increases. In terms of superconductivity small grains can eventually also decrease the mean free path length of Cooper-pairs and therefore the coherence length ξ [79]. As described in the standard Ginzburg Landau superconductivity theory this coherence length is connected to the transition temperature [79] by:

$$\xi_0 = \frac{\hbar^2}{4m^*\alpha_0 T_{c0}} \quad (3.7)$$

where ξ_0 is the zero-temperature coherence length with $\xi(T) = \xi_0 \left| \frac{T}{T_c} \right|^{-\frac{1}{2}}$, \hbar is the Planck constant, m^* is the effective mass of the Cooper-pair, $\alpha_0 = \frac{a}{T - T_c}$ with a being the first Landau parameter and $T_{c0} = T_c(H=0)$ is the transition temperature at zero external magnetic field. For this reason, a decrease of ξ could be connected to an increase of T_c . As already depicted in section 3.3.2 the RRR value acts as an indicator for the crystal structure (epitaxial growth versus grain size) and hence for the grain size present in the thin film and can therefore - in some cases - be associated to T_c .

As mentioned above magnetic impurities included in the thin film also effect the transition temperature. This effect was indeed used in [76, 77] for tuning the transition temperature by controlling the implanted dose of different magnetic impurities such as Co, Fe or Ni. It is reported that an increase in the implant dose results in a decrease (the slope depends on the used element) of T_c [76, 77]. In the small concentration limit (of the magnetic atoms in the thin film) a linear dependency is found [76]. However, no effect on the width of the transition region ΔT_c is reported [76].

3.5 Summary of Tungsten Properties

In the following a table is given containing the most important properties of tungsten investigated in this work:

	crystal structure	a [Å]	ρ_{300K} [$\mu\Omega\text{cm}$]	T_c [K]
bulk α -W	bcc	3.165	5.3	0.0154
bulk β -W	A15	5.051	$\sim 10 \times 5.3$	n.s.
thin film α -W	bcc	~ 3.17	$\sim 5.3-40$	$\sim 0.015-0.066$
thin film β -W	A15	~ 5.05	$\sim 100-300$	$\sim 1-4$
thin film γ -W	fcc	4.13	$\sim 100-1000$	≤ 6

Table 3.1: Properties of the different tungsten crystal structures.

where a is the lattice constant, ρ_{300K} is the specific resistivity at room temperature and T_c is the transition temperature. For thin films the lattice constant values given are valid for epitaxially grown non-stressed films. The specific resistivity values and transition temperatures stated for thin films are dependent on the crystallinity (grain size/epitaxial growth) of the thin film and on the stress (tensile/compressive) present in the thin film.

Chapter 4

Experimental Setup of the RF-Sputtering Magnetron Facility

The deposition technique used for the production of tungsten thin films in the course of this work is the rf-sputtering technique. For this purpose a vacuum facility equipped with three magnetron sputtering cathodes is used. This facility is situated in the evaporation lab of the institute E15, TUM in Garching. Only a brief description of the system is given in section 4.2, for a more detailed description see [39]¹ and [45]. Special attention is given to newly added components (section 4.3 and 4.4) and their operation.

4.1 Working Principle

Sputter deposition is one of the physical vapour deposition (PVD) techniques. The basic components of a sputtering setup include the source material which is called the target, a glow discharge plasma of positive ions (an inert gas such as argon) that forms above the target, a device for the ignition of the plasma (e.g. an ion gauge) and a substrate that is positioned opposite to the target. The whole construction is set up in a vacuum recipient. During sputtering, material is removed from the target by bombarding the target with energetic ions that are accelerated towards the target by an electrical field. This electric field is obtained as a result of an effective negative biasing of the target relative to the substrate. Hence, the target is called the cathode and the substrate is referred to as the anode. The "sputtered" target atoms, i.e., the removed target atoms, are supposed to condense on the substrate. A schematic view of our system is given in figure 4.1.

If a dc-voltage is applied between target and substrate, the process is called dc-sputtering. However, if the target material has a poor conductivity this would lead to accumulation of a positive charge on the target. This in turn

¹The system was set up and assembled during the PhD thesis of J.-C. Lanfranchi [39].

would compensate the applied electric field. For this reason and for the purpose of achieving a denser plasma on top of the cathode, the rf-sputtering (radio-frequency) technique is widely used today. Rf-sputtering avoids the positive charging of the cathode by applying an alternating potential. The operating frequency is 13.56MHz.

If the anode is not grounded a large capacitor is placed in series between the cathode and the rf power supply to allow a significant negative bias to develop on the cathode. In addition, it is common to use additional components, included in a "matchbox" to help to match the plasma impedance to the output impedance of the rf power supply. Usually this is done automatically by a control unit.

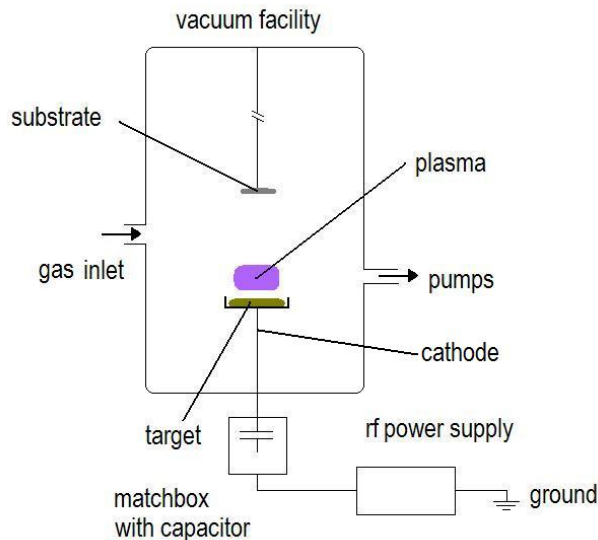


Figure 4.1: Schematic drawing of an rf-sputtering system.

Due to the high electron mobility in a plasma, an rf-system tends to build up large electron currents in the positive bias half of the rf-cycle. As the ions are much too slow to follow the applied rf-bias due to their much larger mass this results in an effective negative biasing of the cathode relative to the plasma which in turn is used for the acceleration of the ions.

In order to confine the plasma in the desired region above the target a so-called magnetron system can be used. Therefore permanent magnets are positioned below the cathode leading to a semispherical plasma over the cathode. The resulting \vec{B} field is perpendicular to the present \vec{E} field. In this way an electron confinement is produced above the cathode which results in a higher plasma density [80] (figure 4.2). The higher plasma density results in a much higher-current, lower-voltage discharge. Additionally, the enhanced plasma confinement directly above the target leads to a "cleaner" process as the ions are situated in the vicinity of the target and cannot interact with other materials. The most common design which is also used for our facility

described in section 4.2 is a planar circular design of the cathode where the cathode is a flat circular disk out of the desired target material with magnets installed below. In this case, the electrons follow circles centered on the disk axis.

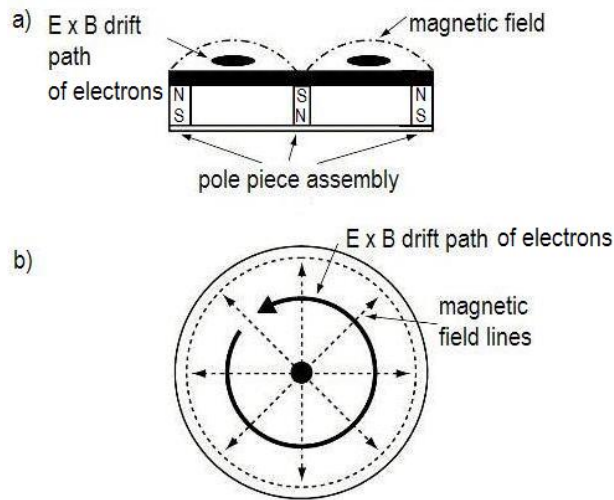


Figure 4.2: Sketch of a circular planar magnetron cathode: a) side view. b) top view.

However, due to this design the intrinsic deposition uniformity of an rf-sputtering magnetron design is not sufficient. This can be compensated by either increasing the substrate-to-target distance (in this case the sputtering rate decreases) or by including a rotatable substrate holder into the design of the facility to effectively average out the nonuniform deposition flux.

The deposition rate depends on the magnetic and electric field parameters, on the plasma density, on the target material and on the substrate-to-target distance.

4.2 Description of the Facility

The magnetron sputtering facility used in the course of this work consists of three main parts: a load lock for the introduction of the substrates, a main chamber where the deposition process takes place and the electronic and mechanical periphery (figure 4.3). Most of the electronic periphery including the control units for the pumps, the sputtering cathodes and other components of the system, as well as the read-out systems for the vacuum gauges and the resonant crystal is situated in a rack adjacent to the facility.

Each chamber is equipped with a forepump and a turbopump and can be evacuated separately. To monitor the pressures independently each chamber

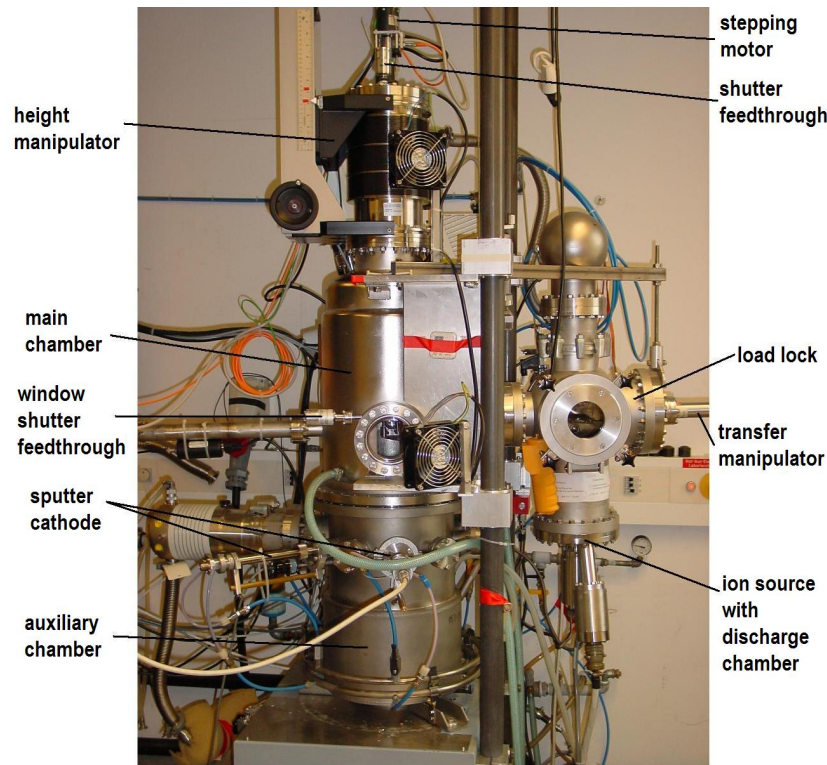


Figure 4.3: Front view of the magnetron sputtering facility. The electronic periphery is not included in the picture.

is equipped with a thermocouple gauge for coarse vacuum and an ion gauge for high to ultra high vacuum. The ion gauge of the main chamber serves also to ignite the plasma as it uses high voltage for operation.

The main chamber is double-walled and is flushed with cooling water during the sputtering process. A viewport on the frontside of the main chamber gives the possibility to monitor the substrate transfer from the load lock to the main chamber, the position of the substrate and the deposition process. To avoid vapour deposition on the window surface of the view port this viewport can be shut during the deposition process with a shutter located directly on the inside of the window. On the backside of the main chamber the gas inlet line with a tunable gas flow (the gas flow controller is situated in the electronic rack) for the sputtering gas is located. Typically, pressures of $p \sim 1 \cdot 10^{-8}$ mbar are achieved in the main chamber before the sputtering process is started. To monitor growth rate and hence film thickness during the deposition process, a water-cooled resonant crystal is mounted which is read out by a deposition monitor. In the main chamber the substrates can be heated before, during and after the sputtering process by a boron nitride heater (Boraelectric, section 4.4) that is included in the design of the substrate holder support. The substrate holder consists of an exchangeable

shadow mask made of tantalum. The substrate holder support in the main chamber also incorporates the possibility of adjusting the height of the substrate above the cathode by a versatile vacuum manipulator mounted on top of the main chamber and a shutter underneath the substrate holder that allows shadowing of the substrate from the cathode. A stepping motor [81] is added to the construction to allow rotation of the substrate holder during the deposition process. The stepping motor is controlled by a PC [81].

During deposition an auxiliary chamber can be opened to the main chamber. The auxiliary chamber, as it is equipped with a second pumping unit (turbo and forepump), is used for the reduction of the load on the main chamber pumps during sputtering. In addition, the ionisation vacuum gauge of the auxiliary chamber gives the possibility to control the pressure during sputtering.

For the purpose of monitoring the residual gases and the purity of the discharged sputter gas, a small chamber with a mass spectrometer can be connected to the main chamber and can be pumped differentially. The mass spectrometer and the ion gauge of the mass spectrometer recipient are controlled by the PC.

In the main chamber three rf-sputtering magnetron cathodes (Mighty MAK 2") are installed each of which can bear a different target material. At present, the system is only used for tungsten sputtering. The cathode in use is loaded with a tungsten target (MaTecK GmbH) with a purity of 99.95%. For the introduction of the substrate into the main chamber a load lock is used where the exchangeable substrate holder is positioned on a magnetic transfer manipulator. To introduce substrates into the main chamber the load lock itself is evacuated with a turbopump to $\sim p=10^{-7}$ mbar within a few hours. As the load lock is additionally equipped with an ion source (section 4.3), the possibility of precleaning and roughening of the substrate surface is provided in the same system as used for the deposition process. Hence, also ion etching of already evaporated films is possible in the same system. Substrate transfer to the main chamber is realised via the vacuum manipulator [81].

4.3 Operation of the Ion Source

The ion source (Ion Tech. INC. MPS 3000PBN - 3cm) is mounted on the lower part of the load lock (figure 4.3), opposite to the substrate surface, and is used for precleaning or roughening of substrates before the deposition process. The ion source is operated in combination with a PBN, a Plasma Bridge Neutraliser, in order to achieve neutralisation of the plasma and to avoid charging of the ion-irradiated surface. As the ion source and the PBN work with an argon plasma the load lock is also equipped with two gas inlet lines at the backside, each operated by a gas flow controller.

4.3.1 Working Principle

The working principle of the ion source is based on the ionisation of argon atoms that are fed into the discharge chamber by collision with electrons. Generation of these electrons (characterised by the discharge current² I_{dis}) is achieved by applying a current I_{fil} (in the range of \sim a few A) to a tungsten filament (figure 4.4). These electrons are accelerated in an electric field (discharge voltage V_{dis} , in the range of a few 10V) between the discharge cathode - the tungsten filament - and the anode - the surrounding walls of the discharge chamber. A magnetic field (generated by permanent magnets) present in the discharge chamber constrains the electrons to travel long paths from the cathode before reaching the anode. Hence, an enlarged ionisation probability is achieved. As the electrons are lighter than the ions the plasma is slightly positively self-biased ($\sim 5\text{V}$) with respect to the surrounding surfaces (anode).

The extraction of the ions from the discharge chamber is achieved by the



Figure 4.4: Tungsten filament of the ion source. The length of the filament is 2 cm.

presence of a screen grid and an acceleration grid (figure 4.5) opposite to the discharge cathode and by the fact that the discharge chamber is strongly positively biased relative to ground (V_{net} up to some 100V). The screen grid is on cathode potential and has therefore a negative potential of $\sim V_{\text{dis}}$ with respect to the plasma and allows focussing of the extracted ions. The accelerator grid is strongly negatively biased with respect to ground (V_{acc} , up to $\sim 1000\text{V}$) which results in a fast extraction of the ions from the discharge

²This current includes also secondary electrons due to the ionisation process.

chamber and additionally in a beam widening of the extracted ions. However, this potential does not contribute to the effective acceleration of the ions towards the irradiated surface. The acceleration of the ions is caused by the net potential (V_{net}) of the discharge chamber and therefore also of the plasma with respect to ground. Hence, the ion energy is determined by the net voltage V_{net} .

The ion beam current (I_{beam} , \sim some 10mA) is proportional to the ion production rate and the plasma density in the discharge chamber, but not directly connected to the ion energy and to the net voltage. However, the beam current is dependent on the total potential ($I_{\text{beam}} \sim V_{\text{tot}}^{\frac{3}{2}}$) of the ions in the discharge chamber with respect to the accelerator grid which is responsible for the ion extraction. V_{tot} is the sum of the net potential and the accelerator potential.

The ions extracted from the discharge chamber form, in principle, a positive

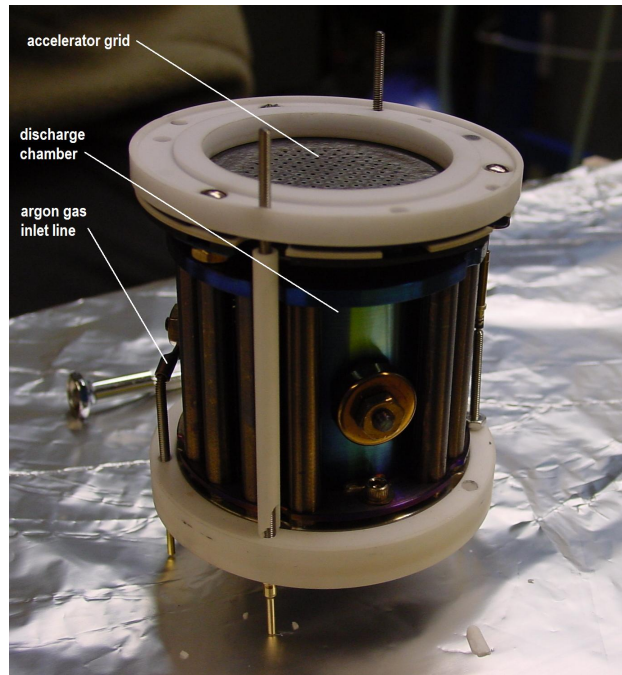


Figure 4.5: Discharge chamber of the ion source. On top the acceleration grid can be seen. The diameter of the grid is 3cm.

plasma that would lead to a strong charge buildup which in turn could effect a deterioration of the irradiated substrate surface. For this reason a plasma neutralisation has to be achieved before the plasma reaches the substrate surface. The neutralisation does not include a recombination of the plasma ions with electrons but a compensation of the electric charge of the plasma by adding free electrons. This results in an electrically neutral plasma when considered from the outside. It could in principle be achieved by placing an additional tungsten filament outside of the discharge chamber into the ion

beam which, however, would lead to disruption of the filament and to the insertion of impurities (filament atoms) to the process. Another approach, realised in our system, involves the addition of supplemental electrons with the help of an additional small plasma chamber, the plasma bridge neutraliser (PBN) (figure 4.6). This small plasma chamber is installed above the ion source perpendicular to the ion beam direction and delivers via an individual discharge process the add-electrons for the plasma neutralisation. In principle, this chamber works in the same way as the ion source itself. However, the extracted particles in this process are the electrons. The extraction is achieved by applying a negative potential (PBN body voltage, V_{PBN}) of the PBN discharge chamber relative to ground. V_{PBN} is adjusted automatically to fit the required value for the extracted electron current (PBN emission current, $I_{\text{PBN-em}}$). One should take care that the extracted neutralising electron current is at least equal to or larger than the ion beam current I_{beam} to achieve an effective neutralisation. The transfer of the electrons into the ion beam is realised by a small fraction of ions extracted from the PBN discharge chamber. These lead to the buildup of a conductive bridge between the PBN discharge chamber and the ion beam.

The substrate is moved into the ion beam and out of it with the help of the magnetic transfer manipulator.

4.3.2 Operation Parameters

To operate the ion source a pressure of maximal $1.4 \cdot 10^{-4}$ mbar has to be maintained in the load lock also during argon gas flushing. The oxygen partial pressure should not exceed $5 \cdot 10^{-5}$ mbar as oxygen ions are reactive and can cause deterioration of the system. All electric parameters of the system are controlled by the MPS-3000 PBN controller which is located in the same rack as all other control units of the sputtering facility. A parameter that should be constantly monitored to avoid overcharge of the system is the discharge power $P_{\text{dis}} = I_{\text{dis}} \cdot V_{\text{dis}}$. The discharge power should not exceed 110W.

To obtain a desired ablation of surface material for a silicon or sapphire substrate of $\sim 10\text{-}15\text{\AA}$ a set of tests were performed where the thickness of the removed material was determined after ion irradiation with the help of an α -stepper. When adjusting the parameters it also had to be taken into account that the tungsten filament of the ion source had to be replaced at the beginning of this work as it was burned. The replacement filament is made of a 0.50mm tungsten wire in contrary to the originally used 0.25mm tungsten wire.

The following adjustable parameters were extracted to achieve the desired surface ablation for an irradiation time of 30 seconds (all parameters concerning the adjustment of voltage/current values are stored in Memory II of the MPS-3000 PBN controller):

- The argon gas inlet lines have to be adjusted to a flow of 2.0sccm



Figure 4.6: Complete setup of the ion source together with the plasma bridge neutraliser. On top of the ion source the acceleration grid can be seen. The PBN discharge chamber is mounted above the ion source.

(standard cubic cm, display of the gas flow controller = value in sccm times 10) for the ion source and to a flow of 1.5sccm for the PBN.

- The filament current limit (cathode current limit) is set to: Limit: $I_{\text{fil}}=2.5\text{A}$.
- The discharge current limit is set to: Limit: $I_{\text{dis}}=1\text{A}$.
- The discharge voltage is set to: $V_{\text{dis}}=70\text{V}$.
- The beam voltage is set to: $V_{\text{beam}}=300\text{V}$.
- The accelerator voltage is set to: $V_{\text{acc}}=300\text{V}$.
- The PBN filament current limit is set to: Limit: $I_{\text{PBN-fil}}=6.5\text{A}$.
- The PBN emission current limit is set to: Limit: $I_{\text{PBN-em}}=12\text{mA}$.
- The A/B-ratio (ratio of I_{fil} to I_{dis}) limit: Limit: $A/B=50\%$.

The following parameter values arise during operation due to the adjusted parameters and can be read from the display of the MPS-3000 PBN controller:

- The filament current (cathode current) adjusts to: $I_{\text{fil}} \approx 2.1\text{A}$.
- The discharge current adjusts to: $I_{\text{dis}} \approx 0.4\text{A}$.
- The beam current adjusts to: $I_{\text{beam}} \approx 8\text{mA}$.
- The accelerator current adjusts to: $I_{\text{acc}} \approx 1\text{-}2\text{mA}$.
- The PBN body voltage adjusts to: $V_{\text{PBN}} \approx 15\text{-}20\text{V}$.

After operation of the ion source the MPS-3000 PBN controller is kept switched on to assure cooling of the controller by its fans. Additionally, care should be taken to maintain the vacuum for at least 2 hours in the load lock due to the hot filament that could be degraded under normal atmosphere.

4.4 Start-up of the Substrate Heater

The substrate heater which is included in the substrate holder construction of the main chamber is a rectangular shaped BORALECTRIC® Heater Element made out of boron nitride. This heater is situated ~ 10 cm above the substrate. Substrate heating is achieved indirectly by thermal radiation. The heater controller (HC 3500 tectra) and the power supply of the heater are located in the rack to the left of the system. In order to calibrate the substrate temperature T_{sub} several tests were performed. For this purpose a Pt100 sensor was attached to a tantalum substrate holder which was placed in the holder support in the main chamber.

Tests were performed under various conditions: different target temperature levels for the substrate holder, liquid nitrogen cooling of the double-walled auxiliary chamber switched on and off, on and off water cooling of the double-walled main chamber, as well as on and off argon flow into the main chamber.

As the auxiliary chamber is also double-walled and can be cooled with liquid nitrogen we have tested if this has an effect on the temperature of the main chamber wall and of the parts connected to it, on the achieved pressure in the main chamber, and on the substrate temperature T_{sub} with respect to the heater temperature T_{htr} . Since no influence on the above mentioned parameters was observed, liquid nitrogen cooling has not been applied.

However, a test with no water cooling of the main chamber wall showed that the wall and also some parts connected to it, as e.g. the ion gauge, were strongly heated up at heater temperatures in the range needed for substrate heating. Hence, all other tests were performed with water cooling which proved to efficiently cool the wall as well as the ion gauge. However, it

was found that the view port window and the versatile vacuum manipulator needed an extra cooling provided by three fans mounted onto the facility. Most of the tests were performed with argon gas discharged into the main chamber to simulate deposition conditions under which the heater is used. The argon flow was adjusted to the maximum rate of the gas flow controller, at 9.5sccm. With this argon gas flow, the only difference observed was a slightly faster reaction of the substrate temperature to changes in the heater temperature. To ensure that the desired T_{sub} is reached and that stable conditions are maintained before the start of the deposition process, the heater has to be kept at the chosen setpoint for at least 0.5h. All the following tests were performed with argon gas flow into the main chamber (flow rate $\approx 9.95\text{sccm}$), with water cooling but without liquid nitrogen cooling.

The following parameters were extracted (stable conditions were reached after $\sim 0.5\text{h}$):

$T_{\text{sub}} [^{\circ}\text{C}]$	osc. of $T_{\text{sub}} [^{\circ}\text{C}]$	$T_{\text{set}} [^{\circ}\text{C}]$	$T_{\text{htr}} [^{\circ}\text{C}]$	osc. of $T_{\text{htr}} [^{\circ}\text{C}]$
150	± 2	235	235	± 2
200	± 5	300	300	± 5
300	± 1	440	440	± 1
400	± 5	600	600	± 5
410	± 2	610	610	± 2

Table 4.1: Substrate temperatures T_{sub} measured for different heater temperatures T_{htr} . The setpoint temperature T_{set} is controlled by a heater controller. The observed oscillations in the substrate temperature, osc. of T_{sub} , originate from oscillations of the heater temperature, osc. of T_{htr} .

Stabilisation at some substrate temperatures was difficult due to heater temperature oscillations. The cause of these oscillations were improper values of some control parameters of the heater.

Measurements were carried out without rf-power switched on. During an actual rf-sputtering process T_{sub} could be slightly higher as the values given in table 4.1 due to the energetic sputtered atoms striking the substrate surface.

4.5 The RF-Sputtering Process

For first deposition tests sapphire single crystal substrates ($10 \times 20 \times 0.43\text{mm}^3$, Fa. ESCETE Single Crystal Technology) with c-plane surface (0001 crystal orientation) and 2-epi polished surfaces were used. The substrate holder is made from tantalum with a cutout size fitting the size of the substrate. The

uncovered area of the substrate in the holder is $\sim 10 \times 17 \text{mm}^2$).

Prior to the W-film deposition, the substrates need to be cleaned to assure removal of residual magnetic and other impurities as these can affect the transition temperature, as mentioned in section 3.4. Cleaning of the substrates is performed in a class 10000 clean room using the following procedure:

- the substrate in a glass container filled with acetone is placed in an ultrasonic bath for ~ 10 minutes
- the substrate is rinsed with purified water
- the substrate is put into a glass container filled with isopropanol that is placed in an ultrasonic bath for ~ 10 minutes
- the substrate is put into a glass container filled with purified water that is placed in an ultrasonic bath for ~ 5 minutes
- the substrate is flushed with gaseous nitrogen and put into a clean box for transport purposes

Afterwards, the substrate is directly transported to the evaporation lab where it is introduced into the rf-sputtering system described in section 4.2.

To introduce the substrate into the main chamber the load lock is vented and the substrate is positioned in the tantalum substrate holder described above. The load lock is evacuated for at least 5 hours (most of the times the load lock is pumped over night) until a pressure of minimum $p \approx 10^{-7} \text{mbar}$ is reached. Subsequently the following deposition procedure is pursued:

- – ion gun precleaning/roughening is performed as described in section 4.3.2 and then the substrate is transferred into the main chamber with the help of the versatile vacuum manipulator
 - **or** if precleaning/roughening is not required the substrate is directly transferred into the main chamber with the help of the versatile vacuum manipulator
- the substrate is positioned $\sim 25 \text{cm}$ above the sputtering cathode (height manipulator set to 4.5")
- the mass spectrometer chamber is connected to the main chamber so that the residual gases can be monitored with the PC
- the substrate shutter is turned into the position where the substrate is shadowed from the cathode
- the argon gas inlet line is opened to the main chamber and the argon gas flow is adjusted to $\sim 2 \text{sccm}$ (20 on the gas flow controller display) to flush the gas inlet lines and to assure improved thermal contact between the substrate heater and the substrate

- water flushing of the main chamber double-wall and the three fans mounted on the facility are turned on
- – the substrate temperature is regulated to $T_{\text{sub},1} \approx 300^\circ\text{C}$ with a ramp of $\sim 5^\circ\text{C min}^{-1}$ (heater temperature: $T_{\text{set}} = 440^\circ\text{C}$, see section 4.4)
 - **or** the substrate temperature is regulated to $T_{\text{sub},2} \approx 410^\circ\text{C}$ with a ramp of $\sim 5^\circ\text{C min}^{-1}$ (heater temperature: $T_{\text{set}} = 610^\circ\text{C}$, see section 4.4)
- the facility is kept in this state for ~ 1.5 -2 hours
- the argon flow is increased to its maximum $\sim 10\text{sccm}$ ($p_{\text{main chamber}} \approx 3.5 \cdot 10^{-5}$)
- the matchbox unit is switched on and set to manual state (the parameters C1 and C2 are set to 112 and 140, respectively)
- the deposition monitor is switched on (as deposition element tungsten has to be chosen)
- the rf-power supply is switched on; it is necessary to wait for at least 5 minutes until the tube of the power supply is in thermal equilibrium
- the input power of the rf-power supply is carefully increased until the plasma is ignited which can be observed via the viewport (semispherical violet glow discharge plasma); the matchbox is set to automatic state
- the viewport window shutter is closed
- the ion gauge of the main chamber is switched off
- the auxiliary chamber is connected to the main chamber
- after reaching stable conditions (~ 5 minutes) the input power is further increased until the deposition monitor shows a deposition rate of 1\AA sec^{-1} (this should be the case for $P_{\text{input}} \approx 250\text{W}$)
- during the whole process the reflected power must not exceed a maximum value of $\sim 10\text{W}$ (in such a case the system should be carefully shut down and checked³)
- cleaning of the target surface is performed by sputtering for ~ 5 -10 minutes with the substrate shutter closed
- the substrate shutter is opened while the deposition monitor is set to zero so that the grown film thickness can be monitored

³This could happen, e.g., due to a short between the outer cathode ring and the target caused by loosened flakes of earlier deposited material in the main chamber

- sputtering is performed for ~ 20 minutes until a W-film thickness of 1200\AA is reached
- the substrate shutter is closed
- the rf-input power is slowly decreased until the matchbox can no longer perform a correct matching of the plasma, at this moment the matchbox is set to manual operation and the input power is set to zero
- the rf-power supply is switched off after 10 minutes to assure cooling of the supply
- the argon gas flow is stopped and the ion gauge is turned on again
- the substrate temperature is decreased at $\sim(5-10)^\circ\text{C min}^{-1}$ until $\sim T_{\text{sub}} \approx 180^\circ\text{C}$ (from this point on substrate cooling is slow and no longer determined by the heater temperature)
- the heater controller is set to 0°C and turned off
- the auxiliary chamber is disconnected from the main chamber
- the small mass spectrometer chamber is disconnected from the main chamber
- water cooling of the main chamber and the fans are turned off
- minimum ~ 5 hours later (usually this is done the next day) the substrate is retransferred to the load lock and then removed from the system

Chapter 5

Results and Properties of the Sputtered Tungsten Thin Films

With the procedure described in section 4.5 several tungsten thin films were produced. Two deposition parameters were varied for the production: ion gun precleaning/roughening and substrate temperature T_{sub} (either $T_{\text{sub},1}=300\text{ }^{\circ}\text{C}$ or $T_{\text{sub},2}=400\text{ }^{\circ}\text{C}$) during deposition. In the following the experimental techniques for the investigation of the produced tungsten thin films as well as the resulting properties of the produced thin films are presented and discussed.

5.1 Experimental Techniques

5.1.1 Contacting Tungsten Thin Films

In order to enable measurements of electrical properties of the thin films electrical contacts have to be applied. Different strategies can be pursued. One possibility is given by the deposition of additional bond pads (small thin films, e.g. out of aluminum or gold) onto the tungsten thin film. This approach has not been followed in the course of this work as the additional deposition process usually involves heating cycles and etching processes which might influence the superconducting properties. Other possibilities are the use of indium squeezed contacts or directly bonded aluminum or gold wires.

Squeezed Indium Contacts

To apply squeezed indium contacts to the tungsten thin film a circuit board and a copper holder with a cutout for the substrate bearing the thin film are used. Small portions of indium are soldered onto the board and are connected with thin copper wires to the readout circuit. The indium beadlets are attached to the thin film by pressing the board onto the thin film with the help of screws that are fixed in the copper holder. Tight contact between the indium and the film has to be established to avoid that the contacts open when the sample is cooled down. If done correctly, the indium contacts have

proven to operate successfully down to mK temperatures. Squeezed indium contacts have been used as up to now direct ultrasonic bonding onto tungsten thin films was believed to be difficult.

Direct Ultrasonic Bonding

However, in [82] it was shown that direct ultrasonic bonding onto tungsten thin films is possible with aluminum bond wires ($\varnothing=25\mu\text{m}$) for electrical contacts and also with gold bond wires ($\varnothing=25\mu\text{m}$) for thermal contacts. The bond contacts are effectuated with an ultrasonic bonding machine (Fa. Kulicke und Soffa). For transition measurements and detector operation usually four aluminum bond contacts were made for electrical contacting of the tungsten thin film.

5.1.2 $\vartheta - 2\vartheta$ Measurement

The technique used to investigate the crystal structure of the produced tungsten thin films is a $\vartheta - 2\vartheta$ measurement. These measurements were carried out in the crystal laboratory of the TUM with the help of a computer-operated two-circle diffractometer. The wavelength used is the Cu- K_{α_1} line (the Cu- K_{α_2} line also appears in the measurement and produces a peak with $\sim 12\%$ of the intensity of the peak due to the Cu- K_{α_1} line, see figure 5.1). This was determined with a calibration measurement of a pure sapphire single crystal (the same as used for the tungsten deposition process, figure 5.1).

A $\vartheta - 2\vartheta$ measurement is based on Bragg diffraction. The incident X-rays are diffracted on different crystal planes and produce a diffraction pattern with peaks. The peaks are due to constructive interference when the Bragg condition is fulfilled:

$$n \cdot \lambda = 2 \cdot d \cdot \sin \vartheta \quad (5.1)$$

where $n=(h^2+k^2+l^2)$ is an integer number and h, k, l are the Miller indices of the reflecting crystal plane, λ is the used X-ray wavelength, d denotes the interplanar distance and ϑ is the diffraction angle. Hence, the measured angle 2ϑ allows to measure the lattice constant a .

The calibration measurement of the sapphire sample showed a relative error in the determination of the lattice constant of sapphire of $\sim 0.1\%$.

5.1.3 Residual Resistance Ratio (RRR) Measurement

For the RRR measurement the dipstick described in [45] was used with indium squeezed contacts. To determine the RRR value the resistance at room temperature and at liquid helium temperature was measured. To eliminate the influence of the connecting wires four-point measurements were performed. The dipstick was read out with an AVS-47 AC resistance bridge.

5.1.4 Transition Temperature Measurement

To measure the transition temperature the sapphire substrate bearing the tungsten thin film is installed onto a copper holder with a cutout of the size of the sapphire substrate. The direct contact of the sapphire substrate to the copper holder provides the thermal contact of the tungsten film to the heat bath. First transition temperature measurements were carried out with indium squeezed contacts. The indium beadlets are squeezed onto the tungsten film by two stripes of SINTIMID® each of which is attached to the copper holder with two screws. Each stripe has a small hole in the middle to which a thin copper wire is fastened which is in contact with the indium beadlet. The copper wires are soldered onto individual solder/bond pads that are glued onto the copper holder with black Stycast®. This glue with tiny sapphire balls inserted provides the electrical isolation of the solder/bond pads from the copper holder. Alternatively, the electrical contacts can be provided by directly bonded aluminum wires that connect the tungsten thin film with the solder/bond pads.

This holder is then installed in a ^3He - ^4He cryostat (base temperature of the cryostat $\sim 15\text{mK}$) where a SQUID read out circuit (see section 2.1) is connected to the tungsten film by soldering NbTi wires onto the solder/bond pads. Additionally, a thermometer (a speer carbon resistance thermometer) and a resistance heater are screwed onto the holder and are connected to the temperature controller (LR-130 Linear Research) and the resistance bridge (LR-400 Linear Research). The holder being in good thermal contact with the thin film is stabilised at the chosen temperature.

To record the superconducting to normalconducting transition a data acquisition system on a PC connected to the read out electronics is used. The temperature is swept from a point below the transition region (film is in the superconducting state) to a point above the transition region (film is in the normalconducting state) and back to reduce the influence of hysteresis.

5.2 Results

With the techniques described above, tungsten thin films produced with the procedure presented in section 4.5 were investigated. For all films investigated in chapter 5, sapphire c-plane (0001) substrates ($10\times 20\times 0.43\text{mm}^3$) are used. The deposited film area amounts to $\sim 10\times 17\text{mm}^2$. The thickness of the film is 1200\AA . In table 5.1 important deposition parameters are summarised: The substrate temperature given in table 5.1 corresponds to the value obtained from the measurements described in section 4.4 (where no rf-sputtering was performed) and can therefore only give a lower limit for the actual substrate temperature during sputtering.

film nr.	IG [y/n]	T _{sub} [°C]
081106	n	300
151106	y	300
241106	n	400
170107	y	400

Table 5.1: Deposition parameters of the tungsten thin films investigated in section 5.2. The first column gives the number of the film. The second column tells if ion gun precleaning/roughening (IG) was performed. The substrate temperature T_{sub} during deposition is depicted in the last column. All other deposition parameters (see section 4.5) are kept the same.

5.2.1 $\vartheta - 2\vartheta$ Measurements

The $\vartheta - 2\vartheta$ measurements were carried out as described in section 5.1. The scanned 2ϑ range covers the angular region from 35 to 45° in steps of 0.02° with 10 seconds recording time in each step. In figure 5.1a) a reference measurement of the sapphire single crystal substrate and in b) the measurement of the tungsten thin film "081106" are depicted.

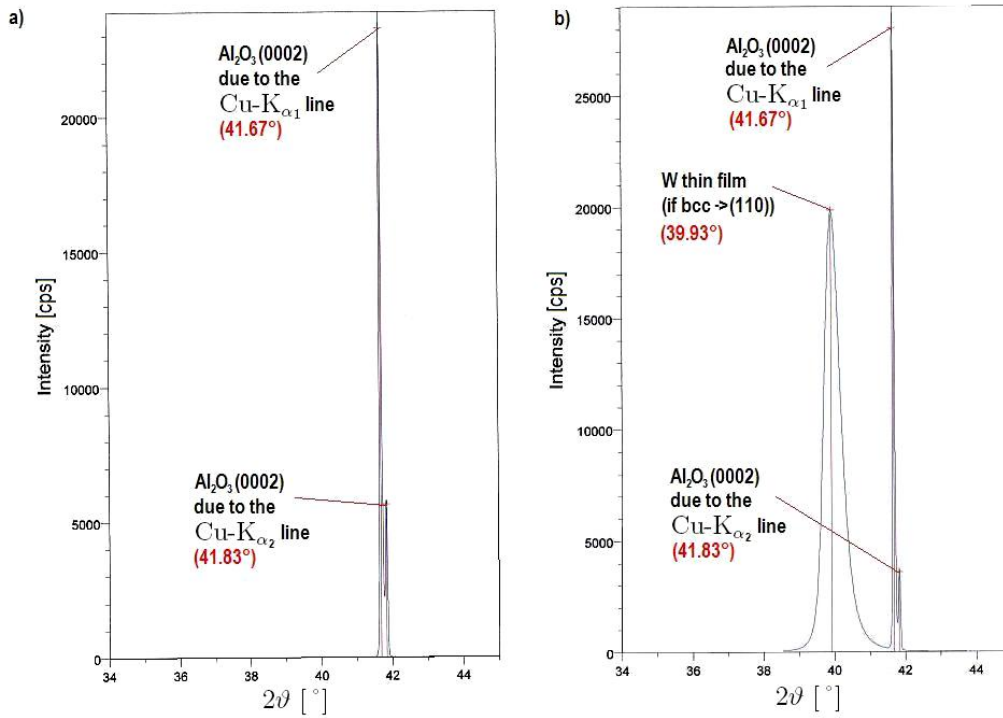


Figure 5.1: $\vartheta - 2\vartheta$ measurements of a) a sapphire single-crystal substrate (c-plane) and b) the tungsten film "081106" sputtered onto a sapphire single crystal (c-plane). In picture a) the two peaks due to the two Cu-K_α lines diffracted by the (0002) sapphire lattice planes (FWHM ~ 0.07) can be seen. Picture b) shows the same two peaks and additionally one broad peak (FWHM ~ 0.54) due to diffraction by lattice planes of the tungsten thin film. This broad peak includes diffraction on the W lattice planes due to both Cu-K_α lines.

Table 5.2 shows a summary of the results for the 2ϑ values of the peak, its full width at half maximum (FWHM), for the interplanar distance d and the lattice constant a of the thin W films assuming the α -W (bcc) structure. The d values have been calculated via equation 5.1 using the wavelength of the Cu-K_{α1} line. The assumption of a bcc-lattice structure leads to $n=2$ in equation 5.1 and the diffracting lattice planes are given by the Miller indices (110) or iterations thereof.

film nr.	2ϑ [°]	peak FWHM	d [Å]	a (bcc) [Å]
081106	39.93	0.54	2.26	3.19
151106	40.04	0.55	2.25	3.18
170107	40.03	0.55	2.25	3.18
Al ₂ O ₃ substrate	41.67	0.07	-	-

Table 5.2: Results for various W thin films and a sapphire substrate. The full width at half maximum (FWHM) values of the 2ϑ peaks of the W thin films is much larger than that of the sapphire substrate. The last two columns give the interplanar distance d and the lattice constant a assuming that an α -W structure is present. The last line gives the corresponding results for a sapphire single-crystal substrate (c-plane) as reference. An upper limit for the systematic error of the 2ϑ values is estimated from the difference between the 2ϑ results obtained by different fit methods: a cognitive and a parabolic fit. This difference yields $\sim 0.02^\circ$. From this value it can be seen that within the error bars the measured 2ϑ values for "081106" and "151106" (or "170107") can be separated.

5.2.2 Residual Resistance Ratio

The residual resistance ratio was measured with indium squeezed contacts (four-point measurement) as described in section 5.1. Measurements at liquid helium temperature were carried out by inserting the dipstick into a liquid helium dewar. In table 5.3 the measured resistances at room temperature (300K) and at liquid helium temperature (4.2K) and the RRR-value calculated with equation 3.5 are given:

film nr.	R_{300K} [Ω]	$R_{4.2K}$ [Ω]	RRR value
081106	1.07	0.72	1.48
151106	1.09	0.75	1.45
241106	0.81	0.51	1.59
170107	1.08	0.73	1.47

Table 5.3: Measured room temperature and helium temperature resistances R_{300K} and $R_{4.2K}$ for various W thin films. The error is estimated to be 0.01Ω . The resulting RRR values calculated with equation 3.5 are given in the last column. The error for RRR is about 0.02Ω .

5.2.3 Specific Resistivity

To determine the specific resistance of the sputtered tungsten thin films the resistances measured to derive the residual resistance ratio were used. The

specific resistance ρ is calculated according to the equation:

$$\rho = R \cdot \frac{A}{l} \quad (5.2)$$

where R is the resistance (four-point measurement, in $[\Omega]$), A (in $[\text{cm}^2]$) is the cross-section and l (in $[\text{cm}]$) is the length of the measured conductor. Hence, the geometry used for the four-point measurement has to be incorporated in the calculations. Figure 5.2 shows a sketch of the geometry used for the four-point-measurements with squeezed indium contacts:

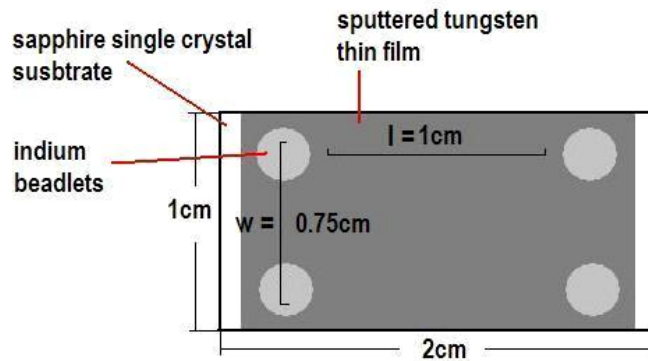


Figure 5.2: Sketch of the geometry used for the four-point resistance measurement of the sputtered tungsten thin film (film thickness $d=1200\text{\AA}$, length $l=1\text{cm}$, cross-section $A\approx 9\cdot 10^{-6}\text{cm}^2$).

For a conservative estimate (here, a large value is considered conservative) of the specific resistance ρ we took:

$$A = d \cdot w \approx 1200\text{\AA} \cdot 0.75\text{cm} = 9 \cdot 10^{-6}\text{cm}^2 \quad (5.3)$$

$$l \approx 1\text{cm} \quad (5.4)$$

where $d=1200\text{\AA}$ is the film thickness, w and l are the shorter and longer distances between the indium beadlets (see figure 5.2), respectively. With these values for A and l the resistance values R_{300K} and $R_{4.2K}$ from section 5.2.2 and equation 5.2 the specific resistance values ρ_{300K} and $\rho_{4.2K}$ for the sputtered tungsten thin films are estimated. The results are summarised in table 5.4.

film nr.	R_{300K} [Ω]	ρ_{300K} [$\mu\Omega\text{cm}$]	$R_{4.2K}$ [Ω]	$\rho_{4.2K}$ [$\mu\Omega\text{cm}$]
081106	1.07	9.60	0.72	6.49
151106	1.09	9.84	0.75	6.78
241106	0.81	7.25	0.51	4.55
170107	1.08	9.72	0.73	6.60

Table 5.4: Measured resistances R_{300K} and $R_{4.2K}$ for various W thin films are given. The resulting specific resistances ρ_{300K} and $\rho_{4.2K}$ for a conservative estimate (large values) calculated with equation 5.2 are also presented. The error for the resistivity is about $0.09\mu\Omega\text{cm}$. Therefore, the value for film "241106" is clearly distinguishable within the error bars.

5.2.4 Transition Temperature

Transition temperature measurements were carried out as described in section 5.1. For each film a transition temperature measurement was performed using squeezed indium contacts. Film "241106" was also measured with directly bonded contacts (Al wires, $\varnothing=25\mu\text{m}$).

In table 5.5 the results for the measured transition temperatures T_c of the sputtered tungsten thin films, the width of the transitions ΔT_c and the difference in resistance of the normal to the superconducting state ΔR are summarised. Film "170107" did not show a transition to the superconducting state down to the cryostat's base temperature of $\sim 15\text{mK}$. Hence, no T_c value for this film could be obtained.

film nr.	contact form (SI/DB)	T_c [mK]	ΔT_c [mK]	ΔR [Ω]
081106	SI	46	4	~ 0.5
151106	SI	34	2-3	~ 0.5
241106	SI	40	1-2	~ 0.8
241106	DB	38	1-2	~ 1.1
170107	SI	≤ 15	-	-

Table 5.5: Transition temperatures T_c measured for various W thin films in a ^3He - ^4He cryostat with a base temperature of $\sim 15\text{mK}$. The measurements were carried out either with squeezed indium (SI) or directly bonded (DB) contacts. Additionally, the width of the transition ΔT_c and the difference in resistance ΔR of the normal to the superconducting state are given.

In figure 5.3 the transitions described in table 5.5 are shown. The transition shown in figure a) is relatively broad and the normalconducting state was just reached at the endpoint of the data shown. In figure b) the slight slopes at the beginning and at the end of the data set and also the offset with respect to zero are most probably due to not perfectly established in-

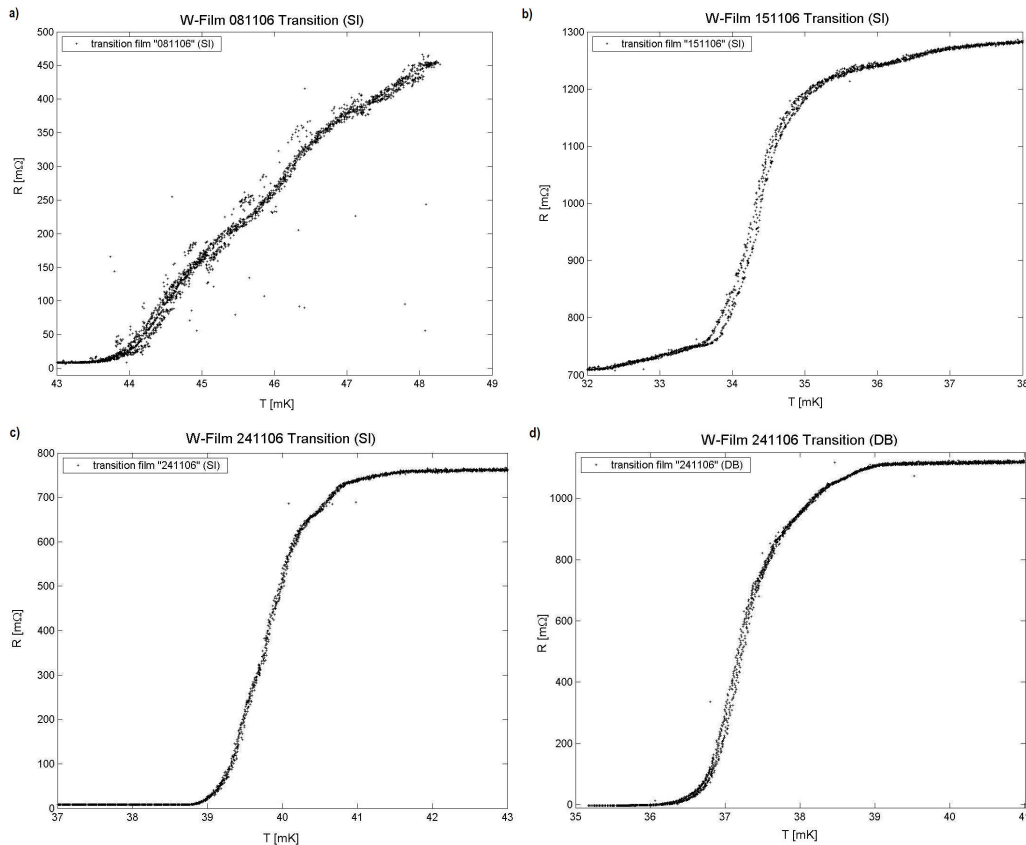


Figure 5.3: Transitions from super- to normalconducting state of the sputtered tungsten thin films "081106", "151106" and "241106". The transitions shown in figure a), b) and c) are recorded with indium squeezed (SI) contacts, while figure d) shows again the transition of the tungsten thin film "241106" this time recorded with Al wires directly bonded (DB) onto the tungsten thin film.

dium contacts. The small difference in transition temperature ($\sim 2\text{mK}$) and the difference in ΔR (the difference in resistance of the normal to the superconducting state) that can be seen in the two measurements of film "241106" can probably be explained by the different contact techniques used (with squeezed contacts and bonded contacts, respectively) and geometries used for the measurements. However, these measurements did not show any noteworthy difference in the results. Thus, with this measurement it could be demonstrated that direct bonding (DB) on tungsten thin films delivers a possibility of electrically contacting tungsten thin films equivalent to squeezed indium contacts (SI). To document the reproducibility of this technique also other measurements (see chapter 6 and 7) were carried out with directly bonded contacts.

5.2.5 Summary of Properties of the Produced Tungsten Thin Films

In table 5.6 a summary of the properties described above of the sputtered tungsten thin films is given :

film nr.	IG [y/n]	T_{sub} [°C]	2ϑ [°]	a (bcc) [Å]	R_{300K} [Ω]	$R_{4.2K}$ [Ω]
081106	n	300	39.93	3.19	1.07	0.72
151106	y	300	40.04	3.18	1.09	0.75
241106	n	400	-	-	0.81	0.51
170107	y	400	40.01	3.18	1.08	0.73
	RRR	ρ_{300K} [$\mu\Omega\text{cm}$]	$\rho_{4.2K}$ [$\mu\Omega\text{cm}$]	T_c [mK]	ΔT_c [mK]	ΔR [Ω]
081106	1.48	9.60	0.72	46	4	~ 0.5
151106	1.45	9.84	0.75	34	2-3	~ 0.5
241106	1.59	7.25	0.51	40	1-2	~ 0.8
170107	1.47	9.72	0.73	≤ 15	-	-

Table 5.6: Properties of the produced tungsten thin films. The different columns contain the following information: iongun precleaning/roughening (IG), substrate temperature during deposition (T_{sub}), measured angle 2ϑ , calculated lattice constant a for α -W structure (bcc), measured room temperature and liquid helium temperature resistances R_{300K} and $R_{4.2K}$, residual resistance ration (RRR), estimated specific resistivity at room temperature (ρ_{300K}) and at 4.2K ($\rho_{4.2K}$), the measured temperature (T_c) and width (ΔT_c) of the superconducting transition and the difference in resistivity ΔR between super- to normalconducting state. Concerning the error bars for the individual values see tables 5.1 to 5.5.

5.3 Discussion

In the following the results obtained for the sputtered tungsten thin films described in section 5.2 are discussed and interpreted in terms of the production parameters, the crystal structure, and the measured superconducting transition temperatures and the width of the transitions. Clearly, since only relatively few W thin films have been investigated our results hardly provide conclusive information but certainly show badging trends.

5.3.1 Production Parameters

From table 5.6 several deductions can be made:

- ion source precleaning/roughening:

the film produced with ion source application seems to exhibit

- a slightly less tensile stressed crystal structure
- a lower residual resistance ratio
- a higher specific resistivity
- a lower transition temperature
- a sharper transition

⇒ thin film production with ion source application seems to lead to a slightly lower "crystalline" quality of the tungsten thin film but to a lower T_c and a sharper super- to normalconducting transition as the crystal lattice seems to be slightly less stressed (for an explanation, see section 5.3.3).

- substrate temperature:

the film produced at a higher substrate temperature seems to exhibit

- a higher residual resistance ratio
- a lower specific resistivity
- a lower transition temperature
- a sharper transition

⇒ thin film production at a higher substrate temperature seems to lead to a lower T_c and a sharper super- to normalconducting transition, i.e., the "crystalline" quality of the tungsten thin films is better.

5.3.2 Crystal Structure

In the following the obtained results are discussed with respect to the lattice structure (α -W, β -W or γ -W), the stress state (tensile or compressed) and the growth mode (epitaxial or grained) of the tungsten thin film.

Lattice Structure

A peak at a 2ϑ -angle of $\sim 40^\circ$ could be attributed to the investigated sputtered tungsten thin films (see section 5.2.1). According to chapter 3, for the α -W structure the peak at 40.26° is due to diffraction at the (110) lattice planes while for the β -W structure the peak at 39.87° is due to diffraction at the (012) lattice planes. Both these values do not fit exactly the measured ones of the produced tungsten thin films.

Hence, from the ϑ - 2ϑ measurement of the investigated tungsten thin films "081106", "151106" and "170107" no definitive statement concerning the presence of the α -W or the β -W structure can be made.

To further investigate the presence of particular lattice structures the specific

resistivity values calculated from the resistance measurements can be used. As described in chapter 5.2.1 the specific resistivity values differ largely for the different lattice structures. For α -W thin films specific resistivities in the range from $5.3\mu\Omega\text{cm}$ (bulk value) up to $40\mu\Omega\text{cm}$ (stressed and/or grained crystal structure) are reported while for thin films exhibiting the β -W structure the reported specific resistivities range from $100\mu\Omega\text{cm}$ up to $300\mu\Omega\text{cm}$. The estimated specific resistivity values from our resistance measurements of the sputtered tungsten thin films range from $7.3\mu\Omega\text{cm}$ up to $9.8\mu\Omega\text{cm}$. These values which were obtained with a conservative estimate clearly indicate that the produced tungsten thin films exhibit the α -W structure.

However, the specific resistivity values do not correspond exactly to the value given for an epitaxially grown α -W thin film of $5.3\mu\Omega\text{cm}$. This difference could be due to various mechanisms. First, as indicated in section 3.3.2, the size effect could have an impact on the specific resistivity via the film thickness t that could diminish the mean free path l of the electrons. Equation (3.4) provides an estimate of the specific resistivity for films with thickness t . When evaluating this equation with the film thickness of the produced tungsten thin films of $\sim 1200\text{\AA}$ and a mean free electron path of $l \approx 40\text{nm}$ (bulk value) one find a value of $\sim 5.96\mu\Omega\text{cm}$ for the produced tungsten thin films. This value is still smaller than the measured ones given in table 5.6. Hence, also other mechanisms not included in equation 3.4 seem to play a role in diminishing the electron mean free path and therefore increasing the specific resistivity of the produced tungsten thin films. As already described in section 3.3.2 also scattering from impurities and grain boundaries can deliver such a mechanism. Thus, the thin films can either contain impurities and/or are grown in a grained structure. For further discussion see the section on growth mode below.

Stress State

Assuming an α -W structure for the thin films the lattice constants measured are a factor of ~ 1.005 - 1.008 larger than the bulk values which indicates a tensile stressed lattice structure.

As described in [78] a high residual stress such as the one found for the produced thin films can eventually be linked to the working-gas (here Argon) pressure during deposition. The working-gas pressure influences the particle transport process from the target to the substrate in terms of the energy of the sputtered atoms and the directionality. This becomes clear when regarding elevated working-gas pressures (1) in comparison to low working-gas pressures (2): (1) results in a denser plasma and working-gas region and therefore in more scattering events of the sputtered atoms than in (2). An increase of the scattering rate, however, results in a lower energy and less directionality of the sputtered atoms incident on the substrate surface. This in turn promotes an open, porous growth mode of the thin film and therefore

tensile stress being present in the thin film [78]. Low working-gas pressure on the other hand supports high energy transfer to the substrate and high mobility of the sputtered atoms on the surface and therefore compressive stress present in the growing thin film [78]. The energy of the incident atoms can, however, also be increased by an increase in rf-sputtering power.

However, the stress of a deposited thin film is of course also influenced by the lattice structure of the underlying substrate surface.

Hence, the observed tensile stress present in the produced tungsten thin films can perhaps, to some extent, be explained by a relatively low energy transfer and low mobility of the tungsten atoms on the sapphire substrate surface.

Growth Mode (epitaxial/grained)

Moreover, the ϑ - 2ϑ measurements show that the width (FWHM) of the observed W-peaks (~ 0.55) is quite large in comparison to the width (FWHM) of the peak (~ 0.07) obtained for a single crystal sapphire substrate (see section 5.2.1). This difference can be explained by a nonepitaxial and probably inhomogeneous¹ growth of the tungsten thin films. Therefore, the conclusion can be drawn that the produced tungsten thin films consist of grains.

In addition, the RRR-value, as reported in chapter 5.2.1, can be used as a measure for the crystalline quality in terms of crystal defects, grain boundaries and inhomogeneities present in the thin film. A residual resistance ratio of ~ 1.5 is calculated from the measured resistances for the sputtered tungsten thin films. Hence, another evidence for the existence of grains and inhomogeneities in the tungsten thin films is delivered by this relatively small RRR-value.

Taken together these results indicate that the produced tungsten thin films form a grained, tensilely stressed and probably inhomogeneous α -W structure. As described in the following section these results are consistent with the measured transition temperatures.

5.3.3 Transition Temperatures

Influence of the Lattice Structure

As can be seen from table 5.6 all measured transition temperatures range well below the transition temperatures which would be expected for thin films exhibiting the β -W or γ -W structure (T_c in the range of 1-4K or, respectively, up to 6K). Hence, the transition temperatures indicate in agreement with the discussion in the previous section that the produced tungsten thin films

¹The inhomogeneous growth can be related to the production process of the investigated tungsten thin films as the rf-sputtering process contains an intrinsic deposition uniformity as described in section 4.1 especially as no rotation of the substrate holder was applied.

exhibit or at least mainly consist of the α -W structure.

However, the measured transition temperatures do not correspond to the value obtained for a pure, unstressed and undisturbed tungsten thin film of $\sim T_c=15\text{mK}$ as reported in section 3.4. The measured elevated transition temperatures can be attributed to different mechanisms.

As reported in section 3.4, a small abundance of the β -W structure in a mainly α -W structured tungsten thin film can lead to a higher transition temperature. However, the produced tungsten thin films are very likely to exist in a pure α -W structure. Hence, the observed elevated transition temperatures cannot be explained by a simultaneous existence of the β -W structure.

Indeed, in section 3.4, elevated transition temperatures of up to $\sim 66\text{mK}$ for pure α -W thin films are reported to occur in accordance with the measured transition temperatures. As depicted there, stress acting on the lattice structure (tensile or compressive) of the thin film and also the crystallinity of the thin film (grains or inhomogeneities) can have an impact on the transition temperature (increasing or decreasing).

In the present case of tungsten thin films produced with a magnetron rf-sputtering technique it has to be kept in mind that especially this technique can lead to inhomogeneous films due to an intrinsic deposition non-uniformity of the sputtering technique (see section 4.1).

Influence of Stress present in the Thin Film

Equation (3.6) describes the correlation of the transition temperature with different parameters that are influenced by a stressed crystal lattice. As a result, for a compressed crystal lattice (decreased lattice constant) a decreased transition temperature while for a tensile stressed crystal lattice (increased lattice constant) an increased transition temperature can be expected. For the investigated sputtered tungsten thin films the discussion in the previous section indicated that the crystal lattice of the produced tungsten thin films is subject to a tensile stress. Therefore, elevated transition temperatures in comparison to the "unstressed" value of $\sim 15\text{mK}$ are expected. This is exactly what can be observed with our investigated tungsten thin films.

When examining the values of the lattice constant a and the transition temperature T_c given in table 5.6 it is possible to see this correlation: film "081106" exhibits the largest lattice constant (the largest tensile stress) and also the highest transition temperature T_c .

Influence of the Crystal Quality of the Thin Film

Additionally, the crystallinity of the tungsten thin film in terms of grain size or crystal defects can have an impact on the transition temperature. As de-

scribed by equation (3.7), a decrease of the Cooper-pair coherence length can result in an increased T_c . Therefore, the RRR value which can probably be connected to the coherence length, as already described in section 3.4, could be associated with the transition temperature: A very small RRR value could e.g. be associated to a very small grain size. A very small grain size could, on the other hand, diminish the coherence length of the Cooper-pairs and therefore result in an increase of the transition temperature.

However, the rather low specific resistivities that are measured for the tungsten thin films do not indicate very small grains to be present in the thin films, because very small grains present in the thin film would decrease the mean free path of the electrons and therefore increase the specific resistivity. Hence, it is not surprising that no dependency of the transition temperature on the RRR value can be observed when considering the measurements presented in table 5.6.

Still, the width of the transition ΔT_c could also be strongly dependent on the "crystalline" quality of the thin film. As an example, when comparing ΔT_c of film "241106" (largest RRR value) with the ΔT_c s of the films "081106" and "151106" (smaller, \sim similar RRR values) (see table 5.6), it can be seen, that ΔT_c decreases with an increasing RRR value. Hence, it is concluded that a lower "crystalline" quality of the thin film leads to a broader transition.

In summary, the produced tungsten thin films - despite exhibiting the α -W structure - show transition temperatures slightly elevated in comparison to the T_c value expected for a pure, unstressed, epitaxially grown α -W film. This enhancement in the transition temperature can most probably be associated with the observed tensile stressed lattice structure of the produced tungsten thin films. The width of the transitions on the other hand seems to be correlated to the crystalline quality, in particular to grains and inhomogeneities present in the thin film.

5.3.4 Conclusions

Taking all these results together it can be concluded that the measured transition temperatures and the width of the transitions can be linked successfully to crystal structure properties of the tungsten thin film. Concerning the impact of the deposition parameters on the width and temperature of the super- to normalconducting transitions of the sputtered tungsten thin films the following results have been obtained:

A higher substrate temperature seems to lead to a higher crystalline quality of the thin film and therefore to a sharper transition. The higher substrate temperature also appears to lead to a decrease in the transition temperature. The application of ion source precleaning/roughening leads to a slightly lower crystalline quality of the thin film, however, it seems to allow the growth of a

thin film which is less stressed. Actually, the lower crystalline quality would probably tend to result in an increased transition temperature and an increased width of the transition. However, the less stressed crystal lattice generates a decreased transition temperature and a decreased width. From the data presented in the previous sections the conclusion can be drawn that the influence of the less stressed crystal lattice seems to dominate the influence of the lower crystalline quality. Hence, the transitions of tungsten thin films produced with ion source application occur at lower temperatures than the transitions of tungsten thin films produced without ion source application.

As a result and a consequence it can be stated that in order to produce tungsten thin films with transition temperatures of $\sim 15\text{mK}$ and a transition width of $\sim 1\text{mK}$ as required e.g. for the CRESST experiment (chapter 2) some production parameters need to be adjusted. Various possibilities arise from the discussion above. The substrate or the substrate surface orientation used for the deposition could be changed so that the substrate surface where the thin film is grown on exhibits a different lattice structure. This could lead to a change in the growth mode respectively in the stress state of the thin film. Another possibility would be to modify the deposition parameters. The substrate temperature during deposition could be increased which would probably lead to a higher crystalline quality of the thin film. As the working-gas pressure cannot be further increased with the present device, an attempt to decrease the energy, the mobility and the directionality of the tungsten atoms on the substrate surface and therefore to suppress a tensile stressed growth mode could be to decrease the applied rf-power. The substrate-to-cathode distance could be increased so that the rf-sputtering cathode is more likely to act as a point source which would decrease the intrinsic non-uniformity of the sputtering technique and therefore lead to a more uniform film growth. Substrate holder rotation during the sputtering process could be applied to additionally average out the nonuniform deposition flux. Annealing after the sputtering process of the tungsten thin films could be applied to support growth of the tungsten thin film with less and bigger grains, less stress, and/or less crystal defects.

Chapter 6

Production and Properties of "Small" Tungsten Thin Films

6.1 Motivation

As described in section 2.2 the usual procedure to fabricate a TES from a tungsten thin film would include photolithographical and etching processes of the produced tungsten thin films. These postprocessing steps were observed to frequently have an uncontrolled impact on the measured transition temperature¹ of the tungsten thin film [45]. Mostly the transition widths are smaller after the structuring processes while the transition temperatures are lower.

To exclude this unpredictable influence on the transition temperatures it is attempted to initially produce tungsten thin films of a smaller size with a specially designed shadow mask so that these films can directly be used as TESs. The realisation of this idea and the obtained results are presented in the following sections.

6.2 Production

In order to directly produce smaller tungsten thin films a different tantalum shadow mask² (figure 6.1) is used. The design of the shadow mask allows production of eight "small" thin films of circular shape each with a diameter of $\sim 2\text{mm}$ on "small" crystal substrates of $3 \times 5\text{mm}^2$ size in a single batch. The fact that the tungsten thin film is deposited onto such a small crystal substrate has two advantages. First, the utilisation of small crystal substrates allows the production of eight tungsten thin films at the same time.

¹In the majority of cases the observed "change" in transition temperature is probably due to structuring processes where one small part of a large tungsten thin film is chosen. The small remaining part very likely exhibits a much more uniform crystal lattice and therefore probably narrower and lower transitions.

²This shadow mask was originally designed and used for the production of small iridium-gold TESs [83].

Additionally, the TESs deposited on the small crystal substrates can be used directly for the assembly of the composite detectors described in chapter 7.



Figure 6.1: Tantalum shadow mask used for the production of the "small" sputtered tungsten thin films. The substrate holder with the exchangeable shadow mask can be seen. The positions for the eight substrates are shown, corresponding to the film numbers of the produced film (see section 6.3). One cutout can accommodate a substrate of $3 \times 5 \text{ mm}^2$. The unsealed area for each film is given by a circle with a diameter of $\sim 2 \text{ mm}$.

One batch of eight "small" tungsten thin films was produced (in the following referred to as "210207-X", where X denotes the number of the tungsten thin film within the batch) on small c-plane (0001) sapphire substrates of $3 \times 5 \times 1 \text{ mm}^3$ size (2-epi polished). Concerning the deposition procedure it has to be especially pointed out in this case that still no rotation of the substrate holder was applied and therefore the eight substrates covered different local positions above the sputtering cathode leading to different properties of the thin films (see section 4.1). The procedure described in section 4.5 was followed, with no ion-gun precleaning applied. The substrate temperature during sputtering was $T_{\text{sub}} = 400 \text{ }^\circ\text{C}$.

6.3 Results

Transition temperature measurements of the produced "small" tungsten thin films were performed in a ^3He - ^4He dilution refrigerator (base-temperature $\sim 15 \text{ mK}$). To avoid postprocessing of the tungsten thin films the electrical contacts are provided by direct ultrasonic bonding on the tungsten thin film with aluminum wires ($\varnothing = 25 \text{ } \mu\text{m}$), as described in section 5.1.1.

Out of the eight films produced, five have been tested regarding the temperature and width of the transitions. The results are given in table 6.3.

film nr.	T_c [mK]	ΔT_c [mK]	ΔR [Ω]
220207-1	≤ 15	-	-
220207-2	63	5	~ 1.8
220207-3	28.5	1.5	~ 2.1
220207-5	40	4	~ 2.0
220207-6	54	4	~ 1.2

Table 6.1: Transition temperatures of "small" sputtered tungsten thin films produced with the shadow mask described in section 6.2. Each circular film area covers a size of $\sim 12 \text{ mm}^2$. T_c was measured in a ^3He - ^4He dilution refrigerator (base-temperature: $\sim 15 \text{ mK}$). ΔT_c denotes the width of the transition and ΔR the difference in resistance from the normal to the superconducting state.

In figure 6.2 the transitions described in table 6.3 are shown.

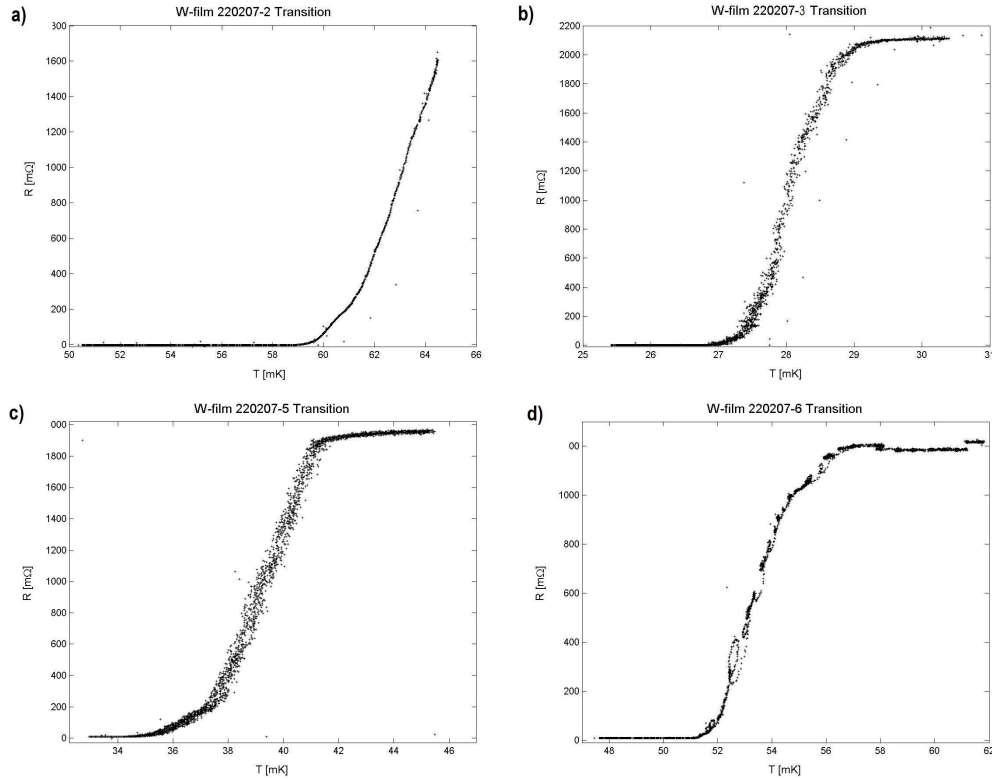


Figure 6.2: Transitions from super- to normalconducting state of the sputtered tungsten thin films "220207-2,3,5,6". For the transition of film "220207-2" shown in figure a) the normalconducting condition was reached at approximately the endpoint of the shown dataset. The transition of film "220207-6" shown in figure d) looks a bit irregular which can be assigned to the process of data taking and the performance of the utilised SQUID.

6.4 Discussion

The produced films show different transition temperatures T_c and widths of the transitions ΔT_c although produced in one batch.

As already mentioned, during the deposition process no substrate holder rotation was applied. Hence, the differences in the observed transition temperatures can most probably be associated with the different local positions of the small sapphire substrates above the sputtering cathode during the deposition process. To achieve more uniform properties of the different tungsten thin films produced in one batch, the same methods could be applied as suggested in section 5.3.4 to obtain a more uniform growth of the "big" tungsten thin films.

The mentioned methods are (summarised): increased substrate-to-cathode distance, substrate holder rotation and annealing of the tungsten thin film after deposition.

The relatively low T_c value and sharp transition of film "220207-3" look very promising. In the context of the composite detector design which is described in the following chapter, the produced "small" tungsten thin films have the advantage that they can be directly used as TESs without any postprocessing steps.

Chapter 7

Composite Detectors

Using the "small" tungsten thin films described in chapter 6 two so-called composite detectors (CD) were realised. The composite detector design (CDD), which was already used to built detectors in [39] and [40], has been investigated here as it allows decoupling of the TES production from the choice of the absorber material. Applying this technique offers several advantages as discussed in section 7.1.2.

7.1 Composite Detector Design (CDD)

7.1.1 Basic Design

For the purpose of realising a composite detector, a TES is deposited onto a small crystal substrate (in the following: "TES-substrate") which is then glued onto a bigger absorber crystal [39, 40]. Hence, the glue used should exhibit properties that allow an effective phonon transport from the absorber crystal to the TES. For the realised composite detectors investigated in sections 7.2 and 7.3 two different glueing techniques were applied: for one detector (in the following: "detector 1") only a small glue spot of $\sim 0.7\text{mm}$ diameter was used while for the second detector (in the following: "detector 2") the new technique of a plain layer of glue of the size of the TES-substrate (15mm^2) was applied. A sketch of the principle design with the two different glueing techniques is given in figure 7.1.

7.1.2 Advantages of the Application of the CDD

The approach of decoupling the TES and the TES production process from the absorber crystal offers several advantages. Direct Dark Matter search experiments require big target masses (see chapter 1). For Dark Matter experiments using cryogenic detectors with TESs as, e.g., the CRESST experiment, this usually implies the operation of several detector modules. As mentioned in section 2.1 this is due to the fact that in order to maintain a reasonable sensitivity of the detector it is not possible to arbitrarily scale up

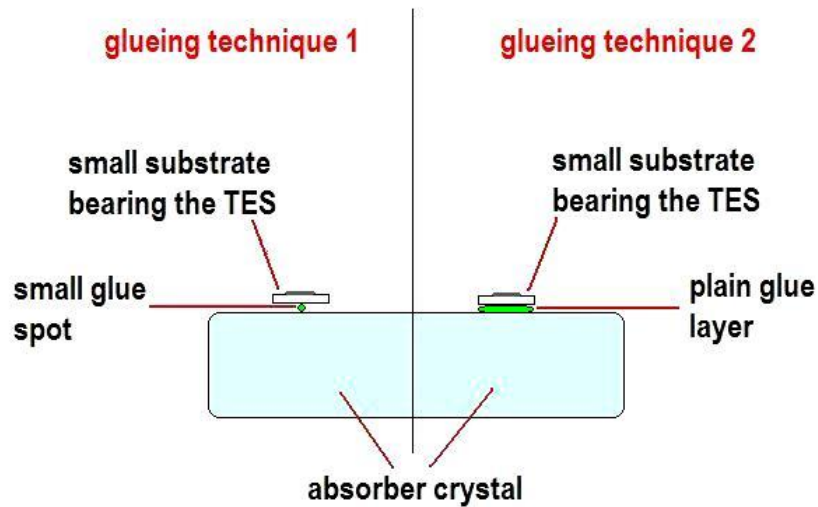


Figure 7.1: Sketch of the composite detector design applied for the detectors investigated in sections 7.2 and 7.3. The absorber crystal with the attached small TES-substrate can be seen. For the "glueing technique 1" a small glue spot is used while for the "glueing technique 2" a plain layer of glue of the size of the TES-substrate is applied.

one detector module in size. Hence, a reproducible production of the detector modules and therefore of the TESs is needed.

The CDD allows a separate production of the TES which can be investigated independent of the absorber crystal and then selected concerning the desired properties, like transition temperature and width of the transition.

Additionally, as already realised with the production of the "small" tungsten thin films (chapter 6), it is possible to produce a whole batch of W-TESs in the same production process. Up to now, it has not yet been achieved that all individual tungsten thin films of one batch exhibit more or less the same properties. However, in section 6.3 several techniques are presented that could lead to the aimed at result.

A further advantage provided by the CDD is that the TES production process is completely independent of the chosen absorber material. Especially concerning the CRESST detectors, where the absorber material is CaWO_4 , another advantage emerges. With the TES production on separate crystal substrates heating of the absorber material during the deposition process is avoided. This is of great interest as CaWO_4 is known to suffer during the deposition process from oxygen loss due to heating of the crystal which, in turn, lowers the light output and therefore the discrimination capabilities of the crystal [84].

As described in [83] the CDD has the additional advantage of electrically decoupling the TES from the absorber crystal. This is important concerning the application of the Neganov-Luke effect [85] where a voltage is applied to

a semiconductor absorber crystal which could otherwise influence the TES operation.

7.1.3 Setup of the Two Realised Composite Detectors

For the two detectors realised and investigated in this chapter two "small" tungsten thin films ("220207-3" and "220207-6", see table 6.3 and figure 6.2) which were sputtered onto the c-plane surface (0001) of small sapphire substrates ($5 \times 3 \times 1 \text{ mm}^3$) are used. Applying the two different glueing techniques mentioned above these tungsten thin films on the small sapphire substrates (W-TES-3 and W-TES-6) are glued onto two different absorbers and are operated as TESs. An epoxy resin (Epo-Tek 301-2)¹ was used.

For "detector 1" the W-TES-3 was glued onto a sapphire crystal of $10 \times 20 \times 1 \text{ mm}^3$ size which is used as absorber, while for "detector 2" the W-TES-6 was glued onto a CaWO_4 crystal² of cylindrical shape with a diameter and a height of 20mm acting as the absorber.

A sketch of a composite detector with its electrical and thermal connections can be seen in figure 7.2. The composite detector is fixed inside a copper holder where the absorber crystal is supported by either sapphire balls ("detector 1") or Teflon supports ("detector 2"). In this way, a thermal decoupling of the absorber crystal from the copper holder is achieved.

Thermal and electrical contacts of the TES are realised with bonded gold and directly bonded aluminum wires ($\varnothing = 25 \mu\text{m}$) as described in section 5.1.1. The aluminum wires connect the tungsten TES with electrically insulated solder/bond pads on the copper holder to which also the wires of the SQUID read-out circuit are soldered. The gold wires connect the TES to the copper holder, which in turn is thermally coupled to the mixing chamber of the cryostat and thus serves as a heat sink for the TES. In principle, all contacts could be implemented by the use of only one aluminum or gold wire, respectively. However, always a pair of wires is used in order to decrease the risk of an open contact due to loosening of one wire during cool-down³.

The read out of the detectors is realised via a SQUID circuit (see section 2.1) in electro-thermal feedback mode [42]. Temperature stabilisation of the TES is achieved with the help of a heater and a temperature sensor (speer resistor) that are attached to the copper holder. The heater and the speer resistor are connected to a temperature controller (TS-530A Temperature Controller) and a resistance bridge (AVS-47 AC Resistance Bridge). Being

¹This glue was investigated in [39], especially concerning its suitability for the application in a composite detector design.

²This crystal was produced in our group using the Czochralski technique [86].

³During cool-down of the detector it is possible that due to vibrations or different thermal contraction of the used materials a wire used for the TES contacting becomes loose.

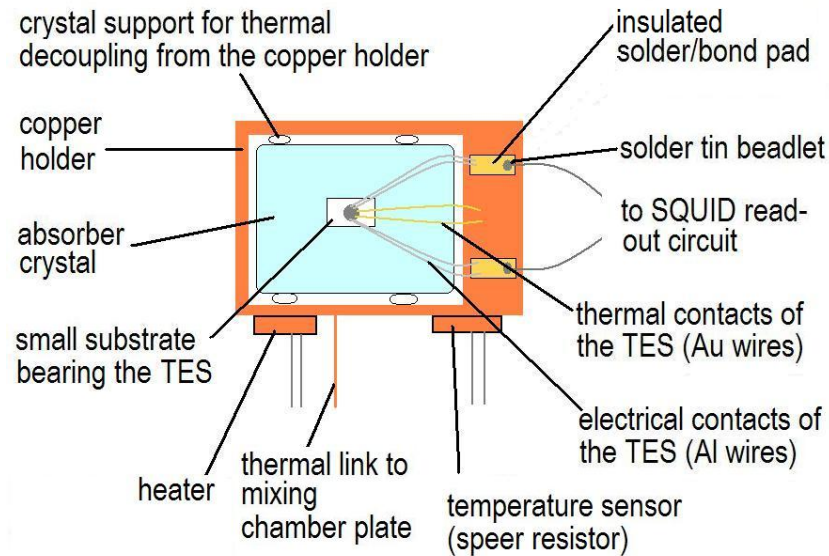


Figure 7.2: Sketch of a composite detector inside a copper holder. The crystal is supported in such a way that it is thermally decoupled from the holder. The TES (on the small substrate) with its electrical and thermal contacts (bonded Al wires to insulated solder/bond pads on the copper holder and Au wires to the copper holder) can be seen. The copper holder is thermally coupled to the mixing chamber and therefore serves as heat bath for the TES. Additionally, the temperature sensor (speer resistor) and the resistance heater that are used for temperature stabilisation of the TES are indicated.

in good thermal contact with the copper holder via the gold wires, the TES can be stabilised to a chosen temperature in the middle of its super- to normalconducting transition.

In figure 7.3 the composite "detector 1" and "detector 2" can be seen built into the copper holder. The bonded electrical and thermal contacts are visible. Additionally, the transitions of the used W-TES-3 and W-TES-6 are given.

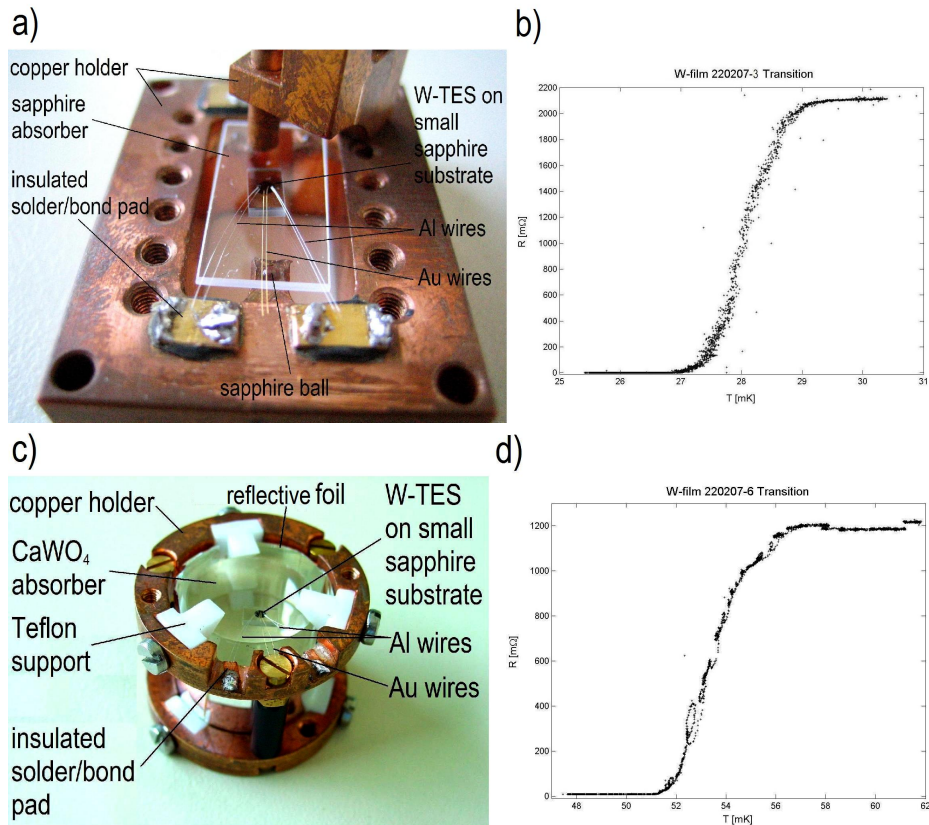


Figure 7.3: Composite "detector 1" and "detector 2" and the transitions of the used W-TEs. In figure a) the composite "detector 1" with a sapphire absorber of $10 \times 20 \times 1 \text{ mm}^3$ size and the W-TEs-3 is shown. The absorber is supported by sapphire balls in the copper holder. The electrical (bonded Al wires) and thermal (bonded Au wires) contacts of the TES can be seen. In figure b) the transition of the used W-TEs-3 is given. Figure c) shows the composite "detector 2" with a CaWO₄ crystal absorber of cylindrical shape with a diameter and a height of 20mm and the W-TEs-6. The crystal is fixed in the copper holder by teflon supports that thermally decouple it from the holder. A reflective foil is installed around the crystal to enable efficient scintillation light detection with a light detector. Electrical and thermal contacts of the TES to insulated solder/bond pads and the copper holder, respectively, are again provided by bonded Al and Au wires. In figure d) the transition of the used W-TEs-6 is shown.

7.2 Composite Detector 1

7.2.1 Measurements

For the measurements "detector 1" in the copper holder described above was mounted in a dilution refrigerator beneath the mixing chamber with the help of a thermally insulating Sintimid bar. A definite connection to the mixing chamber plate was established by a copper wire. The temperature resistor and the heater which are attached to the holder as well as the TES were connected to the controller electronics and to the SQUID read-out circuit, respectively. The detector was operated at the transition temperature of the TES of $\sim 28\text{mK}$.

To record an ^{55}Fe spectrum, an ^{55}Fe source equipped with an aperture with a $\sim 1\text{mm}$ hole was mounted $\sim 20\text{mm}$ below the detector (figure 7.4). This position of the source allowed irradiation of the absorber, however, almost no direct events due to the source have been observed in the small TES-substrate.

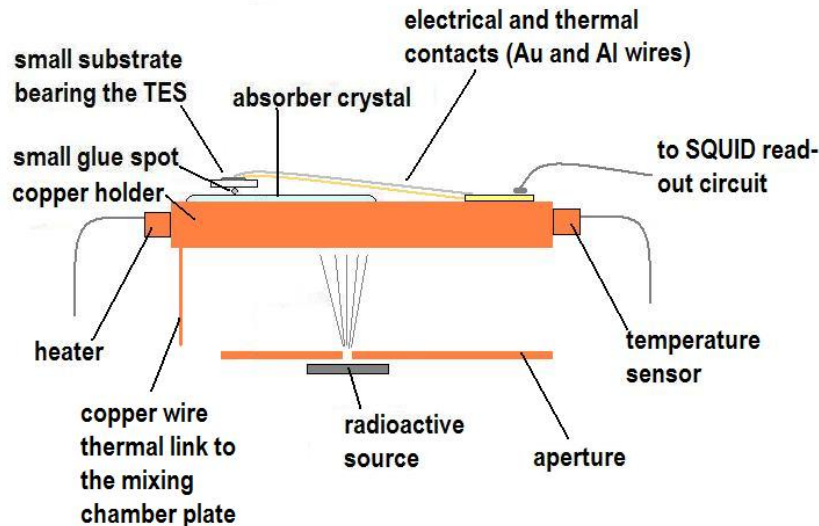


Figure 7.4: Sketch of the setup used to record a spectrum with an ^{55}Fe source with "detector 1". The distance between the source and the detector was $\sim 20\text{mm}$. The hole in the aperture has a diameter of $\sim 1\text{mm}$.

7.2.2 Results and Discussion

About 20000 pulses of the ^{55}Fe source were recorded during a measuring time of $\sim 2.6\text{h}$ using a data acquisition system (Fa. National Instruments, PXI Bus) with a time base of $2\mu\text{s}$. Further details concerning the pulse shape are given in section 8).

To analyse the measured spectrum a standard event fit was performed. Further details are given in [87, 88]. The spectrum is shown in figure 7.5. The separation of the Mn-K $_{\alpha}$ and Mn-K $_{\beta}$ peaks can clearly be seen.

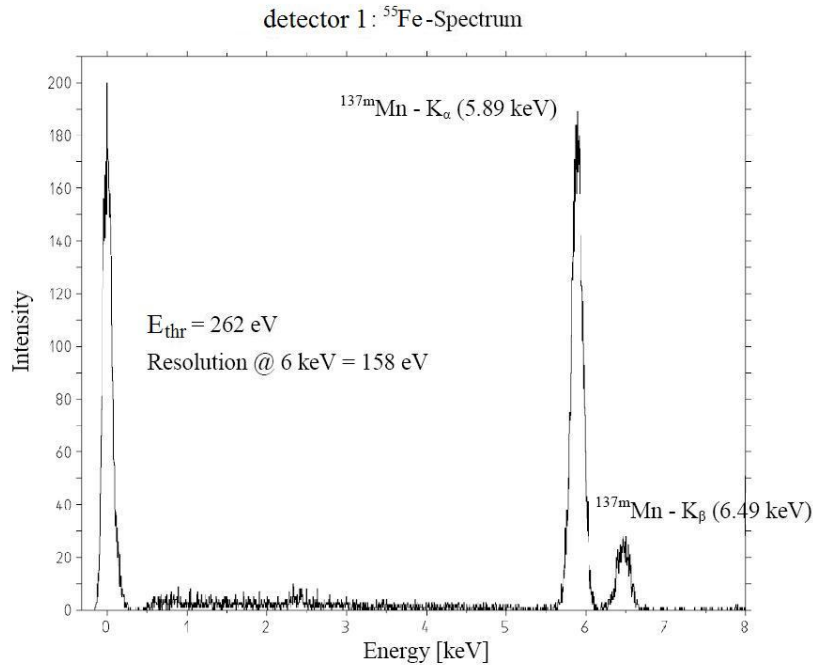


Figure 7.5: ^{55}Fe spectrum recorded with "detector 1". The separation of the Mn-K $_{\alpha}$ and Mn-K $_{\beta}$ lines can be clearly seen. An energy threshold E_{thr} of 262eV and a resolution (FWHM) of 158eV at 6keV were achieved.

A quite satisfying energy resolution (FWHM) of 158eV at 6 keV was achieved⁴. To derive the energy threshold noise samples of the baseline were recorded which lead to a peak at $\sim 0\text{keV}$ (see figure 7.5). The 5σ width of this peak determines the energy threshold [87, 88]. An energy threshold E_{thr} of 262eV was deduced.

7.3 Composite Detector 2

7.3.1 Measurements

Measurements with "detector 2" were carried out analogously to the measurements with "detector 1". The detector was operated at $\sim 53\text{mK}$, the transition temperature of the used TES.

⁴Compare, e.g., to a composite detector described in [39] where also an Al_2O_3 absorber of the same size was used. In [39], the obtained energy resolution is 187eV at 6 keV, however, the achieved energy threshold is $\sim 100\text{eV}$.

Spectra with a ^{137}Cs and a ^{57}Co source were recorded. These sources were mounted on the outside of the cyostat.

7.3.2 Results and Discussion

For the ^{137}Cs spectrum 200000 pulses were recorded in a measuring time of $\sim 3.6\text{h}$ using the same PXI Bus system, however, with a time base of $20\mu\text{s}$ to take into account the longer decay time of the pulses recorded with "detector 2" (for a presentation and discussion of the pulse shape see section 8). Details concerning the data analysis are given in [87, 88].

The spectrum is shown in figure 7.6. The sharp peak around 0keV includes noise samples for threshold determination, while the broad distribution around 200keV arises from muon induced events in the detector. The peak at 662keV arises from the ^{137}Cs source.

An energy threshold E_{thr} of 10keV could be deduced from the noise peak and an energy resolution (FWHM) of 32keV at 662keV (^{137}Cs line) was found.

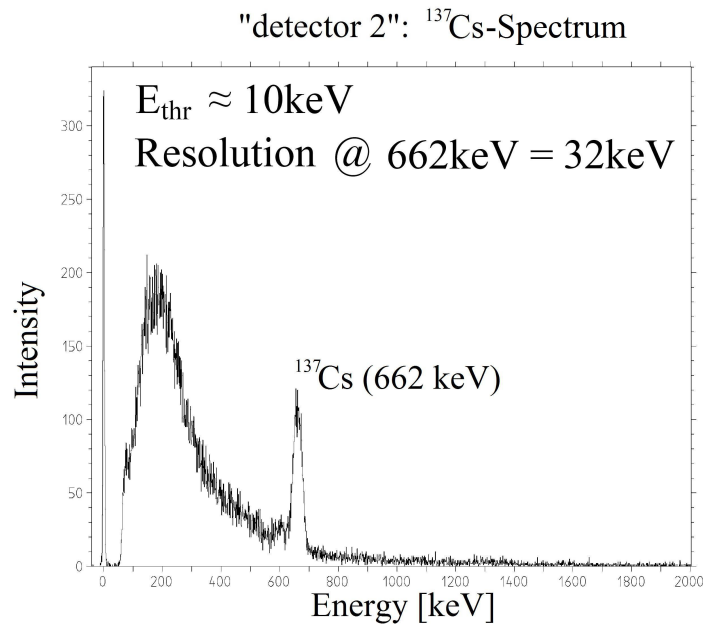


Figure 7.6: ^{137}Cs spectrum recorded with "detector 2". The sharp peak around 0keV includes noise samples, the broad distribution is due to muon induced events in the detector and the peak at 662keV corresponds to the ^{137}Cs line. An energy threshold E_{thr} of 10keV and a resolution (FWHM) of 32 keV at 662keV were achieved.

For the ^{57}Co spectrum 25830 pulses were recorded in a measuring time of $\sim 1.0\text{h}$, while the same measurement parameters were used and the same data analysis was performed as for the ^{137}Cs measurement. The obtained spectrum (in the range from 50keV to 160keV) is shown in figure 7.7. The two ^{57}Co peaks and the W- K_α escape peak can be seen.

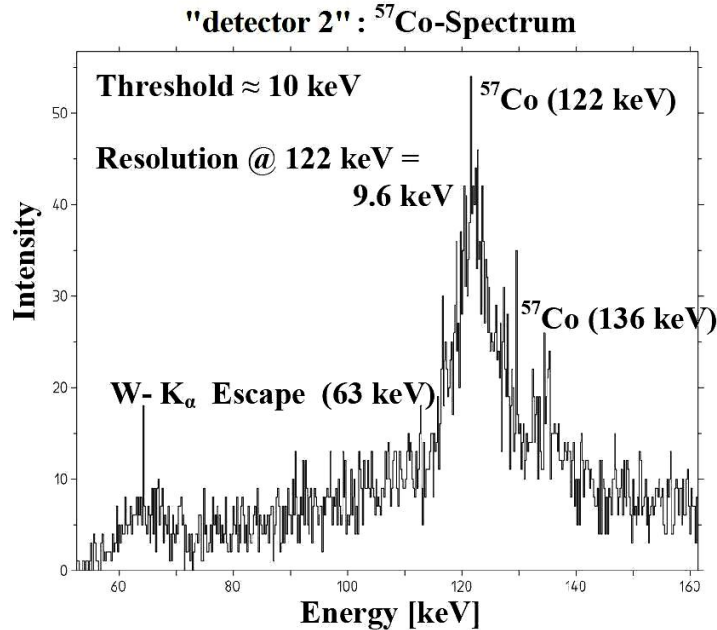


Figure 7.7: W- K_α escape peak and ^{57}Co lines recorded with "detector 2". A resolution (FWHM) of 9.6 keV at 122keV and of 7.6keV at 63keV were achieved.

From the ^{57}Co measurement an energy resolution (FWHM) of 9.6keV at 122keV (^{57}Co line) was found. For the W- K_α escape peak an energy resolution of 7.6keV at 63keV was deduced. For details concerning the data analysis see [87, 88].

The energy threshold and the energy resolutions found for "detector 2" were limited by microphonics and SQUID noise and can still be improved.

7.4 Conclusions

With these two composite detectors it could be successfully demonstrated that good energy thresholds and resolutions can be realised applying the composite detector design. Composite "detector 1" - with a relatively small absorber mass - shows highly satisfying results. The properties of composite "detector 2" show that the composite design, when applying the technique of a plain glue layer in combination with a big absorber, also exhibits a

promising potential.

To further exploit the composite design an improvement of the quality and reproducibility of the glueing techniques should be aimed at. Especially, the production of a plain glue layer concerning the thickness and homogeneity of the glue layer can surely be improved. Hence, further composite detectors with small glue spots as well as large glue layers, with different absorber sizes and with further improved TESs should be fabricated and investigated.

Chapter 8

Thermal Detector Model for Composite Detectors

The basic thermal detector model (BTDM) describes the properties of a cryogenic particle detector with a TES (Transition Edge Sensor) *directly* deposited on the surface of the absorber crystal and is discussed in greater detail in, e.g., [40], [39] and [41]. In order to discuss and understand the performance of the two composite detectors (measurements performed are presented in section 7.2 and 7.3) a thermal detector model including an extension concerning the composite design is presented in this chapter.

8.1 Basic Thermal Detector Model (BTDM)

The properties of a detector and the signal evolution are fundamentally affected by relaxation processes after the energy deposition in the absorber of the detector. Two main contributions to the TES temperature signal can be extracted [41]: a so-called non-thermal contribution, characterised by a fast decay time of the temperature signal, and a thermal contribution, characterised by a slow decay time of the temperature signal. The processes leading to these two different contributions are shortly depicted in the following sections.

8.1.1 Processes in the Absorber

Within a very short time of a few ps after an event in the absorber of the detector (here: the absorber is a dielectric material, like CaWO_4 or Al_2O_3) the energy is existent in optical phonons¹ [41]. These decay within a few 100ps into acoustic phonons (longitudinal - LA - and transversal -TA) with an approximately monochromatical frequency spectrum corresponding to $\sim\frac{1}{2}$

¹A small fraction of the energy is distributed to scintillation photons. In a sapphire absorber this contribution can be neglected, while in the CaWO_4 absorber these scintillation photons carry minimum $\sim 1\%$ of the deposited energy. This is the energy fraction measured with the scintillation light detector in the CRESST experiment [18].

of the Debye frequency (frequencies in the THz range²). Thereafter the LA phonons decay into TA phonons and spread via isotope scattering and scattering at impurities over the whole crystal. As the mean free path during this process reaches the dimensions of the absorber crystal these non-thermal phonons (frequencies in the THz range) are distributed ballistically over the whole crystal [41].

Additional energy loss occurs mainly in two ways: by inelastic scattering at the crystal surfaces leading to thermalisation in the absorber on a typical timescale of some ms, or by absorption and subsequent thermalisation in the metal film (the TES) which is deposited directly on the crystal surface on a typical timescale of a few hundred μs up to $\sim \text{ms}$ [41, 39]. Both processes cause signal contributions in the TES, the so-called thermal and non-thermal contributions.

8.1.2 Graphical Representation of the BTDM

Modelling of the individual detector components in terms of heat capacities, temperatures and couplings between the individual components, the detector performance and the pulse shape recorded via the TES can be explained quantitatively. Such a model for a cryogenic calorimeter is given in figure 8.1 (taken from [41]).

The absorber is assumed as a dielectric crystal and therefore its heat capacity is dominated by the contribution of the lattice while the electronic contribution can be neglected [39]. Concerning the TES, the lattice heat capacity contribution can be neglected due to the small size of the TES film and the low temperatures. The electronic contribution is dominant [39]. Hence, the thermal coupling of the absorber phononic system to the TES electronic system is given by G_{ea} , where $G_{ea} = (\frac{1}{G_K} + \frac{1}{G_{ep}})^{-1}$ [41]. G_K is the Kapitza-coupling (transmission of thermal phonons through interfaces) with $G_K \propto T^3$ and G_{ep} is the coupling between the electron and phonon system in the TES with $G_{ep} \propto T^5$ [41]. For very low temperatures, the strong temperature dependence of this coupling leads to an almost complete thermal decoupling of the TES electron system and the TES phonon system and therefore also between the TES electron system and the absorber phonon system [41]. For the detectors discussed in the present work, the thermal conductance G_{eb} , the coupling of the TES to the heat bath, is provided by two gold-bond wires connecting the TES to the copper holder. The thermal conductance G_{ab} , the coupling of the absorber to the heat bath, is given by the support of the absorber crystal in the copper holder. With the use of sapphire balls or Teflon parts and due to the strong temperature dependence of the coupling, G_{ab} can be made negligibly small at mK temperatures.

The power input $P_e(t)$ indicated in the picture is given by non-thermal phonons propagating into the TES. These thermalise in the electron sys-

²At mK temperatures thermal phonons exhibit frequencies in the GHz range.

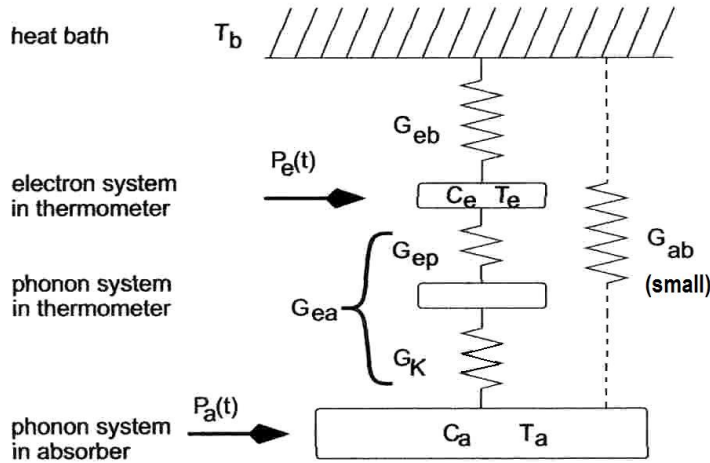


Figure 8.1: Thermal model of a cryogenic detector with a directly deposited TES (thermometer) [41]. T_b is the heat bath temperature, T_e and T_a are the temperatures of the TES electron system and the absorber phonon system, respectively, C_e and C_a are their heat capacities. Phonons that thermalise in the electron system of the TES or in the absorber cause the energy flows P_e or P_a into the TES and the absorber, respectively. G_{ab} , G_{eb} and G_{ea} are the thermal conductances.

tem of the TES and can then either escape via the thermal conductance G_{eb} into the heat bath or be transferred back to the absorber via the thermal conductance G_{ep} [41]. Due to the very small electron-phonon coupling G_{ep} at low temperatures, G_{eb} will be the dominant path for the phonons thermalised in the electron system of the TES. The application of electro-thermal feedback (ETF) can further increase the effective thermal conductance G_{eb} and therefore further decrease the fraction of thermalised phonons that are radiated back into the absorber [89, 41]. Due to the very small thermal conductance G_{ep} the contribution to the thermal phonon population in the absorber by non-thermal phonons thermalised in the TES can be neglected for very low temperatures [41]. As described in the previous section, non-thermal phonons in the absorber can thermalise on the absorber crystal surfaces and lead to a power input $P_a(t)$ (see figure 8.1) to the thermal phonon population in the crystal [41].

8.1.3 Non-thermal and Thermal Phonons and Pulse Shape

The life time $\tau_{t, \text{TES}}$ for the thermal phonons in the absorber, i.e., the time describing the propagation of thermal phonons from the absorber into the TES, is determined by the thermal conductances, that are valid for the transfer of the thermal phonons. $\tau_{t, \text{TES}}$ corresponds to the thermal relaxation time of

the absorber.

To determine the actual collection time of the non-thermal phonons in a TES directly deposited onto the absorber surface, i.e., the life time of the non-thermal phonons in the absorber $\tau_{\text{nt, TES}}$ two competing processes, reducing the non-thermal phonon population in the absorber, have to be taken into account: the thermalisation time in the TES (the metal film) τ_{film} and the thermalisation time in the crystal, τ_{crystal} . This correlation is given in the following equation [41]:

$$\tau_{\text{nt, TES}} = \left(\frac{1}{\tau_{\text{film}}} + \frac{1}{\tau_{\text{crystal}}} \right)^{-1} \quad (8.1)$$

For the calculation of τ_{film} a simple model can be used [41]:

$$\tau_{\text{film}} = \frac{2V_{\text{a}}}{A_{\text{TES}} \bar{\eta} \langle v_{g\perp} \alpha \rangle} \quad (8.2)$$

- τ_{film} : thermalisation time of non-thermal phonons in the TES
- τ_{crystal} : thermalisation time of non-thermal phonons in the absorber crystal
- V_{a} : volume of the absorber crystal
- A_{TES} : area of the TES
- $\bar{\eta}$: absorption probability for the non-thermal phonons in the TES
- $v_{g\perp}$: group velocity of the non-thermal phonons normal to the interface area (between absorber and TES)
- α : transmission probability of the non-thermal phonons
- $\langle \dots \rangle$: average over all modes and wave vectors of the incident phonons

Estimated calculated values for the material-specific parameters α , $\bar{\eta}$ and $\langle v_{g\perp} \alpha \rangle$ are given in [41] for Ir, Au and W on sapphire and on silicon.

However, if the surface to volume ratio for the absorber crystal is relatively small or if the TES area to absorber crystal surface ratio is relatively big³ then the thermalisation time in the crystal τ_{crystal} is significantly larger than the thermalisation time in the TES τ_{film} . In this case, $\tau_{\text{nt, TES}}$ is given by:

$$\tau_{\text{nt, TES}} \approx \tau_{\text{film}} = \frac{2V_{\text{a}}}{A_{\text{TES}} \bar{\eta} \langle v_{g\perp} \alpha \rangle} \quad (8.3)$$

The only significant signal in the TES would be due to phonons thermalising in the TES, the non-thermal contribution. The other extreme example for $\tau_{\text{nt, TES}}$ is given by the situation that no non-thermal phonons are collected and thermalised in the TES. Then $\tau_{\text{film}} \rightarrow \infty$ and then:

$$\tau_{\text{nt, TES}} \approx \tau_{\text{crystal}} \quad (8.4)$$

³The smaller the surface to volume ratio for the absorber and the larger the TES area to absorber surface ratio, the smaller the fraction on non-thermal phonons that thermalises on the crystal surface.

The only significant signal in the TES would be due to phonons thermalising in the absorber crystal, the thermal contribution.

Independent from these considerations, the deposition of the energy E in the TES can be described by two distributions [41]:

- non-thermal phonons relaxing in the TES give the power input

$$P_e(t) = \Theta(t)\epsilon\left(\frac{E}{\tau_{nt, TES}}\right)e^{-\frac{t}{\tau_{nt, TES}}}$$

- thermal phonons relaxing in the absorber give the power input

$$P_a(t) = \Theta(t)(1 - \epsilon)\left(\frac{E}{\tau_{nt, TES}}\right)e^{-\frac{t}{\tau_{nt, TES}}}$$

where $\Theta(t)$ is the step function and ϵ is the fraction of non-thermal phonons absorbed in the TES. The assumption is made that the energy is instantaneously existent in the form of non-thermal phonons in the absorber crystal. This assumption leads to two coupled differential equations with the solution giving the pulse shape (rise in temperature) $\Delta T(t)$ [41]:

$$\Delta T(t) = \Theta(t) \left[A_{nt} \left(e^{-\frac{t}{\tau_{nt, TES}}} - e^{-\frac{t}{\tau_{in, TES}}} \right) + A_t \left(e^{-\frac{t}{\tau_t, TES}} - e^{-\frac{t}{\tau_{nt, TES}}} \right) \right] \quad (8.5)$$

where A_{nt} and A_t are the amplitudes of the two partial pulses. The different time constants can be interpreted as follows ([41]):

- $\tau_{nt, TES}$: life time of non-thermal phonons in the absorber, results in a fast decay time of the pulse and the rise time of the thermal phonon pulse
- $\tau_{in, TES}$: intrinsic time constant of the TES, gives the rise time of the non-thermal phonon pulse, here: $\tau_{in, TES} \ll \tau_{nt, TES}$. The detectors work in bolometric mode [41].
- τ_t, TES : life time of thermal phonons in the absorber, results in a slow decay time of the pulse

The different time constants are calculated with the following equations (for a detailed derivation see [41]):

$$\tau_{nt, TES} = \left(\frac{1}{\tau_{film}} + \frac{1}{\tau_{crystal}} \right)^{-1} = \left(\left(\frac{2V_a}{A_{TES}\bar{\eta}\langle v_{g\perp}\alpha \rangle} \right)^{-1} + \tau_{crystal}^{-1} \right)^{-1} \quad (8.6)$$

$$\tau_{in, TES} \approx \frac{C_e}{G_{ea} + G_{eb}} \quad (C_e \ll C_a) \quad (8.7)$$

$$\tau_t, TES \approx \frac{C_a}{\frac{G_{eb}G_{ea}}{G_{eb}+G_{ea}} + G_{ab}} \quad (C_e \ll C_a) \quad (8.8)$$

In figure 8.2 an example for a fit of the pulse shape observed in the TES of a cryogenic detector according to equation 8.5 is shown. The black line gives the temperature signal in the TES (equation 8.5). As can be seen from

this figure a physical pulse is characterised by a fast rise time and a slower (compared to the rise time) decay time. Two signals, the non-thermal (red line) and the thermal (blue line), contribute to the observed temperature signal in the TES (black line). The non-thermal contribution is described by the rise time $\tau_{in, TES}$ and the decay time $\tau_{nt, TES}$. The thermal contribution is described by the rise time $\tau_{nt, TES}$ and the decay time $\tau_{t, TES}$. For detectors considered in this work, $\tau_{in, TES} \ll \tau_{nt, TES}$, as ETF was used [89]. Thus, in good approximation the resulting signal in the TES (black line) can be described by one rise time ($\approx \tau_{in, TES}$) and by two decay times ($\tau_{nt, TES}$ and $\tau_{t, TES}$).

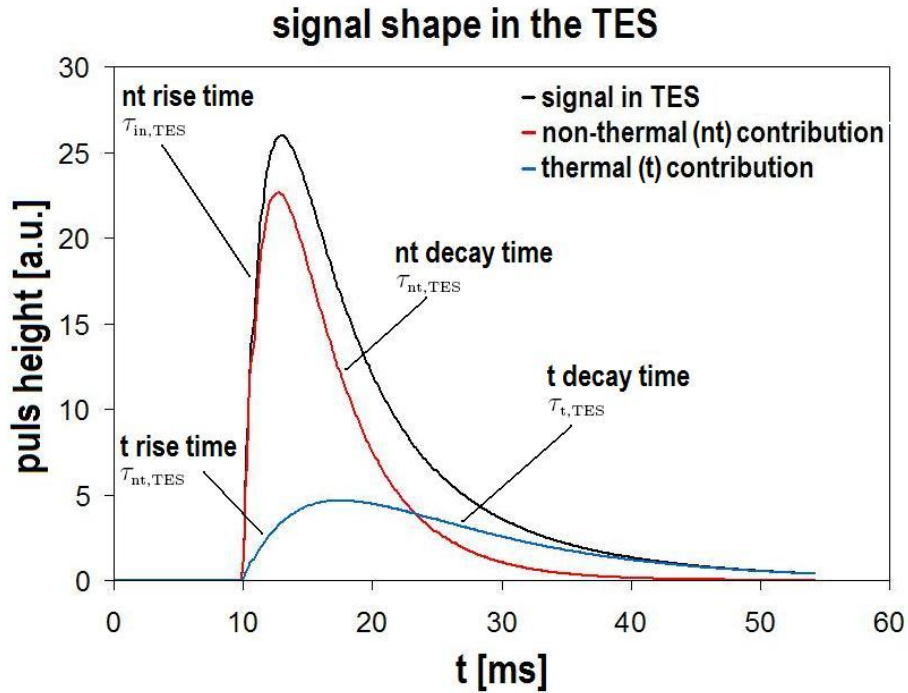


Figure 8.2: Typical signal shape observed in the TES of a cryogenic detector. The black line gives the total signal shape. The red line represents the contribution by non-thermal phonons, while the blue line gives the signal contribution due to thermal phonons.

This model gives a description of the performance of a cryogenic calorimeter with a TES directly deposited onto the absorber crystal.

8.2 Properties of the Investigated Composite Detectors

Three different composite detectors ("detector 1, 2 and 3") have been investigated.

8.2.1 Setup of the Three Composite Detectors

”Detector 1” and ”detector 2” are the two composite detectors already described in section 7.1.3, while ”detector 3” is described in greater detail in [87]. As absorber the same cylindric CaWO_4 absorber was used as for ”detector 2”⁴. For ”detector 3” a small silicon substrate with an Ir/Au-TES (produced in the same way as the ”small” W-TEs, see chapter 6) is glued onto the absorber with a small glue spot. The detector is contacted and supported in a copper holder in the same way as ”detector 2”.

In table 8.1 the main properties of these three composite detectors are given, where mat-a is the absorber material, V_a is the absorber volume, A_g is the area of the applied glue layer (or spot) used for the attachment of the TES-substrate, d_g is the estimated thickness of the applied glue layer (or spot) and R_{ag} is the (absorber-volume to glue-volume)-ratio. Only an estimate can be given for this ratio, as also the thickness of the glue layer (or glue spot) are not well known.

detector	mat-a	V_a [mm ³]	A_g [mm ²]	d_g [mm]	R_{ag}
”1”	Al_2O_3	$10 \cdot 20 \cdot 1 = 200$	$0.35^2 \cdot \pi = 0.38$	~ 0.2	~ 2600
”2”	CaWO_4	$10^2 \cdot 20 \cdot \pi = 6280$	$3 \cdot 5 = 15$	~ 0.3	~ 1400
”3”	CaWO_4	$10^2 \cdot 20 \cdot \pi = 6280$	$0.5^2 \cdot \pi = 0.79$	~ 0.2	~ 43000

Table 8.1: Main properties of the three investigated composite detectors. The absorber material is given in the second column. V_a denotes the absorber volume, A_g gives an estimated value for the glue area and d_g an estimate for the thickness of the glue layer. R_{ag} is the estimated absorber-volume to glue-volume ratio.

8.2.2 The ”TES-substrate - TES” system

As already depicted in section 7.1.3, for ”detector 1” and ”detector 2” the ”small” W-TEs described in chapter 6 on sapphire substrates are used, while for ”detector 3” a circular Ir/Au-TES, evaporated onto a small silicon substrate is employed. To further characterise these systems, they are regarded as individual cryogenic detectors that can be described with the basic thermal detector model given in section 8.1. Thus, the TES-substrate is considered as an ”absorber” with the TES deposited directly onto the ”absorber” surface. Therefore the signal function due to a temperature change of the ”TES-detector” is given by (see equation 8.5):

$$\begin{aligned}
 f_{\text{TES-detector}}(t) &= \Theta(t) \cdot [f_{\text{TES-detector,nt}} + f_{\text{TES-detector,t}}] = \\
 &= \Theta(t) \left[A_{nt} \left(e^{-\frac{t}{\tau_{nt,s-\text{TES}}}} - e^{-\frac{t}{\tau_{in,s-\text{TES}}}} \right) + A_t \left(e^{-\frac{t}{\tau_{t,s-\text{TES}}}} - e^{-\frac{t}{\tau_{nt,s-\text{TES}}}} \right) \right]
 \end{aligned} \tag{8.9}$$

⁴”Detector 2” was built after disassembling of ”detector 3”.

where $\tau_{\text{nt,s-TES}}$ and $\tau_{\text{t,s-TES}}$ give the non-thermal phonon and the thermal phonon life times in the TES-substrate, respectively, and $\tau_{\text{in,s-TES}}$ is the rise time of the signal in the TES.

Using equation 8.3 an estimate for an upper limit of the life time $\tau_{\text{nt,s-TES}}$ for non-thermal phonons in the TES-substrate thermalising in the TES can be calculated with the assumption of an instantaneously present non-thermal phonon population in the TES-substrate:

$$\tau_{\text{nt,s-TES}} \leq \frac{2V_s}{A_{\text{TES}}\bar{\eta}\langle v_{g\perp}\alpha \rangle} \quad (8.10)$$

V_s denotes the TES-substrate volume, A_{TES} is the TES area. The material specific parameters $\bar{\eta}$ and $\langle v_{g\perp}\alpha \rangle$ are taken from [41].

In table 8.2 the TES-substrate material (mat-TES-s), the TES material (mat-TES), the TES-substrate volume V_s , the TES area A_{TES} , and the calculated upper limit for the life time of non-thermal phonons in the TES-substrate thermalising in the TES are summarised for the three investigated detectors.

detector	mat-TES-s	mat-TES	V_s [mm ³]	A_{TES} [mm ²]	$\tau_{\text{nt,s-TES}}$ [ms]
"1"	Al ₂ O ₃	W	3.5·1=15	1 ² · π = π	≤0.013
"2"	Al ₂ O ₃	W	3.5·1=15	1 ² · π = π	≤0.013
"3"	Si	Ir/Au	3.5·0.5=7.5	1 ² · π = π	≤0.014

Table 8.2: Properties of the (TES-substrate - TES) system of the three composite detectors. Columns two and three list the materials used for the substrates and TESs, respectively. V_s is the TES-substrate volume, A_{TES} is the TES area and $\tau_{\text{nt-sTES}}$ is the calculated upper limit for the collection time of the non-thermal phonons from the TES-substrate into the TES.

As the material (Al₂O₃) of the TES-substrate of "detector 1" and "detector 2" is a dielectric and the material of the TES-substrate of "detector 3" is a semiconductor (Si), for all three detectors the electron system of the TES-substrate is neglected in the following as its contribution to the heat capacity is negligible in comparison to the heat capacity of the phonon system [39]. Hence, in the following discussion the "TES-detectors" of the three composite detectors are treated as equal systems as their performance is very similar to each other as discussed above.

8.2.3 Signal Shape Observed for the Investigated Composite Detectors

With these three detectors spectra of different radioactive sources were recorded (see chapter 7). From these measurements for each detector an averaged standard pulse was extracted. This pulse was then fitted with a function of

the form given in equation 8.5. For the three composite detectors $\tau_{\text{in, TES}} \ll \tau_{\text{nt, TES}}, \tau_{\text{t, TES}}$ and therefore $\tau_{\text{in, TES}} \approx \tau_{\text{rise}}$. The results for the specific rise and decay times of the signal pulse for the three composite detectors are summarised in table 8.3.

detector	τ_{rise} [ms]	τ_{decay1} [ms]	τ_{decay2} [ms]
"1"	0.31	2.00	-
"2"	1.58	4.94	11.6
"3"	0.09	(0.50)	22.9

Table 8.3: Rise and decay times of the fitted standard event for the three detectors. For "detector 1" only one decay time was found. For "detector 3" only the slow decay time τ_{decay2} is included in the discussion as the fast decay time τ_{decay1} can be attributed to a process not connected to the absorber crystal of the composite detector (see discussion below).

As can be seen from table 8.3, for "detector 1" only one decay time was found. For "detector 2" two decay times could be identified. The fast decay time τ_{decay1} found for "detector 3" is assumed not to originate from a phonon signal of the absorber. This assumption is justified when estimating the non-thermal collection time in a cryogenic detector with a CaWO_4 crystal⁵ of the size used here in combination with a TES of the size of the applied glue area, which amounts to $\sim 63\text{ms}$ (without electro-thermal feedback (ETF), see equation 8.2). This time is ~ 130 times larger⁶ than the observed τ_{decay1} . Thus, with this value and equation 8.1 a non-thermal phonon life time of $\sim 0.5\text{ms}$ would yield a thermalisation time of non-thermal phonons in the crystal of $\sim 0.5\text{ms}$. However, such a tiny thermalisation time in the crystal is only expected for rough surfaces or large defect densities in the crystal. In addition, as the same crystal was used for "detector 2", this time would also be expected to occur for "detector 2". Hence, this fast decay time is most probably related to the collection of scintillation light in the silicon TES-substrate [87] used for "detector 3". Hence, for the following discussion only the slower decay time τ_{decay2} is regarded for "detector 3".

8.3 Thermal Detector Model for a Composite Detector (TDM-CD)

To describe the signals observed with composite detectors additional components have to be included into the basic thermal detector model: the glue and the TES-substrate. Such an extended model is presented in figure 8.3.

⁵The material specific parameters for the CaWO_4 crystal in combination with an Ir/Au-TES are taken from [90].

⁶With the application of ETF this time can be smaller, however, the ETF is not assumed to account for a factor of ~ 130 .

8.3.1 Processes in the Absorber

The fundamental interaction of a particle or radiation in the absorber is not affected by the glue. The phonon generation, decay and distribution in the absorber crystal occur in the same way as in a detector with a TES which is directly deposited onto the absorber crystal surface (see section 8.1). However, concerning the non-thermal and thermal phonon propagation from the absorber into the TES, the glue as well as the TES-substrate have to be taken into account.

8.3.2 Graphical Representation of the TDM-CD

As shown in figure 8.3, the glue and the TES-substrate are included as additional components with heat capacities C_g and C_s and temperatures T_g and T_s , respectively. As the glue is considered as a dielectric⁷ only the phonon system is taken into account for this component. The same holds true for the TES-substrates as described in section 8.2.2. Additionally, the energy flows P_g and P_s are indicated corresponding to non-thermal phonons which thermalise in the glue and in the substrate, respectively. The interfaces between the absorber and the glue, between the glue and the TES-substrate and between the TES-substrate and the TES are again considered to be given as Kapitza couplings G_{Kag} , G_{Kgs} and G_{Ksp} , respectively, for the thermal phonons. Alternatively, the glue can be included into the system only through its thermal conductance, resulting in the combined thermal conductance G_{Kas} between the absorber and the substrate which is also assumed to be given as a Kapitza coupling. The direct coupling of the absorber to the heat bath G_{ab} is considered to be quite weak, as already described for the basic thermal detector model (see section 8.1).

8.3.3 Propagation of Non-Thermal and Thermal Phonons

The processes considered can be described as propagations of non-thermal and thermal phonons. The initial situation is that after an event in the absorber a non-thermal phonon population exists and a thermal phonon population is formed from part of the non-thermal phonon population. In general, these populations are collected via the glue layer (where the non-thermal phonons possibly can also thermalise) and then reach the TES-substrate (compare to [40]).

Figure 8.4 gives a rough overview of the propagation processes that are possible in such a complex system for the non-thermal and thermal phonons.

⁷For the glue a specific conductivity of $\geq 2 \cdot 10^{12} \Omega \text{cm}$ at room temperature is given from the manufacturer.

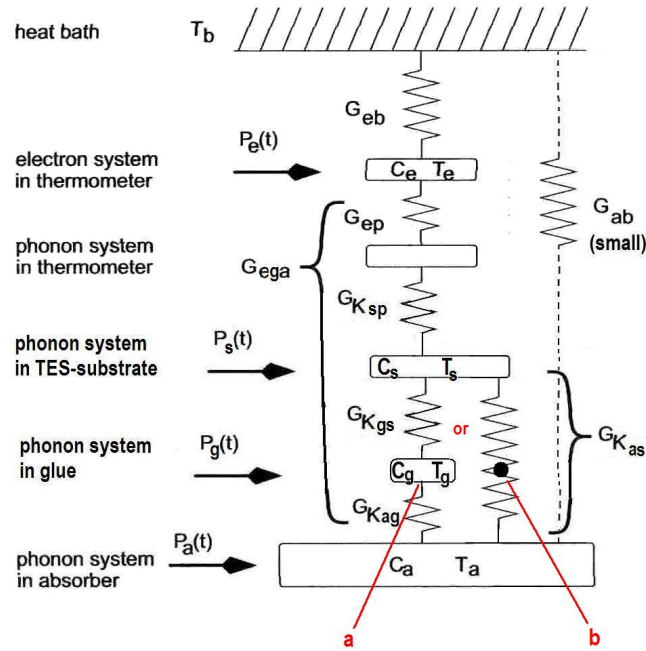


Figure 8.3: Thermal model of a composite detector. For the glue two alternative representations *a* and *b* are presented. Alternative *a* shows the glue as thermal component to which a heat capacity C_g and a temperature T_g can be related. Alternative *b* shows the glue representing a thermal conductance G_{Kas} between the absorber and the TES-substrate. T_b , T_e , T_a , T_s and T_g are the temperatures of the heat bath, the thermometer (TES) electron system, the absorber phonon system, the TES-substrate phonon system and the glue phonon system, respectively. C_e , C_a , C_s and C_g are their heat capacities, and P_e , P_a , P_s and P_g are the energy flows into the particular system caused by non-thermal phonons thermalising in the respective component. G_{ab} , G_{eb} and G_{ega} are the thermal conductances.

Also the decay of non-thermal phonons into thermal phonons is indicated in figure 8.4. For the thermal phonons only the propagation direction versus the heat bath is given, while of course also the other propagation direction is possible. However, the coupling G_{ep} is again considered to be very small in comparison to the coupling G_{eb} . Therefore, non-thermal and thermal phonons that reach the TES electron system are effectively removed from the system. The shaded red (blue) areas indicate a non-thermal (thermal) phonon population. The green arrows depict the decay of non-thermal phonons into thermal phonons. The red arrows give the non-thermal phonon flows that correspond to the power inputs $P(t)$ indicated in figure 8.3. The glue is illustrated in two different ways: as thermal component, where non-thermal phonons can decay, or simply as thermal conductance (see also representation *a* and *b* in figure 8.3).

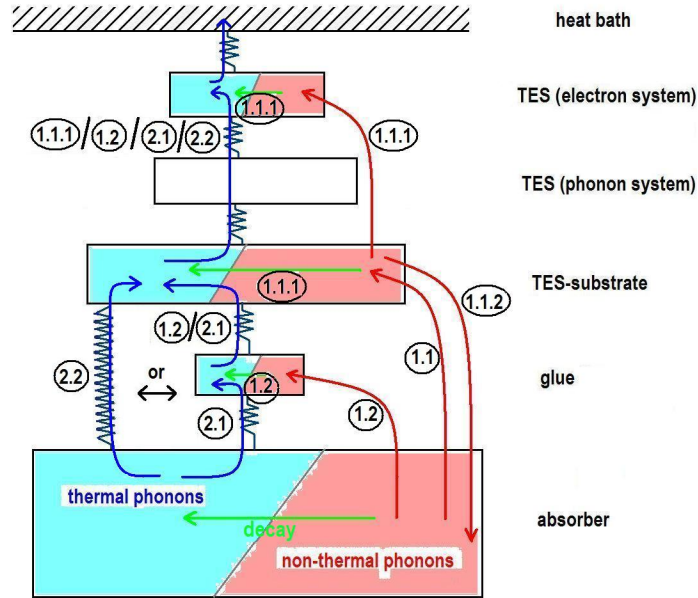


Figure 8.4: Sketch of the most important propagation possibilities for non-thermal (red arrows) and thermal phonons (blue arrows). The green arrows depict the decay of non-thermal into thermal phonons. For the thermal phonons only the propagation towards the heat bath is given. The influence of the glue is characterised in two ways: the glue can either be considered as a thermal component with a heat capacity and a temperature where non-thermal phonons can decay or the glue can contribute a thermal conductance to the system (see *a* and *b* in figure 8.3). The numbers given correspond to the different phonon propagations discussed below.

As already depicted in section 8.2.2, the system consisting of the TES-substrate, the TES and the coupling to the heat bath can be treated as an "individual" cryogenic detector (the "TES-detector"). It can be described with the basic thermal detector model presented in section 8.1. However, in the thermal detector model the signal evolution is described under the assumption of a non-thermal phonon population that is instantaneously present in the absorber and a thermal phonon population evolving from the non-thermal one. For the composite detectors discussed here, these assumptions do no longer hold for the "TES-detector" as the non-thermal phonon population is not initially present in the TES-substrate (the absorber of the "TES-detector") but is now delivered from the main absorber through the interfaces (absorber - glue - TES-substrate). This "transfer"-process causes a time-dependent power-flow, $P(t)$, into the TES-substrate that can include thermal and non-thermal phonon contributions. Hence, the resulting signal in the TES has to be described by a convolution of the power input $P(t)$ and

the "TES-detector"-signal $f_{\text{TES-detector}}(t)$ (see equation 8.9):

$$\Delta T(t) = (P * f_{\text{TES-detector}})(t) \quad (8.11)$$

For the discussion two main cases are considered independently from each other: **case 1**, the propagation of initially non-thermal phonons from the absorber into the remaining system and **case 2**, the propagation of "initially" thermal phonons from the absorber into the remaining system. The possible contributions to the temperature signal in the TES are discussed.

The two different phonon populations in the absorber deliver two power flows $P_{nt}(t)$ and $P_t(t)$ into the remaining system:

$$P_{nt} \propto \Theta(t) e^{-\frac{t}{\tau_{nt,a}}} \quad (8.12)$$

$$P_t \propto \Theta(t) \left[e^{-\frac{t}{\tau_{t,a}}} - e^{-\frac{t}{\tau_{nt,a}}} \right] \quad (8.13)$$

where the rise time of the non-thermal phonon power $P_{nt}(t)$ is considered to be infinitely fast on the time scale of the detector and is therefore neglected. The decay time of the non-thermal power pulse is given by the life time of the non-thermal phonons in the absorber (either decay into thermal phonons or be collected into the glue) $\tau_{nt,a}$. The thermal phonon power $P_t(t)$ is given by a pulse with a decay time $\tau_{t,a}$ corresponding to the life time for thermal phonons in the absorber (propagation into the remaining detector system or directly into the heat bath) and a rise time $\tau_{nt,a}$.

Case 1: non-thermal phonons from the absorber

Considering the propagation of non-thermal phonons from the absorber after crossing the interface (absorber - glue) there are two possibilities:

- **case 1.1:** the non-thermal phonons are further transferred into the TES-substrate (path 1.1 in figure 8.4) from which they either directly propagate into the TES and thereafter into the heat bath or decay into thermal phonons and propagate into the TES and thereafter into the heat bath (paths 1.1.1 in figure 8.4) or they propagate back through the glue into the absorber (path 1.1.2 in figure 8.4)
- **case 1.2:** the non-thermal phonons decay in the glue into thermal phonons; these propagate further into the TES-substrate from which they directly propagate into the TES and thereafter into the heat bath (path 1.2 in figure 8.4)

Case 2: thermal phonons from the absorber

Considering the propagation of thermal phonons from the absorber also two possibilities arise:

- **case 2.1:** the thermal phonons are transferred into the glue (which in this case is interpreted as thermal component, a in figure 8.3) and then into the TES-substrate from which they further propagate into the TES and thereafter into the heat bath (path 2.1 in figure 8.4)
- **case 2.2:** the thermal phonons are directly transferred via the thermal conductance (including the glue, b in figure 8.3) into the TES-substrate from which they further propagate into the TES and thereafter into the heat bath (path 2.2 in figure 8.4)

In the following these two cases are described in more detail.

8.3.4 Case 1: Non-thermal Phonons from the Absorber

In case 1 the (absorber - glue) interface is considered transparent for non-thermal phonons from the absorber leading (see figure 8.4) to a power input $P_{nt,as}(t)$ (path 1.1) into the TES-substrate or $P_{nt,ag}(t)$ (path 1.2) into the glue (where they thermalise).

Case 1.1

In case 1.1, it is assumed that thermal phonons from the absorber cannot cross the interface (absorber - glue), i.e., the thermal conductance G_{Kag} (see figure 8.3) is considered to be even much smaller than the thermal coupling of the absorber to the heat bath G_{ab} (see figure 8.3) given by the absorber crystal support in the copper holder. Thus in case 1.1, the TES-substrate and the TES are considered to be thermally decoupled from the absorber.

The non-thermal phonons lead to a power input $P_{nt,as}(t)$ into the TES-substrate (path 1.1). It is assumed that the transmission of the non-thermal phonons through the interfaces (absorber - glue - TES-substrate) can be described in analogy to equation 8.1 used for the non-thermal phonon life time in the BTDM. This collection time $\tau_{nt,as}$ for non-thermal phonons from the absorber through the glue into the TES-substrate is determined by a transmission parameter λ_{ags} describing the transmission through the interfaces (absorber - glue - TES-substrate), the absorber volume V_a , the glue area A_g and the thermalisation time $\tau_{crystal}$ of non-thermal phonons in the absorber crystal:

$$\begin{aligned} \tau_{nt,as} &= \left(\frac{1}{\tau_{coll-glue}} + \frac{1}{\tau_{crystal}} \right)^{-1} \\ \frac{1}{\tau_{nt,as}} &= \frac{A_g \overline{\eta_{as}} \lambda_{ags}}{2V_a} + \frac{1}{\tau_{crystal}} \end{aligned} \quad (8.14)$$

where $\tau_{coll-glue}$ is the collection time for non-thermal phonons in the glue area and $\overline{\eta_{as}}$ gives the probability for the non-thermal phonons not to be scattered

back from the TES-substrate into the absorber (path 1.1.2), but to reach the TES (path 1.1.1). λ_{ags} corresponds to $\bar{\eta} \langle v_{g\perp} \alpha \rangle$ of the BTDM, however, it now represents the material-specific parameters of the interface (absorber - glue - TES-substrate). Hence, the value of $\bar{\eta}_{\text{as}}$ controls the fraction of non-thermal phonons that propagate along path 1.1.1 or path 1.1.2.

For path 1.1.1 non-thermal phonons are regarded that reach the TES-substrate ($P_{nt,as}(t)$, see equation 8.12) where they can either further propagate into the TES and thereafter into the heat bath or decay into thermal phonons and then propagate into the TES and thereafter into the heat bath. This propagation and decay of the non-thermal phonons in the TES-substrate is described by the "TES-detector" function $f_{\text{TES-detector}}(t)$ (see equation 8.9). The resulting signal in the TES is therefore given by the convolution of the power input $P_{nt,as}(t)$ with the "TES-detector function" $f_{\text{TES-detector}}(t)$:

$$\begin{aligned}
 \Delta T(t) &\propto (P_{nt,as} * f_{\text{TES-detector}})(t) = \\
 &= P_0 \Theta(t) \left[-c_1 e^{-\frac{t}{\tau_{nt,as}}} e^{-t^b \left(\frac{1}{\tau_{nt,s-\text{TES}}} - \frac{1}{\tau_{nt,as}} \right)} + c_2 e^{-\frac{t}{\tau_{nt,as}}} e^{-t^b \left(\frac{t}{\tau_{in,s-\text{TES}}} - \frac{1}{\tau_{nt,as}} \right)} - \right. \\
 &\quad \left. - c_3 e^{-\frac{t}{\tau_{nt,as}}} e^{-t^b \left(\frac{t}{\tau_{t,s-\text{TES}}} - \frac{1}{\tau_{nt,as}} \right)} \right]_0^t = \\
 &= P_0 \Theta(t) \left[c_1 \left(e^{-\frac{t}{\tau_{nt,as}}} - e^{-\frac{t}{\tau_{nt,s-\text{TES}}}} \right) - c_2 \left(e^{-\frac{t}{\tau_{nt,as}}} - e^{-\frac{t}{\tau_{in,s-\text{TES}}}} \right) + \right. \\
 &\quad \left. + c_3 \left(e^{-\frac{t}{\tau_{nt,as}}} - e^{-\frac{t}{\tau_{t,s-\text{TES}}}} \right) \right] \tag{8.15}
 \end{aligned}$$

with the amplitudes:

$$c_1 = (A_{nt} - A_t) \frac{\tau_{nt,s-\text{TES}} \cdot \tau_{nt,as}}{\tau_{nt,as} - \tau_{nt,s-\text{TES}}} \tag{8.16}$$

$$c_2 = A_{nt} \frac{\tau_{in,s-\text{TES}} \cdot \tau_{nt,as}}{\tau_{nt,as} - \tau_{in,s-\text{TES}}} \tag{8.17}$$

$$c_3 = A_t \frac{\tau_{t,s-\text{TES}} \cdot \tau_{nt,as}}{\tau_{nt,as} - \tau_{t,s-\text{TES}}} \tag{8.18}$$

The first two terms of the signal function 8.15 describe contributions to the pulse with the same decay time $\tau_{nt,as}$ and the (shorter) rise times $\tau_{nt,s-\text{TES}}$ and $\tau_{in,s-\text{TES}}$, respectively. With $\tau_{in,s-\text{TES}}$ being very small in comparison to all other regarded times, the second term in equation 8.15 can be neglected. Concerning the third term two possibilities arise, resulting either in a second decay time $\tau_{t,s-\text{TES}}$ and therefore two different decay times ($\tau_{nt,as}$ and $\tau_{t,s-\text{TES}}$) of the signal function 8.15 or in the same decay time $\tau_{nt,as}$ and therefore altogether in one decay time ($\tau_{nt,as}$) of the signal function 8.15:

- $\tau_{nt,as} < \tau_{t,s-\text{TES}} \Rightarrow$ 2 decay times of the signal function: $\tau_{nt,as}$ and $\tau_{t,s-\text{TES}}$
- $\tau_{nt,as} > \tau_{t,s-\text{TES}} \Rightarrow$ 1 decay time of the signal function: $\tau_{nt,as}$

To decide which case is true for each of the three composite detectors ("detector 1", "detector 2" and "detector 3"), the observed decay times of these detectors (see section 8.2.3, table 8.3) are regarded:

- "detector 1":
If a non-thermal phonon power flow leads to a significant signal contribution in the TES then $\tau_{nt,as} > \tau_{t,s- TES}$ has to be true for "detector 1", as only one decay time is observed.
- "detector 3":
If a non-thermal phonon power flow leads to a significant signal contribution in the TES then $\tau_{nt,as} > \tau_{t,s- TES}$ has to be true for "detector 3", as only one decay time is observed.
- "detector 2":
If a non-thermal phonon power flow leads to a significant signal contribution in the TES then $\tau_{nt,as} < \tau_{t,s- TES}$ could be true for "detector 2" as two decay times are observed (see table 8.3).
Then it could be deduced that
 $\tau_{nt,as}$ corresponds to the faster decay time $\tau_{decay1} \approx 5\text{ms}$ and
 $\tau_{t,s- TES}$ corresponds to the slower decay time $\tau_{decay1} \approx 12\text{ms}$.
 The decay time $\tau_{t,s- TES}$ should be the same for all detectors as this decay time is related to the "TES-detector" which can be assumed to be equal for all detectors (section 8.2.2).
 Thus, if $\tau_{t,s- TES} \approx 12\text{ms}$ then $\tau_{nt,as} < \tau_{t,s- TES}$ should also be true for "detector 1", as here $\tau_{nt,as} \approx 2\text{ms}$. As no second decay time of $\sim 12\text{ms}$ is observed for "detector 1" this leads to a contradiction.
 Therefore, $\tau_{nt,as} > \tau_{t,s- TES}$ also has to be true for "detector 2" and one of the two observed decay times can be explained with a contribution by a non-thermal power flow from the absorber.

For path 1.1.2 the fraction $(1-\overline{\eta_{as}})$ of the non-thermal phonons is regarded that "escape" the collection in the TES by "choosing" path 1.1.2 back into the absorber. In the absorber the non-thermal phonons can either propagate into the TES-substrate again (case 1) or thermalise (case 2). Hence, the propagation possibility of path 1.1.2 does not contribute to the signal function in the TES a second decay time but causes a decrease in amplitude of the non-thermal phonon signal contribution (path 1.1.1) and an increase in the thermal phonon population in the absorber (see section 8.3.5).

These results indicate that for the three composite detectors $\tau_{nt,as} > \tau_{t,s- TES}$ can be assumed to hold true if the non-thermal phonon propagation along path 1.1.1 delivers one decay time to the observed signal in the TES of the detectors. In this case, the thermal decay time for the "TES-detector" $\tau_{t,s- TES}$ can be neglected as it does not influence the resulting signal in the TES⁸.

⁸This circumstance can also be motivated by the very fast non-thermal phonon collection time in the TES-substrate, that is due to the quite large (TES-substrate-volume to TES-area)-ratio. This delivers an efficient collection of the non-thermal phonons in the TES, before they can thermalise.

Then for all three composite detectors one observed decay time could be attributed to the non-thermal phonon power flow $P_{nt,as}(t)$, but for "detector 2" the second observed decay time has to be explained by another process, either by a non-thermal phonon propagation into the glue, where the non-thermal phonons thermalise (case 1.2, path 1.2, discussed next) or by a contribution from thermal phonons from the absorber (case 2, path 2.1 or 2.2, see section 8.3.5).

Case 1.2

In case 1.2, it is assumed that non-thermal phonons can cross the interface (absorber - glue) into the glue with the life time $\tau_{nt,ag}$, where they thermalise within the time τ_{glue} (which has to be compared to the thermalisation time $\tau_{crystal}$ in section 8.1.3). Hence, to allow these thermal phonons to propagate further into the TES-substrate, the interfaces (absorber - glue) and (glue - TES-substrate) which are considered to be equal, have to be "transparent" for thermal phonons, i.e., $G_{Kgs} \approx G_{Kga} \neq 0$. Therefore, if phonons propagating along path 1.2 contribute to the temperature signal in the TES, also phonons propagating along the paths 2.1 and 2.2 can lead to signal contributions in the TES.

However, at this point, only the possible signal contributions by phonons propagating along path 1.2 are discussed.

The non-thermal phonons lead to a power input $P_{nt,ag}(t)$ (see equation 8.12) into the glue (path 1.2). It is assumed that the transmission of the non-thermal phonons through the interface (absorber - glue) can again be described by a life time $\tau_{nt,ag}$ (compare to equation 8.14). These non-thermal phonons are supposed to thermalise in the glue within the time τ_{glue} and further propagate into the TES-substrate within the time $\tau_{t,gs}$. As the glue is an amorphous material and has a very small volume (compared to the other detector components) this thermalisation τ_{glue} is expected to occur very fast, i.e., within a time scale τ_{glue} that can be neglected in comparison to the time scale of the detector. Concerning the propagation time $\tau_{t,gs}$ two processes have to be taken into account: the propagation back into the absorber $\tau_{glue-abs}$ and the propagation into the TES-substrate $\tau_{glue-subs}$. To obtain the propagation times for these two processes an equation of the form 8.8 has to be regarded. However, in this case the absorber is given by the glue, while the electron system of the TES corresponds to the phonon system of the TES-substrate or the absorber. As the glue volume is very small in comparison to the absorber and the TES-substrate volume it is assumed that: $C_g \ll C_a, C_s$. Additionally, as mentioned above, $G_{Kgs} \approx G_{Kga}$ is assumed (see figure 8.3). This gives:

$$\tau_{glue-subs} \approx \tau_{glue-abs} \propto \frac{C_g}{G_{Kgs}} \quad (C_g \ll C_a, C_s) \quad (8.19)$$

Hence, the life time of thermal phonons in the glue is given by:

$$\tau_{t,gs} \approx \left(\frac{1}{\tau_{\text{glue-abs}}} + \frac{1}{\tau_{\text{glue-sub}}} \right)^{-1} = \frac{\tau_{\text{glue-sub}}}{2} \quad (8.20)$$

This process leads to an effective thermal power flow $P_{t,ags}(t)$ into the TES-substrate, which is given by the following equation:

$$P_{t,ags}(t) \propto \Theta(t) \left[e^{-\frac{t}{\tau_{t,gs}}} - e^{-\frac{t}{\tau_{nt,as}}} \right] \quad (8.21)$$

$P_{t,ags}(t)$ has to be convoluted with the thermal part of the "TES-detector function" $f_{t, \text{TES-detector}}(t)$ (see equation 8.9). This leads to a signal in the TES of the following form:

$$\begin{aligned} \Delta T(t) &\propto (P_{t,ags} * f_{t, \text{TES-detector}})(t) = & (8.22) \\ &= (P_0 \Theta(t) \left[e^{-\frac{t}{\tau_{t,gs}}} - e^{-\frac{t}{\tau_{nt,as}}} \right]) * \left[A_t (e^{-\frac{t}{\tau_{t,s-\text{TES}}}} - e^{-\frac{t}{\tau_{in,s-\text{TES}}}}) \right] = \\ &= P_0 \Theta(t) \left[d_1 (e^{-\frac{t}{\tau_{t,s-\text{TES}}}} - e^{-\frac{t}{\tau_{t,gs}}}) - d_2 (e^{-\frac{t}{\tau_{t,gs}}} - e^{-\frac{t}{\tau_{in,s-\text{TES}}}}) + \right. \\ &\quad \left. + d_3 (e^{-\frac{t}{\tau_{nt,as}}} - e^{-\frac{t}{\tau_{t,s-\text{TES}}}}) + d_4 (e^{-\frac{t}{\tau_{nt,as}}} - e^{-\frac{t}{\tau_{in,s-\text{TES}}}}) \right] \end{aligned} \quad (8.23)$$

with the amplitudes:

$$d_1 = A_t \frac{\tau_{t,s-\text{TES}} \cdot \tau_{t,gs}}{\tau_{\tau_{nt,as} - t, gs}} \quad (8.24)$$

$$d_2 = A_t \frac{\tau_{t,gs} \cdot \tau_{in,s-\text{TES}}}{\tau_{t,gs} - \tau_{in,s-\text{TES}}} \quad (8.25)$$

$$d_3 = A_t \frac{\tau_{t,s-\text{TES}} \cdot \tau_{nt,as}}{\tau_{\tau_{t,s-\text{TES}} - nt, as}} \quad (8.26)$$

$$d_4 = A_t \frac{\tau_{nt,as} \cdot \tau_{in,s-\text{TES}}}{\tau_{\tau_{nt,as} - in, s-\text{TES}}} \quad (8.27)$$

With $\tau_{in,s-\text{TES}}$ being very small, the second and the fourth term in equation 8.23 can be neglected. Hence, one signal component from the first term and one from the third term remain.

For the first term, the two times $\tau_{t,s-\text{TES}}$ and $\tau_{t,gs}$ have to be compared to find out which time is slower and therefore the decay time of this contribution. As the heat capacity of the glue is expected to be very much smaller than the heat capacity of the TES-substrate, $\tau_{t,s-\text{TES}} > \tau_{t,gs}$ can be assumed (see equation 8.8). Thus, the first term delivers a contribution with a decay time $\tau_{t,s-\text{TES}}$. Concerning the third term in equation 8.23 two possibilities have to be distinguished from each other:

- $\tau_{nt,as} > \tau_{t,s-\text{TES}}$ resulting in two decay times $\tau_{nt,as}$ and $\tau_{t,s-\text{TES}}$
this case is in agreement with case 1.1.1

- $\tau_{\text{nt,as}} < \tau_{\text{t,s- TES}}$ resulting in one decay time $\tau_{\text{t,s- TES}}$
then, case 1.1.1 is excluded

This decision cannot be taken at this point of the discussion, however, when case 2 is discussed, the conclusion can be drawn, that case 1.1.1 has to contribute to the signal and therefore $\tau_{\text{nt,as}} > \tau_{\text{t,s- TES}}$ is true.

To summarise, if $\tau_{\text{nt,as}} > \tau_{\text{t,s- TES}}$, phonons propagating along path 1.2 deliver two decay times $\tau_{\text{nt,as}}$ and $\tau_{\text{t,s- TES}}$, while $\tau_{\text{nt,as}} < \tau_{\text{t,s- TES}}$ would lead to one decay time, $\tau_{\text{t,s- TES}}$.

However, the transport of non-thermal phonons along path 1.2 from the absorber into the glue is determined by the non-thermal phonon life time in the absorber (see equation 8.14), i.e. by the ratio $R_{\text{ntas-crystal}} = \frac{\tau_{\text{crystal}}}{\tau_{\text{coll-glue}}}$ of the collection time of non-thermal phonons in the glue area $\tau_{\text{coll-glue}}$ to the thermalisation time in the crystal τ_{crystal} which are different for the three investigated composite detectors. To estimate the value of this ratio, it is assumed that⁹ $\tau_{\text{crystal}} \propto \frac{V_a}{A_a}$. For simplification, the material-specific transmission probabilities through the interface (absorber - glue) are assumed to be equal for all three detectors. Hence, these considerations are independent from the two possible cases, $\tau_{\text{nt,as}} \gg \tau_{\text{t,s- TES}}$ and lead to:

$$\tau_{\text{nt,ag}} = \left(\left(\frac{2V_a}{A_g \eta_{as} \lambda_{\text{ags}}} \right)^{-1} + (\tau_{\text{crystal}})^{-1} \right)^{-1} \quad (8.28)$$

$$R_{\text{ntas-crystal}} = \frac{\tau_{\text{crystal}}}{\tau_{\text{coll-glue}}} \approx \frac{A_g}{2A_a} \quad (8.29)$$

This ratio determines how effectively non-thermal phonons from the absorber are collected in the glue area with respect to the thermalisation in the crystal. $R_{\text{ntas-crystal}}$ is given in table 8.4 for the three detectors:

detector	$R_{\text{ntas-crystal}}$
"1"	$\sim 4.1 \cdot 10^{-4}$
"2"	$\sim 40 \cdot 10^{-4}$
"3"	$\sim 2.1 \cdot 10^{-4}$

Table 8.4: $R_{\text{ntas-crystal}}$ for the three composite detectors. This ratio determines how effectively the non-thermal phonons from the absorber are collected in the glue area (larger value of $R_{\text{ntas-crystal}}$) with respect to the thermalisation in the absorber crystal (smaller value of $R_{\text{ntas-crystal}}$).

In the glue the non-thermal phonons can either thermalise or are further transported into the TES. These two processes are again competing processes that lead to an effective thermalisation probability in the glue. The

⁹This assumption is justified as the thermalisation in the crystal is expected to arise mainly at the crystal surfaces.

further propagation of the thermalised phonons from the glue into the TES-substrate also competes with another process, the propagation back into the absorber, which again gives an effective transport of thermal phonons from the glue into the TES-substrate.

These processes of thermalising in the glue and further propagation into the TES-substrate are likely to happen with about the same probabilities for all three composite detectors as they are mainly dependent on the (glue volume to glue surface)-ratio, which is assumed to be very similar for all three detectors. Hence, these processes do not influence the fraction of non-thermal phonons from the absorber that in the end reach the TES-substrate as thermal phonons (thermalisation in the glue) via path 1.2.

From this discussion it can be deduced that the probability for non-thermal phonons to propagate into the glue and then thermalise there and thereafter being transported into the TES-substrate (path 1.2) is mainly determined by the ratio $R_{ntas-crystal}$. However, $R_{ntas-crystal}$ is a factor of 10 to 20 smaller for "detector 1" and "detector 3" than for "detector 2" (see table 8.4). Thus, this process of phonons propagating along path 1.2 should be suppressed by a factor of $\sim 10-20$ for "detector 1" and "detector 3" in comparison to "detector 2".

Therefore, for phonons propagating along path 1.2 only a contribution to the signal for "detector 2" is expected.

Hence, if phonons propagating along path 1.1.1 are also expected to contribute to the signal, this conclusion can be aligned with the observation of only one decay time ($\tau_{nt,as}$, attributed to phonons propagating along path 1.1.1) for "detector 1" and "detector 3", and two decay times for "detector 2" (hence, $\tau_{nt,as}$, attributed to phonons propagating along path 1.1.1 and path 1.2, and $\tau_{t,s-TES}$, attributed to phonons propagating along path 1.2).

Thus, it can be possible, that phonons propagating along path 1.1.1 deliver the decay time $\tau_{nt,as}$ for all three detectors and phonons propagating along path 1.2 give the second decay time $\tau_{t,s-TES}$ for "detector 2". This implies for the decay times of "detector 2", together with the above made and justified assumption that $\tau_{nt,as} > \tau_{t,s-TES}$:

$$\begin{aligned}\tau_{t,s-TES} &= \tau_{decay1} \approx 5\text{ms} \\ \tau_{nt,as} &= \tau_{decay2} \approx 12\text{ms}\end{aligned}\tag{8.30}$$

with the observed values for the decay times from table 8.3.

In summary, it can be stated that a non-thermal phonon flow from the absorber into the TES-substrate ($P_{nt,as}(t)$, path 1.1.1 and 1.1.2) can explain one contribution to the temperature signal pulse in the TES with a decay time of $\sim \tau_{nt,as}$. The second decay time observed for "detector 2" can (up to this point in the discussion) be attributed to a contribution from non-thermal phonons from the absorber propagating along path 1.2. However,

in the following discussion we come to the conclusion that if non-thermal phonons propagating along paths 1.1 and 1.1.1 contribute to the signal, no contribution from non-thermal phonons propagating along path 1.2 is possible. We discuss in section 8.3.5 below that a thermal power flow from the absorber into the system (case 2, path 2.1 or 2.2) can also be responsible for this second decay time.

If phonons propagating along path 1.1.1 would be excluded to contribute to the signal in the TES, phonons propagating along path 1.2 could deliver one decay time $\sim \tau_{t,s-tes}$ for "detector 2". In this case, the other decay time for "detector 2" as well as the observed decay times for "detector 1" and "detector 3" have to be attributed to a signal due to phonons propagating along path 2. However, we discuss in section 8.3.5 below that a thermal power flow from the absorber into the system (case 2, path 2.1 or 2.2) cannot be responsible for these decay times.

Additional Arguments for a Non-thermal Phonon Contribution from path 1.1.1 and Exclusion of path 1.2

An additional argument that speaks in favour of the proposition that one decay time of the signal in the TES is caused by non-thermal phonons from the absorber that propagate into the TES (path 1.1.1) with the life time of non-thermal phonons in the absorber $\tau_{nt,as}$ is given by the following discussion, where we propose:

For the investigated detectors "detector 1" and "detector 2" the decay time τ_{decay1} and for "detector 3" the decay time τ_{decay2} (see table 8.3) can be identified with the non-thermal collection time $\tau_{nt,as}$ (path 1.1). With this proposition, equation 8.14 is used in combination with the detector properties given in section 8.2.1, in order to give an estimate for the material-specific parameter ($\overline{\eta_{as}}\lambda_{ags}$):

$$\frac{1}{\tau_{nt,as}} = \frac{A_g \overline{\eta_{as}} \lambda_{ags}}{2V_a} + \frac{1}{\tau_{crystal}} \quad (8.31)$$

The parameter $\tau_{crystal}$ is the thermalisation time of non-thermal phonons in the absorber and $\overline{\eta_{as}}$ describes the probability for non-thermal phonons that crossed the interfaces (absorber - glue - TES-substrate) not to be scattered back into the absorber (path 1.1.2), but to further propagate into the TES and thereafter as thermal phonons into the heat bath (path 1.1.1). Since $\overline{\eta_{as}}$ is essentially determined by the (TES area to glue area)-ratio, $\overline{\eta_{as}}$ is not the same for all the three composite detectors. Also the different materials of the interfaces that are crossed by non-thermal phonons propagating either along path 1.1.1 or along path 1.1.2 have to be taken into account, as they could also influence $\overline{\eta_{as}}$.

For "detector 1" and "detector 3" it can be assumed that most of the non-thermal phonons propagate further via path 1.1.1 ($\overline{\eta_{as}} \approx 1$) as the TES area A_{tes} (providing the effective absorption area for non-thermal phonons prop-

agating along path 1.1.1) is much larger than the glue area A_g (providing the effective absorption area for non-thermal phonons propagating via path 1.1.2). For "detector 2", however, the glue area A_g is at least of the same size as the TES area, A_{TES} . Therefore, for "detector 2" $\overline{\eta_{as}} \neq 1$ is assumed. These assumptions can also be expressed with the following inequalities for the different detectors:

$$\tau_{\text{nt,s-TES}} \ll \tau_{\text{nt,sg}} \quad \text{for "detector 1" and "detector 3"} \quad (8.32)$$

$$\tau_{\text{nt,s-TES}} \approx \tau_{\text{nt,sg}} \quad \text{for "detector 2"} \quad (8.33)$$

where equation 8.32 implies that non-thermal phonons from the TES-substrate are much more effectively collected in the TES than in the glue, while equation 8.33 implies that non-thermal phonons from the TES-substrate are collected in the TES with roughly the same probability as in the glue. The essential parameters controlling these decay times are the collection area for the non-thermal phonons, A_g and A_{TES} , and the material-specific transmission probabilities¹⁰ λ_{ags} and $\lambda_{\text{s-TES}}$, respectively. If the TES area is larger than the glue area, then $\overline{\eta_{as}}$ can be assumed to be close to 1, if the TES area is smaller or equal to the glue area, $\overline{\eta_{as}} \neq 1$, in more detail:

$$\overline{\eta_{as}} \approx \frac{A_{\text{TES}} \lambda_{\text{s-TES}}}{A_g \lambda_{\text{ags}}} \quad \left(\text{if } \frac{A_{\text{TES}}}{A_g} \leq 1 \right) \quad (8.34)$$

is proposed. This yields a value of $\overline{\eta_{as}} \approx 1$ for "detector 1" and "detector 3", while for "detector 2" $\overline{\eta_{as}}$ is assumed to be given by equation 8.34.

For the three composite detectors the values of table 8.1 are introduced into equation 8.31. From these three equations and equation 8.34, the crystal thermalisation time τ_{CaWO_4} , the transmission probability $\lambda_{\text{ags,CaWO}_4}$ for the CaWO_4 crystal and $\overline{\eta_{as}}$ for "detector 2" can be deduced. For "detector 2" and "detector 3" the parameters τ_{CaWO_4} and $\lambda_{\text{ags,CaWO}_4}$ are the same, as the same CaWO_4 crystal was used as absorber. As for "detector 1" another absorber crystal of different material and size was used, $\tau_{\text{Al}_2\text{O}_3}$ cannot be deduced and therefore only an upper limit for $\lambda_{\text{ags,Al}_2\text{O}_3}$ can be given. From the material specific parameters the value for $\tau_{\text{coll-glue}}$ can be given for the "detector 2" and "detector 3", where $\tau_{\text{coll-glue}}$ corresponds to the collection time for non-thermal phonons from the absorber in the glue area.

Table 8.5 summarizes the results.

In summary, the proposition that for "detector 1" and "detector 2" the decay time τ_{decay1} (table 8.3) and for "detector 3" the decay time τ_{decay2} (table 8.3) can be identified with the non-thermal collection time $\tau_{\text{nt,as}}$ (path 1.1) and therefore be attributed to a propagation of non-thermal phonons from the absorber into the TES-substrate and thereafter into the TES and into the heat bath is supported by the following two arguments:

¹⁰It is assumed, that λ_{ags} is the same, independent from which side of the interface (absorber - glue - TES-substrate) the phonons are incident.

8.3 Thermal Detector Model for a Composite Detector (TDM-CD)

det.	$\overline{\eta_{as}}$	$\lambda_{\text{ags,Al}_2\text{O}_3} [\frac{m}{s}]$	$\lambda_{\text{ags,CaWO}_4} [\frac{m}{s}]$	$\overline{\eta_{as}}\lambda_{\text{ags,CaWO}_4} [\frac{m}{s}]$	$\tau_{\text{coll-glue}} [\text{ms}]$	$\tau_{\text{CaWO}_4} [\text{ms}]$
"1"	~ 1	≤ 526	-	-	-	-
"3"	~ 1	-	~ 461	~ 461	~ 35	~ 69
"2"	≥ 0.34	-	~ 461	~ 155	~ 5.4	~ 69

Table 8.5: Estimates for the parameters $\overline{\eta_{as}}$, for $\lambda_{\text{ags,Al}_2\text{O}_3}$ ("detector 1"), $\lambda_{\text{ags,CaWO}_4}$ ("detector 2", "detector 3") and $(\overline{\eta_{as}}\lambda_{\text{ags,CaWO}_4})$ for "detector 2". In the last two columns an estimate for the collection time of non-thermal phonons in the glue area $\tau_{\text{coll-glue}}$ and for the thermalisation time τ_{CaWO_4} of the used CaWO_4 crystal is given.

- All calculated transmission parameters λ_{ags} are in the expected range: the transmission probability, e.g., for an Al_2O_3 -W interface $\overline{\eta} \langle v_{g\perp} \alpha \rangle \sim 742 \frac{m}{s}$ [41].

- When calculating the ratio $\frac{A_{\text{TES}}\lambda_{\text{s-TES}}}{A_g\lambda_{\text{ags,CaWO}_4}}$ for "detector 3" with the value obtained for $\lambda_{\text{ags,CaWO}_4}$ consistently a value larger than 1 is obtained, justifying the proposition, that this ratio determines the fraction of phonons radiated back into the absorber.

Thus, the proposition is strengthened that a non-thermal phonon power flow from the absorber into the TES provides one decay time $\tau_{\text{nt,as}}$ of the temperature signal in the TES.

Based on the proposition that one decay time can be attributed to non-thermal phonons propagating along path 1.1.1, i.e., the observed decay times of "detector 1" and "detector 3" correspond to $\tau_{\text{nt,as}}$, the possibility of a non-thermal phonon contribution from path 1.2 that could account for the second observed decay time of "detector 2" is discussed. From the discussion of case 1.2, under the assumption that case 1.1.1 contributes to the signal, the equations 8.30 were deduced.

From these equations, it can be seen, that the above made discussion of the non-thermal decay times for the three detectors has to be made under the assumption that $\tau_{\text{nt,as}} \approx 12\text{ms}$ for "detector 2" and not, as assumed there, $\tau_{\text{nt,as}} \approx 5\text{ms}$.

However, this discussion, under the assumption $\overline{\eta_{as}} \approx \frac{A_{\text{TES}}\lambda_{\text{s-TES}}}{A_g\lambda_{\text{ags}}}$, leads to the

following equations for "detector 2":

$$\frac{1}{\tau_{nt,as}} = \frac{1}{\tau_{coll-glue}} + \frac{1}{\tau_{crystal}} \quad (8.35)$$

$$\tau_{coll-glue} \approx 5.4\text{ms} \quad (8.36)$$

$$\Rightarrow \frac{1}{12} = \frac{1}{5.4} + \frac{1}{\tau_{crystal}} \quad (8.37)$$

$$\Rightarrow \frac{1}{\tau_{crystal}} = \frac{1}{12} - \frac{1}{5.4} < 0 \quad (8.38)$$

$$(8.39)$$

This is a contradiction.

In summary it is deduced, that if phonons propagating along path 1.1.1 cause a significant signal contribution in the TES, then phonons propagating along path 1.2 can be excluded to cause the second decay time observed for "detector 2". Thus, in this case, the second decay time observed for "detector 2" still has to be explained by a different process. In the following section the possibility that this second decay time is caused by the *thermal* phonon power flow from the absorber (case 2, path 2.1 or 2.2) is discussed.

However, still, case 1.2 under the assumption of *no* contribution from phonons propagating along path 1.1.1 ($\tau_{nt,as} < \tau_{t,s- TES}$) cannot be excluded. This case, however, requires a signal in the TES due to a contribution by thermal phonons for all three detectors. In the following section the discussion of phonons propagating along path 2 shows that this leads to a contradiction.

8.3.5 Case 2: Thermal Phonons from the Absorber

In **case 2** the propagation of thermal phonons from the absorber is discussed. Hence, a power input $P_{t,ag}(t)$ into the glue (path 2.1) or $P_{t,as}(t)$ into the TES-substrate (path 2.2) is discussed. Thus, the thermal conductance G_{Kag} is considered to be larger or at least of the same range as the thermal coupling of the absorber to the heat bath G_{ab} given by the absorber crystal support in the copper holder.

For simplifications it is assumed, that the life time of thermal phonons in the glue propagating into the TES-substrate $\tau_{t,gs}$ can be neglected in comparison to the life time of thermal phonons in the absorber propagating into the glue $\tau_{t,ag}$ ($C_g \ll C_a$). This then results in the assumption that the propagation time for path 2.1 (a in figure 8.3), where thermal phonons are transferred into the glue via the thermal conductance G_{Kag} and thereafter are transferred into the TES-substrate via the thermal conductance G_{Kgs} is equal to the propagation time for path 2.2 (b in figure 8.3), where thermal phonons are directly transferred via the coupling G_{Kas} (including the glue)

into the TES-substrate. This conclusion can again be justified by calculating the resulting signal in the TES-substrate with a convolution.

Therefore, the two cases 2.1 and 2.2 are treated equally. They are characterised by the life time $\tau_{t,as}$ of thermal phonons in the absorber that propagate through the interfaces (absorber - glue - TES-substrate) into the TES-substrate and there deliver the thermal power flow $P_{t,s}(t)$.

Cases 2.1 and 2.2

The power input $P_{t,s}(t)$ into the TES-substrate from the absorber can be described with a function of the form

$$P_t(t) \propto P_0 \Theta(t) \left[e^{-\frac{t}{\tau_{t,as}}} - e^{-\frac{t}{\tau_{nt,as}}} \right] \quad (\text{equation 8.13})$$

that has to be convoluted with the thermal part of the "TES-detector" function

$$f_{t, \text{TES-detector}}(t) = \left[A_t \left(e^{-\frac{t}{\tau_{t,s-\text{TES}}}} - e^{-\frac{t}{\tau_{in,s-\text{TES}}}} \right) \right] \quad (\text{equation 8.9}), \text{ where}$$

$$\tau_{nt,as} = \left(\frac{1}{\tau_{\text{coll-glue}}} + \frac{1}{\tau_{\text{crystal}}} \right)^{-1}.$$

The resulting signal function is given by:

$$\begin{aligned} \Delta T(t) &\propto (P_{t,s} * f_{t, \text{TES-detector}})(t) = \\ &= (\Theta(t) \left[e^{-\frac{t}{\tau_{t,as}}} - e^{-\frac{t}{\tau_{nt,as}}} \right]) * \left[A_t \left(e^{-\frac{t}{\tau_{t,s-\text{TES}}}} - e^{-\frac{t}{\tau_{in,s-\text{TES}}}} \right) \right] = \\ &= P_0 \Theta(t) \left[-g_1 \left(e^{-\frac{t}{\tau_{t,as}}} - e^{-\frac{t}{\tau_{t,s-\text{TES}}}} \right) - g_2 \left(e^{-\frac{t}{\tau_{t,as}}} - e^{-\frac{t}{\tau_{in,s-\text{TES}}}} \right) - \right. \\ &\quad \left. - g_3 \left(e^{-\frac{t}{\tau_{nt,as}}} - e^{-\frac{t}{\tau_{t,s-\text{TES}}}} \right) + g_4 \left(e^{-\frac{t}{\tau_{nt,as}}} - e^{-\frac{t}{\tau_{in,s-\text{TES}}}} \right) \right] \quad (8.40) \end{aligned}$$

with the amplitudes:

$$g_1 = A_t \frac{\tau_{t,s-\text{TES}} \cdot \tau_{t,as}}{\tau_{t,as} - \tau_{t,s-\text{TES}}} \quad (8.41)$$

$$g_2 = A_t \frac{\tau_{in,s-\text{TES}} \cdot \tau_{t,as}}{\tau_{t,as} - \tau_{in,s-\text{TES}}} \quad (8.42)$$

$$g_3 = A_t \frac{\tau_{t,s-\text{TES}} \cdot \tau_{nt,as}}{\tau_{nt,as} - \tau_{t,s-\text{TES}}} \quad (8.43)$$

$$g_4 = A_t \frac{\tau_{in,s-\text{TES}} \cdot \tau_{nt,as}}{\tau_{nt,as} - \tau_{in,s-\text{TES}}} \quad (8.44)$$

With $\tau_{in,s-\text{TES}}$ being very small, the second and fourth term in equation 8.40 can be neglected. Hence, one signal component (first term) with a decay time of $\tau_{t,as}$ (where $\tau_{t,as} > \tau_{t,s-\text{TES}}$ is assumed¹¹) and a contribution from the third term with either a decay time of $\tau_{nt,as}$ or $\tau_{t,s-\text{TES}}$ (depending on which time is larger, see below) remain. Independent of the value of the decay time, it can be seen, that if a thermal phonon signal from the absorber contributes to the signal in the TES always two different decay times should be observed.

¹¹This assumption is justified by the fact that the heat capacity of the absorber is larger than the heat capacity of the TES-substrate, see equation 8.8.

Comparison with the three Composite Detectors

Thus, at first, a conclusion concerning case 1.2 can be drawn. If $\tau_{nt,as} < \tau_{t,s- TES}$, still this case could not be excluded to contribute to the signal. However, a contribution of case 1.2 only gives one decay time for "detector 2". Therefore, a contribution for *all three* detectors by phonons propagating along path 2 is required to explain all observed decay times. As deduced above, for a detector where phonons propagating along path 2 lead to a contribution to the signal, two different decay times have to be observed. This leads to a contradiction with only one decay time being observed for "detector 1" and "detector 3". Thus, case 1.2 can be excluded in any case, for $\tau_{nt,as} < \tau_{t,s- TES}$ and $\tau_{nt,as} > \tau_{t,s- TES}$.

Hence, only case 2 and case 1.1 can contribute to the signal. For case 2, the thermal phonon population in the absorber depends upon how effectively the non-thermal phonons are removed from the absorber (and therefore cannot thermalise in the absorber) and thus cannot contribute to the thermal population there. The value of the parameter $\overline{\eta_{as}}$ determines which fraction of the non-thermal phonons from the absorber reaches the TES-substrate and thereafter propagates into the TES and into the heat bath (path 1.1.1). The fraction $(1-\overline{\eta_{as}})$ is scattered back into the absorber (1.1.2) where the phonons can thermalise and contribute to the thermal phonon population (paths 2.1 and 2.2).

As can be seen from table 8.5, $\overline{\eta_{as}}$ has different values for the three composite detectors. For "detector 1" and "detector 3", $\overline{\eta_{as}} \approx 1$ and therefore the non-thermal phonons are efficiently removed from the absorber (paths 1.1 and 1.1.1). Hence, for "detector 1" and "detector 3" no effective thermal phonon population can be built up in the absorber and no signal arising from thermal phonons from the absorber can be expected. In contrast, for "detector 2", $\overline{\eta_{as}}$ is determined to be ~ 0.34 . This value indicates that only a fraction of ~ 0.34 of the non-thermal phonon population effectively reaches the TES-substrate (path 1.1.1). Thus, a fraction of $\sim (1-0.34)$ of the non-thermal phonon population can effectively thermalise in the absorber and produce a thermal phonon population. This thermal phonon population, in turn, can cause a contribution to the temperature signal in the TES according to the discussion of case 2 (path 2.1 or 2.2) with two decay times $\tau_{t,as}$ and $\tau_{nt,as}$ or $\tau_{t,s- TES}$ (depending on which times is larger, where $\tau_{nt,as}$ corresponds to the decay time delivered by a contribution of non-thermal phonons from the absorber, case 1.1.1).

As for "detector 2" two decay times are observed it could be assumed that, in principle, in this case *only* a thermal power flow from the absorber can cross the interfaces (absorber - glue - TES-substrate) and cause these two decay times. The assumption that *no* non-thermal phonons cross the inter-

face (absorber - glue - TES-substrate) has the consequence that $\tau_{\text{coll-glue}} \rightarrow \infty$ and therefore $\tau_{\text{nt,as}} \rightarrow \tau_{\text{crystal}}$. This means that in the absorber crystal the main "escape" possibility for non-thermal phonons is given by the thermalisation at the crystal surfaces. This leads to $P_t(t) \propto P_0 \Theta(t) \left[e^{-\frac{t}{\tau_{\text{t,as}}}} - e^{-\frac{t}{\tau_{\text{crystal}}}} \right]$ resulting in two decay times $\tau_{\text{t,as}}$ and τ_{crystal} for the two contributions due to the thermal power input. For "detector 2", $\tau_{\text{t,as}}$ and τ_{crystal} correspond to 5ms and 12ms or vice versa. However, any assignment $\tau_{\text{crystal}} \leq 12\text{ms}$, leads to a contradiction. τ_{crystal} is a material-specific parameter and therefore has to be valid also for "detector 3"¹². Inserting $\tau_{\text{crystal}} \leq 12\text{ms}$ into

$$\frac{1}{\tau_{\text{nt,as}}} = \frac{1}{\tau_{\text{coll-glue}}} + \frac{1}{\tau_{\text{crystal}}} \quad (8.45)$$

$$\Rightarrow \frac{1}{23\text{ms}} = \frac{1}{\tau_{\text{coll-glue}}} + \frac{1}{12\text{ms}} \quad (8.46)$$

$$\Rightarrow \tau_{\text{coll-glue}} = \left(\frac{1}{23\text{ms}} - \frac{1}{12\text{ms}} \right)^{-1} < 0 \quad (8.47)$$

This is a contradiction. Another argument is delivered by the fact, that if $\tau_{\text{crystal}} \leq 12\text{ms}$, this would be the fastest process for "detector 3" and an effective thermalisation in the absorber would be given. Hence, a thermal contribution to the signal with a decay time of $\sim \tau_{\text{crystal}}$ should be observed. However, this is not the case, which is another contradiction.

This leads to the conclusion that a non-thermal power flow causes a contribution with a decay time of $\tau_{\text{nt,as}}$ in all three detectors. As concluded from the discussion of case 1.2, if a non-thermal power flow leads to a signal contribution, phonons propagating along path 1.2 cannot deliver significant contributions to the signal in the TES. This implies that the glue cannot be included in the model as thermal component (*a* in figure 8.3) as this would lead to thermalisation in the glue, but only delivers a thermal conductance (*b* in figure 8.3).

Therefore, for case 2, phonons propagating along path 2.1 (glue as thermal component) don't have to be included in the model, as this path does not exist.

For "detector 2", the second decay time (12ms) has to be explained by a thermal power flow from the absorber into the system (case 2.2). A thermal phonon power flow, however, delivers two contributions with decay times $\tau_{\text{t,as}}$ and ($\tau_{\text{nt,as}}$ or $\tau_{\text{t,s-TES}}$). As in total only two decay times are observed with "detector 2", the second decay time due to the thermal phonon power flow has to be $\tau_{\text{nt,as}}$, the same as for non-thermal phonons (paths 1.1 and 1.1.1). From this discussion it can be concluded that a thermal power flow delivers two contributions with the decay times $\tau_{\text{t,as}}$ and $\tau_{\text{nt,as}}$.

¹²The same absorber crystal was used.

8.3.6 Conclusions

In our model the following assumptions were made:

- The life time of non-thermal phonons in the absorber can be described by:

$$\frac{1}{\tau_{nt,as}} = \frac{A_g \overline{\eta_{as}} \lambda_{ags}}{2V_a} + \frac{1}{\tau_{crystal}}$$

- The transmission probability $\overline{\eta_{as}}$ for non-thermal phonon transport through the glue gives the fraction of non-thermal phonons that propagate further from the TES-substrate into the TES in relation to the non-thermal phonons that propagate back from the TES-substrate into the absorber:

$$\overline{\eta_{as}} \approx \frac{A_{TES} \lambda_{s-TES}}{A_g \lambda_{ags}} \neq 1 \text{ if this ratio is } < 1$$

$$\overline{\eta_{as}} \approx 1 \text{ if this ratio is } > 1$$

- The heat capacity of the glue can be neglected in comparison to the heat capacity of the absorber and the substrate, respectively:

$$C_g \ll C_a, C_s$$

From our model the following conclusions can be drawn:

- The glue should not be included as a thermal component with a heat capacity and a temperature, where non-thermal phonons can thermalise, but has to be included as a contribution to the thermal conductance G_{Kas} (b in figure 8.3).
- Non-thermal phonons having a life time of $\tau_{nt,as}$ in the absorber propagate further through the interfaces (absorber - glue - TES-substrate) into the TES-substrate via path 1.1.1.
- If $\overline{\eta_{as}} \neq 1$, non-thermal phonons decaying in the absorber and propagating via the thermal conductance G_{Kas} (including the glue) into the TES-substrate with $\tau_{t,as}$ give a significant contribution to the signal.
- Hence, depending on $\overline{\eta_{as}}$, the signal shape $\Delta T(t)$ expected in the thermometer can be calculated as follows (the significant contributions are given):

a) if $\overline{\eta_{as}} \approx 1$

$$\Delta T(t) \propto \Theta(t) P_0 \left[c_1 \left(e^{-\frac{t}{\tau_{nt,as}}} - e^{-\frac{t}{\tau_{nt,s- TES}}} \right) - c_3 \left(e^{-\frac{t}{\tau_{nt,as}}} - e^{-\frac{t}{\tau_{t,s- TES}}} \right) \right] \quad (8.48)$$

with

$$c_1 = (A_{nt} - A_t) \frac{\tau_{nt,s- TES} \cdot \tau_{nt,as}}{\tau_{nt,as} - \tau_{nt,s- TES}} \quad (8.49)$$

$$c_3 = A_{nt} \frac{\tau_{t,s- TES} \cdot \tau_{nt,as}}{\tau_{nt,as} - \tau_{t,s- TES}} \quad (8.50)$$

where

$$\frac{1}{\tau_{nt,as}} = \frac{A_g \lambda_{ags}}{2V_a} + \frac{1}{\tau_{crystal}} \quad (8.51)$$

$\tau_{nt,s- TES}$ and $\tau_{t,s- TES}$ are characteristical times of the "TES-detector". First estimates for the transmission probability λ_{ags} are given in table 8.5.

b) if $\overline{\eta_{as}} \approx \frac{A_{TES} \lambda_{s- TES}}{A_g \lambda_{ags}}$

$$\Delta T(t) \propto \Theta(t) P_0 \left[c_1 \left(e^{-\frac{t}{\tau_{nt,as}}} - e^{-\frac{t}{\tau_{nt,s- TES}}} \right) - c_3 \left(e^{-\frac{t}{\tau_{nt,as}}} - e^{-\frac{t}{\tau_{t,s- TES}}} \right) - g_1 \left(e^{-\frac{t}{\tau_{t,as}}} - e^{-\frac{t}{\tau_{t,s- TES}}} \right) - g_3 \left(e^{-\frac{t}{\tau_{nt,as}}} - e^{-\frac{t}{\tau_{t,s- TES}}} \right) \right] \quad (8.52)$$

with

$$c_1 = (A_{nt} - A_t) \frac{\tau_{nt,s- TES} \cdot \tau_{nt,as}}{\tau_{nt,as} - \tau_{nt,s- TES}} \quad (8.53)$$

$$c_3 = A_{nt} \frac{\tau_{t,s- TES} \cdot \tau_{nt,as}}{\tau_{nt,as} - \tau_{t,s- TES}} \quad (8.54)$$

$$g_1 = A_t \frac{\tau_{t,s- TES} \cdot \tau_{t,as}}{\tau_{t,as} - \tau_{t,s- TES}} \quad (8.55)$$

$$g_3 = A_t \frac{\tau_{t,s- TES} \cdot \tau_{nt,as}}{\tau_{nt,as} - \tau_{t,s- TES}} \quad (8.56)$$

where

$$\frac{1}{\tau_{nt,as}} = \frac{A_g \lambda_{ags}}{2V_a} + \frac{1}{\tau_{crystal}} \quad (8.57)$$

$$\tau_{t,as} \text{ is a function of } G_{Kas} \quad (8.58)$$

$\tau_{nt,s- TES}$ and $\tau_{t,s- TES}$ are the characteristic times of the "TES-detector". First estimates for the transmission probability λ_{ags} and of $\overline{\eta_{as}}$ (dependent on the absorber material and size) are given in table 8.5.

- $\tau_{nt,as} > \tau_{t,s- TES}$ is true for the three investigated composite detectors.

For the investigated composite detectors the following processes are expected to account for the observed signal shapes:

- "detector 1": effectively only non-thermal phonons reach the TES, where they are collected very efficiently (due to $\overline{\eta_{as}} \approx 1$) into the TES (path 1.1.1), i.e. the thermalisation in the TES-substrate does not significantly contribute to the resulting signal shape in the TES. The non-thermal phonons are removed from the system "before" they can build up a thermal phonon population in the absorber, hence, no contribution from thermal phonons is expected. Thus, path 1.1.1 is the essential process and determines the signal shape in the TES. Only one decay time $\tau_{nt,as}$ due to non-thermal phonons from the absorber is observed.
- "detector 2": effectively only a fraction $\overline{\eta_{as}}$ (due to the small (TES area to glue area)-ratio R_{TES-g}) of non-thermal phonons from the absorber reaches the TES via path 1.1.1 delivering one component (decay time $\tau_{nt,as}$) to the signal in the TES (same process as in "detector 1"). A fraction $(1-\overline{\eta_{as}})$ is transferred back into the absorber (via path 1.1.2), where they can efficiently contribute to the thermal phonon population and from which they propagate as thermal phonons into the TES-substrate via the thermal conductance G_{Kas} , and then into the TES (path 2.2), delivering two components (decay times $\tau_{nt,as}$ and $\tau_{t,as}$) to the signal. As a consequence two decay times, $\tau_{nt,as}$ (due to non-thermal and thermal phonons from the absorber) and $\tau_{t,as}$ (due to thermal phonons from the absorber) are observed.
- "detector 3": as for "detector 1", effectively only non-thermal phonons reach the TES via path 1.1.1 due to $\overline{\eta_{as}} \approx 1$ (same process as in "detector 1"). Therefore, path 1.1.1 is the essential process and determines the signal shape in the TES. Again only one decay time $\tau_{nt,as}$ due to non-thermal phonons from the absorber is observed.

In summary, from the presented model one decay time, $\tau_{nt,as}$ due to non-thermal phonons from the absorber (path 1.1.1) is expected for every detector. However, the appearance of a second decay time, $\tau_{t,as}$ due to thermal phonons from the absorber (path 2.2) is determined by the value of the transmission probability $\overline{\eta_{as}}$ which is in turn controlled by the effective (TES area to glue area)-ratio $\frac{A_{TES}\lambda_{s-TES}}{A_g\lambda_{ags}}$.

8.3.7 Future Experimental Tests of the Model

In order to further check the validity of this model additional experiments are suggested:

1. To check that the propagation of non-thermal phonons from the absorber into the TES-substrate (path 1.1.1) contributes only one decay time to the signal, i.e., $\tau_{nt,as} > \tau_{t,s-TES}$ (see discussion of **case 1.1.1**),

signals from direct events in the TES-substrates used in our composite detectors have to be recorded.

From these direct events the non-thermal and thermal collection times $\tau_{nt,s-TES}$ and $\tau_{t,s-TES}$ of the TES detector can be deduced and compared to the decay times $\tau_{nt,as}$ which have been determined in this work. If our model is correct, $\tau_{nt,as} > \tau_{t,s-TES}$ has to be found for all three composite detectors.

2. Suppose $\tau_{t,s-TES}$ has been measured in experiment 1. To check that it can be excluded, that phonons propagating along path 1,2, i.e., thermalise in the glue, $\tau_{t,s-TES}$ has to be compared to the observed decay times for "detector 2". If our model is correct, no match should be found, and in addition to $\tau_{t,s-TES} < \tau_{nt,as}$ also $\tau_{t,s-TES} < 5\text{ms}$ should be observed.
3. To check that thermal phonons can cross the (absorber - glue - TES-substrate) as observed for "detector 2", i.e., that this process can contribute the second decay time a composite detector analogous to "detector 1" (sapphire absorber ($10 \times 20 \times 1\text{mm}^3$), sapphire TES-substrate ($3 \times 5 \times 1\text{mm}^3$) with a W-TES ($\varnothing=2\text{mm}$), glue spot ($A_g \approx 0.38\text{mm}^2$)) should be built, however, in addition a heater has to be sputtered onto the surface of the absorber crystal. This heater is used to inject thermal phonons into the absorber. The rise time of the injected heater pulses has to be equal to or faster than the rise time of the composite detector, otherwise the rise time can cause an additional decay time observed in the signal.

To deduce the non-thermal and thermal collection times $\tau_{nt,s-TES}$ and $\tau_{t,s-TES}$ of the TES detector, signals due to direct events in the used TES-substrate have to be recorded.

Signals due to events in the absorber crystal also have to be recorded. From these absorber hits, signals in the TES with only one decay time $\tau_{nt,as}$ are expected.

In addition, signals due to heater pulses into the absorber have to be recorded. From these absorber heat pulses, signals in the TES with only one decay time $\tau_{t,as}$ are expected.

If our model is correct and all these decay times are observed in the described way, this implies the following: the fact, that no decay time due to a thermal contribution from the absorber can be observed for the absorber hits cannot be explained with the argument, that thermal phonons cannot cross a "small" glue area A_g but can, however, as described in our model, be attributed to a "large" $R_{TES-g} > 1$. A large value of R_{TES-g} has the consequence that the non-thermal phonons are very efficiently removed from the system and therefore no thermal population in the absorber can be established.

4. Our model predicts that the ratio $R_{TES-g} \frac{A_{TES} \lambda_{s-TES}}{A_g \lambda_{ags}}$ determines if two decay times or only one can be observed in the temperature signal: if

$R_{\text{TES-g}} > 1$, then $\overline{\eta_{as}} \approx 1$ (see **comparison with the three composite detectors**) and only one decay time ($\tau_{\text{nt,as}}$) should be present. If, however, $R_{\text{TES-g}} \leq 1$, then $\overline{\eta_{as}} < 1$ (see **comparison with the three composite detectors**) and two decay times ($\tau_{\text{nt,as}}$ and $\tau_{\text{t,as}}$) should be observed independent of the absorber size or the absolute areas of the TES or the glue area. To check these predictions two pairs of detectors should be built with the same absorber crystal: one pair being characterised by the same $R_{\text{TES-g}} > 1$, however, with different values for the areas A_{TES} and A_{g} ; the second pair being characterised by the same $R_{\text{TES-g}} \leq 1$, and again with different values for the areas A_{TES} and A_{g} . For each pair, signals due to events in the absorber have to be recorded. If our model is correct, for both detectors of the first pair ($R_{\text{TES-g}} > 1$) only one decay time ($\tau_{\text{nt,as}}$) for each detector should be observed, while for both detectors of the second pair ($R_{\text{TES-g}} > 1$) two decay times ($\tau_{\text{nt,as}}$ and $\tau_{\text{t,as}}$) should be observed. For the case of two observed decay times the ratio of the amplitudes of the two contributions should be similar for the two detectors of the pair.

If the decay times are observed as predicted, this implies that the number of decay times contributing to the resulting temperature signal in the TES is not determined by the (absorber volume to glue area) or (absorber volume to TES area)-ratio, but is, according to our model, determined instead by the ratio $R_{\text{TES-g}} = \frac{A_{\text{TES}}\lambda_{\text{s-TES}}}{A_{\text{g}}\lambda_{\text{ags}}}$.

Chapter 9

Summary and Outlook

In this work the potential of the rf-sputtering technique to produce tungsten thin films for the use as transition edge sensors (TESs) in the CRESST experiment has been investigated. With these tungsten thin films composite detectors were realised. The composite detector design has been examined concerning its applicability to detectors used for Dark Matter experiments like CRESST and EURECA. In addition, an extended thermal detector model was developed which describes the processes occurring in a composite cryogenic detector in a consistent way.

Dark Matter search experiments like CRESST or EURECA are aimed at the direct detection of Dark Matter particles, so-called WIMPs (weakly interacting massive particles). The interaction of WIMPs with ordinary baryonic matter is expected to occur via WIMP-nucleon scattering. With the CRESST and the planned EURECA experiment it is attempted to detect these events with the help of modularised cryogenic detectors. The CRESST detectors are equipped with a tungsten TES (transition edge sensor) to read out the temperature signal produced by an event in the absorber. The simultaneous measurement of the phonon and the scintillation light signal with a CRESST detector module allows efficient discrimination between nuclear recoil events and electron recoils due to background events.

In order to efficiently set new limits on the WIMP-nucleon cross section and to exploit the parameter space for WIMP mass and interaction cross section favoured by the SUSY theory predictions, it is necessary to further increase the target material and additionally enable the application of different target materials to independently check the obtained results. For this purpose a highly reproducible fabrication of detector modules is required.

Tungsten TESs that can be used for CRESST have to exhibit a transition temperature T_c of $\sim 10\text{-}15\text{mK}$ and a transition width in the range of 1 mK . These required properties of the TES can be found for tungsten thin films with the $\alpha\text{-W}$ crystal structure (bcc-lattice structure). To investigate the potential of the production of tungsten TESs for the CRESST experiment

with the rf-sputtering technique several tungsten thin films were produced and measured. The obtained results indicate that the sputtered tungsten thin films do exhibit the required α -W structure, but show transition temperatures of ~ 28 - 63 mK. These elevated transition temperatures could successfully be linked to a stressed crystal lattice and an inhomogeneous and grained growth of the thin films. Several possibilities to adjust the deposition parameters, for example the optimisation of the substrate temperature and the deposition rate, have been identified and are planned to be realised in the future.

Concerning the problem that the transition temperature and width of the produced tungsten thin films can be influenced in an uncontrolled way by postprocessing steps as, e.g., structuring and etching processes, a technique to produce initially smaller tungsten thin films where no postprocessing steps are required has been developed. This technique is based on a special shadow mask that is used for the rf-sputtering process. This shadow mask can accommodate eight small crystal substrates onto which tungsten thin films with a diameter of 2 mm each can be deposited. The tungsten thin films fabricated in this way indicate that this technique can successfully be applied to produce several tungsten thin films in one deposition cycle. Up to now it has not yet been achieved that all individual tungsten thin films of one batch exhibit more or less the same properties. However, several techniques are presented that will further improve the production process to reach this goal. With two of these small tungsten thin films so-called composite detectors have been built.

The presented composite detector design allows to decouple the TES-production process from the choice and treatment of the absorber material. This is achieved by using the small tungsten thin films that were produced on separate TES-substrates and attaching these small thermometers to an absorber crystal with a glue spot or glue layer. One composite detector was realised with a relatively small absorber mass in combination with a small glue spot, while for the second composite detector a plain glue layer in combination with a relatively large absorber mass was used. With the two composite detectors it could successfully be demonstrated that good energy resolutions and thresholds can be achieved. Especially the composite detector with a small absorber mass showed highly satisfying results. The other composite detector with a large absorber mass in combination with a plain glue layer also exhibits a promising potential.

In order to understand the results and signals observed with the composite detectors an extended thermal detector model for composite detectors on the basis of the model described in [41] was developed. With this extended model the observed pulse shapes of the investigated composite detectors can be explained successfully. The temperature signal in the TES is mainly caused by two processes: the propagation of non-thermal phonons from the

absorber all the way through the glue into the TES and the propagation of thermal phonons from the absorber to the TES via the thermal conductance provided by the glue. The contribution of the second process to the temperature signal in the TES strongly depends on the details of the detector construction. Further experiments are suggested to test the validity of the extended model.

List of Figures

2.1	Sketch of the principle setup of a cryogenic calorimeter. The main parts are shown: the absorber crystal, the TES and the weak thermal link to the heat bath, as well as the thermal contacts of the TES. Additionally, the energy deposition of an incident particle in the absorber crystal is illustrated.	10
2.2	Resistance of a tungsten thin film in the transition region from the super- to normalconducting state. A small change in temperature ΔT leads to a measurable change in resistance ΔR . Under ideal conditions this relation can be linearised. Inset: Sketch of the read out circuit for the TES used in CRESST with R_T : thermometer/ TES resistance, R_S : constant shunt resistance, L_I : SQUID input coil, I_0 : constant bias current. A change in R_T changes the branching of I_0 and therefore the magnetic flux through L_I which is is read out by a SQUID. . .	11
2.3	a) Schematic drawing of a CRESST-II detector module consisting of a CaWO_4 phonon detector and a separate light detector, both enclosed in a reflective housing. The tungsten TESs are read out via SQUIDs. b) Photo of a CRESST detector module, with (left) the light detector (silicon) and (right) the phonon detector (CaWO_4).	13
2.4	Pulse height in the light detector versus pulse height in the phonon detector (CaWO_4 crystal) [46]. The scatter plot on the left side was measured with an electron (^{90}Sr source) and a photon source (^{57}Co). Hence, the events in the resulting band are due to electron recoils. To measure the plot on the right a neutron source was added. Therefore, the events in the lower band are caused by nuclear recoil events in the detector leading to a reduced light generation compared to electron-like interactions.	13
2.5	Detailed schematic drawing of a CRESST-II phonon detector TES with thermal and electrical contacts, as well as the SQUID read out circuit.	15
2.6	Schematic drawing of a CRESST-II light detector TES and its thermal and electrical contacts.	16

2.7	Cross section of the CRESST building in Hall A (3600m.w.e.) at the LNGS (Laboratori Nazionali del Gran Sasso). The external shielding is shown in both its open (green-white) and closed (blue-red) positions.	18
2.8	Sketch of the CRESST-II Cryostat [54].	19
2.9	Exclusion limits in terms of coherent (spin-independent) scattering from first data taking with detector modules developed for CRESST-II [18]. Assuming a quenching factor of 7.4 to identify nuclear recoils the solid red curve is obtained. Applying a quenching factor of 40 to identify tungsten recoils to the data of the module Daisy/BE13 the dashed red line is obtained [18]. Regions above the curves are excluded at 90% CL. The closed region represents the claim of a positive WIMP modulation signal by the DAMA collaboration [55]. The green line represents the exclusion limit set by the EDELWEISS experiment [56], while the blue line gives the exclusion limit of the CDMS experiment [57].	21
2.10	Current exclusion limits from the direct search Dark Matter experiments, the EDELWEISS experiment (green line) [56], the CRESST-II experiment [58] (red curve), the current WARP limit [38] (dark grey line), an improved CDMS limit [26] (blue line) and the current limit set by the XENON10 experiment, a noble gas experiment, (brown line) [59] are shown together with the DAMA 3σ signal region (red area) and the parameter space favoured by the SUSY theory (pink area) [60].	22
3.1	X-ray diffraction pattern and crystal unit cell (bcc structure) of α -W. ϑ - 2ϑ measurements were performed with the Cu- $K_{\alpha 1}$ line [62].	27
3.2	X-ray diffraction pattern and crystal unit cell (Cr_3Si structure) of β -W. ϑ - 2ϑ measurements were performed with the Cu- $K_{\alpha 1}$ line [62].	28
4.1	Schematic drawing of an rf-sputtering system.	36
4.2	Sketch of a circular planar magnetron cathode: a) side view. b) top view.	37
4.3	Front view of the magnetron sputtering facility. The electronic periphery is not included in the picture.	38
4.4	Tungsten filament of the ion source. The length of the filament is 2 cm.	40
4.5	Discharge chamber of the ion source. On top the acceleration grid can be seen. The diameter of the grid is 3cm.	41

4.6 Complete setup of the ion source together with the plasma bridge neutraliser. On top of the ion source the acceleration grid can be seen. The PBN discharge chamber is mounted above the ion source. 43

5.1 $\vartheta - 2\vartheta$ measurements of a) a sapphire single-crystal substrate (c-plane) and b) the tungsten film "081106" sputtered onto a sapphire single crystal (c-plane). In picture a) the two peaks due to the two Cu-K $_{\alpha}$ lines diffracted by the (0002) sapphire lattice planes (FWHM ~ 0.07) can be seen. Picture b) shows the same two peaks and additionally one broad peak (FWHM ~ 0.54) due to diffraction by lattice planes of the tungsten thin film. This broad peak includes diffraction on the W lattice planes due to both Cu-K $_{\alpha}$ lines. 53

5.2 Sketch of the geometry used for the four-point resistance measurement of the sputtered tungsten thin film (film thickness $d=1200\text{\AA}$, length $l=1\text{cm}$, cross-section $A\approx 9\cdot 10^{-6}\text{cm}^2$). 55

5.3 Transitions from super- to normalconducting state of the sputtered tungsten thin films "081106", "151106" and "241106". The transitions shown in figure a), b) and c) are recorded with indium squeezed (IS) contacts, while figure d) shows again the transition of the tungsten thin film "241106" this time recorded with Al wires directly bonded (DB) onto the tungsten thin film. 57

6.1 Tantalum shadow mask used for the production of the "small" sputtered tungsten thin films. The substrate holder with the exchangeable shadow mask can be seen. The positions for the eight substrates are shown, corresponding to the film numbers of the produced film (see section 6.3). One cutout can accommodate a substrate of $3\times 5\text{mm}^2$. The unsealed area for each film is given by a circle with a diameter of $\sim 2\text{mm}$ 66

6.2 Transitions from super- to normalconducting state of the sputtered tungsten thin films "220207-2,3,5,6". For the transition of film "220207-2" shown in figure a) the normalconducting condition was reached at approximately the endpoint of the shown dataset. The transition of film "220207-6" shown in figure d) looks a bit irregular which can be assigned to the process of data taking and the performance of the utilised SQUID. 68

7.1	Sketch of the composite detector design applied for the detectors investigated in sections 7.2 and 7.3. The absorber crystal with the attached small TES-substrate can be seen. For the "glueing technique 1" a small glue spot is used while for the "glueing technique 2" a plain layer of glue of the size of the TES-substrate is applied.	72
7.2	Sketch of a composite detector inside a copper holder. The crystal is supported in such a way that it is thermally decoupled from the holder. The TES (on the small substrate) with its electrical and thermal contacts (bonded Al wires to insulated solder/bond pads on the copper holder and Au wires to the copper holder) can be seen. The copper holder is thermally coupled to the mixing chamber and therefore serves as heat bath for the TES. Additionally, the temperature sensor (speer resistor) and the resistance heater that are used for temperature stabilisation of the TES are indicated.	74
7.3	Composite "detector 1" and "detector 2" and the transitions of the used W-TESs. In figure a) the composite "detector 1" with a sapphire absorber of $10 \times 20 \times 1 \text{mm}^3$ size and the W-TES-3 is shown. The absorber is supported by sapphire balls in the copper holder. The electrical (bonded Al wires) and thermal (bonded Au wires) contacts of the TES can be seen. In figure b) the transition of the used W-TES-3 is given. Figure c) shows the composite "detector 2" with a CaWO_4 crystal absorber of cylindrical shape with a diameter and a height of 20mm and the W-TES-6. The crystal is fixed in the copper holder by teflon supports that thermally decouple it from the holder. A reflective foil is installed around the crystal to enable efficient scintillation light detection with a light detector. Electrical and thermal contacts of the TES to insulated solder/bond pads and the copper holder, respectively, are again provided by bonded Al and Au wires. In figure d) the transition of the used W-TES-6 is shown.	75
7.4	Sketch of the setup used to record a spectrum with an ^{55}Fe source with "detector 1". The distance between the source and the detector was $\sim 20\text{mm}$. The hole in the aperture has a diameter of $\sim 1\text{mm}$	76
7.5	^{55}Fe spectrum recorded with "detector 1". The separation of the Mn-K_α and Mn-K_β lines can be clearly seen. An energy threshold E_{thr} of 262eV and a resolution (FWHM) of 158eV at 6keV were achieved.	77

7.6	^{137}Cs spectrum recorded with "detector 2". The sharp peak around 0keV includes noise samples, the broad distribution is due to muon induced events in the detector and the peak at 662keV corresponds to the ^{137}Cs line. An energy threshold E_{thr} of 10keV and a resolution (FWHM) of 32 keV at 662keV were achieved.	78
7.7	W- K_{α} escape peak and ^{57}Co lines recorded with "detector 2". A resolution (FWHM) of 9.6 keV at 122keV and of 7.6keV at 63keV were achieved.	79
8.1	Thermal model of a cryogenic detector with a directly deposited TES (thermometer) [41]. T_b is the heat bath temperature, T_e and T_a are the temperatures of the TES electron system and the absorber phonon system, respectively, C_e and C_a are their heat capacities. Phonons that thermalise in the electron system of the TES or in the absorber cause the energy flows P_e or P_a into the TES and the absorber, respectively. G_{ab} , G_{eb} and G_{ea} are the thermal conductances.	83
8.2	Typical signal shape observed in the TES of a cryogenic detector. The black line gives the total signal shape. The red line represents the contribution by non-thermal phonons, while the blue line gives the signal contribution due to thermal phonons.	86
8.3	Thermal model of a composite detector. For the glue two alternative representations a and b are presented. Alternative a shows the glue as thermal component to which a heat capacity C_g and a temperature T_g can be related. Alternative b shows the glue representing a thermal conductance G_{Kas} between the absorber and the TES-substrate. T_b , T_e , T_a , T_s and T_g are the temperatures of the heat bath, the thermometer (TES) electron system, the absorber phonon system, the TES-substrate phonon system and the glue phonon system, respectively. C_e , C_a , C_s and C_g are their heat capacities, and P_e , P_a , P_s and P_g are the energy flows into the particular system caused by non-thermal phonons thermalising in the respective component. G_{ab} , G_{eb} and G_{ega} are the thermal conductances. .	91

8.4 Sketch of the most important propagation possibilities for non-thermal (red arrows) and thermal phonons (blue arrows). The green arrows depict the decay of non-thermal into thermal phonons. For the thermal phonons only the propagation towards the heat bath is given. The influence of the glue is characterised in two ways: the glue can either be considered as a thermal component with a heat capacity and a temperature where non-thermal phonons can decay or the glue can contribute a thermal conductance to the system (see a and b in figure 8.3). The numbers given correspond to the different phonon propagations discussed below. 92

List of Tables

1.1	Parameters of the Concordance Model (assuming a simple flat Λ -CDM model; values on the basis of the WMAP 3-year dataset) [12]	5
3.1	Properties of the different tungsten crystal structures.	33
4.1	Substrate temperatures T_{sub} measured for different heater temperatures T_{htr} . The setpoint temperature T_{set} is controlled by a heater controller. The observed oscillations in the substrate temperature, osc. of T_{sub} , originate from oscillations of the heater temperature, osc. of T_{htr}	45
5.1	Deposition parameters of the tungsten thin films investigated in section 5.2. The first column gives the number of the film. The second column tells if ion gun precleaning/roughening (IG) was performed. The substrate temperature T_{sub} during deposition is depicted in the last column. All other deposition parameters (see section 4.5) are kept the same.	52
5.2	Results for various W thin films and a sapphire substrate. The full width at half maximum (FWHM) values of the 2ϑ peaks of the W thin films is much larger than that of the sapphire substrate. The last two columns give the interplanar distance d and the lattice constant a assuming that an α -W structure is present. The last line gives the corresponding results for a sapphire single-crystal substrate (c-plane) as reference. An upper limit for the systematic error of the 2ϑ values is estimated from the difference between the 2ϑ results obtained by different fit methods: a cognitive and a parabolic fit. This difference yields $\sim 0.02^\circ$. From this value it can be seen that within the error bars the measured 2ϑ values for "081106" and "151106" (or "170107") can be separated.	54
5.3	Measured room temperature and helium temperature resistances R_{300K} and $R_{4.2K}$ for various W thin films. The error is estimated to be 0.01Ω . The resulting RRR values calculated with equation 3.5 are given in the last column. The error for RRR is about 0.02Ω	54

5.4	Measured resistances R_{300K} and $R_{4.2K}$ for various W thin films are given. The resulting specific resistances ρ_{300K} and $\rho_{4.2K}$ for a conservative estimate (large values) calculated with equation 5.2 are also presented. The error for the resistivity is about $0.09\mu\Omega\text{cm}$. Therefore, the value for film "241106" is clearly distinguishable within the error bars.	56
5.5	Transition temperatures T_c measured for various W thin films in a ^3He - ^4He cryostat with a base temperature of $\sim 15\text{mK}$. The measurements were carried out either with squeezed indium (SI) or directly bonded (DB) contacts. Additionally, the width of the transition ΔT_c and the difference in resistance ΔR of the normal to the superconducting state are given.	56
5.6	Properties of the produced tungsten thin films. The different columns contain the following information: iongun precleaning/roughening (IG), substrate temperature during deposition (T_{sub}), measured angle 2ϑ , calculated lattice constant a for α -W structure (bcc), measured room temperature and liquid helium temperature resistances R_{300K} and $R_{4.2K}$, residual resistance ration (RRR), estimated specific resistivity at room temperature (ρ_{300K}) and at 4.2K ($\rho_{4.2K}$), the measured temperature (T_c) and width (ΔT_c) of the superconducting transition and the difference in resistivity ΔR between super- to normalconducting state. Concerning the error bars for the individual values see tables 5.1 to 5.5.	58
6.1	Transition temperatures of "small" sputtered tungsten thin films produced with the shadow mask described in section 6.2. Each circular film area covers a size of $\sim 12\text{mm}^2$. T_c was measured in a ^3He - ^4He dilution refrigerator (base-temperature: $\sim 15\text{mK}$). ΔT_c denotes the width of the transition and ΔR the difference in resistance from the normal to the superconducting state.	67
8.1	Main properties of the three investigated composite detectors. The absorber material is given in the second column. V_a denotes the absorber volume, A_g gives an estimated value for the glue area and d_g an estimate for the thickness of the glue layer. R_{ag} is the estimated absorber-volume to glue-volume ratio. . .	87
8.2	Properties of the (TES-substrate - TES) system of the three composite detectors. Columns two and three list the materials used for the substrates and TESs, respectively. V_s is the TES-substrate volume, A_{TES} is the TES area and $\tau_{\text{nt-sTES}}$ is the calculated upper limit for the collection time of the non-thermal phonons from the TES-substrate into the TES. . . .	88

8.3	Rise and decay times of the fitted standard event for the three detectors. For "detector 1" only one decay time was found. For "detector 3" only the slow decay time τ_{decay2} is included in the discussion as the fast decay time τ_{decay1} can be attributed to a process not connected to the absorber crystal of the composite detector (see discussion below).	89
8.4	$R_{\text{ntas-crystal}}$ for the three composite detectors. This ratio determines how effectively the non-thermal phonons from the absorber are collected in the glue area (larger value of $R_{\text{ntas-crystal}}$) with respect to the thermalisation in the absorber crystal (smaller value of $R_{\text{ntas-crystal}}$).	99
8.5	Estimates for the parameters $\overline{\eta_{as}}$, for $\lambda_{\text{ags,Al}_2\text{O}_3}$ ("detector 1"), $\lambda_{\text{ags,CaWO}_4}$ ("detector 2", "detector 3") and $(\overline{\eta_{as}}\lambda_{\text{ags,CaWO}_4})$ for "detector 2". In the last two columns an estimate for the collection time of non-thermal phonons in the glue area $\tau_{\text{coll-glu}}$ and for the thermalisation time τ_{CaWO_4} of the used CaWO_4 crystal is given.	103

Bibliography

- [1] S. van den Bergh, The Early History of Dark Matter. *Publ. Astron. Soc. Pacific* **111**, 657 (1999).
- [2] J. Bekenstein, A Primer to Relativistic MOND Theory. (in *EAS Publications Series*, Vol. 20 of *Engineering and Science*, 2006), p. 225.
- [3] M. Milgrom, A modification of the Newtonian dynamics as a possible alternative to the hidden mass hypothesis. *Astrophys. J.* **270**, 365 (1983).
- [4] F. Zwicky, On the Masses of Nebulae and of Clusters of Nebulae. *Astrophys. J.* **86**, 217 (1937).
- [5] K. Freese et al., Death of baryonic dark matter.. *Phys. Rep.* **333**, 183 (2000).
- [6] B. Carr, Baryonic and Non-Baryonic Dark Matter. (in *Birth and Evolution of the Universe, Proceedings of the 4th RESCEU International Symposium at the University of Tokyo, Japan, Universal Academy Press*, 2001), p. 55.
- [7] K. C. Sahu, Microlensing towards the Magellanic Clouds: nature of the lenses and implications on dark matter. (in *The Dark Universe: Matter, Energy and Gravity*, Vol. 15 of *Space Telescope Science Institute symposium series, Cambridge University Press*, 2003), p. 14.
- [8] L. M. Krauss, Dark Matter Candidates: What Cold, ..and What's Not. arXiv:hep-ex/0702051 (2007).
- [9] L. Bergström and A. Goobar, Cosmology and Particle Astrophysics. (in *Springer-Praxis books in astronomy and astrophysics, Praxis Publishing Ltd, Chichester, UK*, 2004, 2nd ed.), p. 59.
- [10] A. A. Penzias and R. W. Wilson, A Measurement of Excess Antenna Temperature at 4080 Mc/s. *Astrophys. J.* **142**, 419 (1965).
- [11] G.F Smoot et al., Structure in the COBE differential microwave radiometer first-year maps. *Astrophys. J. Lett.* **396**, L1 (1992).
- [12] D. N. Spergel et al., Three-Year Wilkinson Microwave Anisotropy Probe (WMAP) Observations: Implications for Cosmology. *Astrophys. J. Suppl. Series* **170**, 377 (2007).

- [13] D. Clowe et al., A Direct Empirical Proof of the Existence of Dark Matter. *Astrophys. J. Lett.* **648**, L109 (2006).
- [14] M. Milosavljevi et al., The Cluster-Merger Shock in 1E 0657-56: Faster than a Speeding Bullet?. *Astrophys. J. Lett.* **661**, L131 (2007).
- [15] R. Trotta et al., Prospects for direct dark matter detection in the Constrained MSSM. *New Astron. Rev.* **51**, 316 (2007).
- [16] G.G. Raffelt, Axions - motivation, limits and searches. *J. of Phys. A Math. Gen.* **40**, 6607 (2007).
- [17] N. Fornengo, Status and Perspectives of Indirect and Direct Dark Matter Searches. (in *36th COSPAR Scientific Assembly*, Vol. 36 of *COSPAR, Plenary Meeting*, 2006), p. 1299.
- [18] F. Pröbst et al., Limits on WIMP dark matter using scintillating CaWO_4 cryogenic detectors with active background suppression. *Astropart. Phys.* **23**, 325 (2005).
- [19] L. Baudis et al., First results from the Heidelberg dark matter search experiment. *Phys. Rev. D* **63**, 022001 (2001).
- [20] L. Baudis et al., Improved constraints on wimps from the international germanium experiment IGEX. *Phys. Lett. B* **532**, 8 (2002).
- [21] I. Abt et al., Das GERDA-Experiment zur Suche nach neutrinolosem Doppelbetazerfall. <http://www.mpg.de/bilderBerichteDokumente/dokumentation/jahrbuch/2007/physik/forschungsSchwerpunkt/pdf.pdf> (08/2007) (2006).
- [22] The UK Dark Matter Collaboration, Limits on WIMP cross-sections from the NAIAD experiment at the Boulby Underground Laboratory. *Phys. Lett. B* **616**, 17 (2005).
- [23] R. Bernabei, Results on Dark Matter and $\beta\beta$ Decay Modes by DAMA at Gran Sasso. arXiv:0704.3543 v2 (2007).
- [24] H.S. Lee et al., Limits on WIMP-nucleon cross section with CsI(Tl) crystal detectors. arXiv:0704.0423 (2007).
- [25] Xinjie Qiu, An overview and current status of Cryogenic Dark Matter Search (CDMS) experiment. http://cdms.berkeley.edu/conference_talks_links/APS_Apr07-Qiu.pdf (2007).
- [26] D.S. Akerib et al., Limits on spin-dependent WIMP-nucleon interactions from the Cryogenic Dark Matter Search. *Phys. Rev. D* **73**, 011102 (2006).

- [27] M. LUCA, Status and Outlook of the EDELWEISS WIMP Search. arXiv:astro-ph/0605496 (2006).
- [28] V. Sanglard for the EDELWEISS collaboration, EDELWEISS-II : Status and future. arXiv:astro-ph/0612207 (2006).
- [29] L. Torres et al., Recent developments on scintillating bolometers for WIMP searches: ROSEBUD status. (in *TAUP 2005: Proc. Ninth Int. Conf. on Topics in Astroparticle and Underground Physics*, Vol. 39 of *J Phys.: Conference Series*, 2006), p. 133.
- [30] M.L. Sarsaa et al., The ROSEBUD experiment at Canfranc : 2001 report. Nucl. Phys. B Proc. Suppl. **110**, 97 (2002).
- [31] F. Proebst et al., Results and plans of the CRESST dark matter search. arXiv:astro-ph/0106314 (2001).
- [32] B. Majorovits et al., The CRESST Dark Matter Search. (in *The Identification of Dark Matter, Proceedings of the 5th International Workshop, Edinburgh, UK, World Scientific Publishing Company, Singapore*, 2005), p. 212.
- [33] J. Jochum, Cryogenic Detectors - Direct Dark Matter Search. Low-energy Astroparticle Underground Neutrino physics and Cosmology in Heidelberg (2007).
- [34] Y. Takeuchi, Recent Status of the XMASS Project. (in *ICHEP 2004*, Vol. I of *Proceedings of the 32nd International Conference on High Energy Physics, Beijing, China*, 2004), p. 324.
- [35] N. Smith et al., First limits on WIMP nuclear recoil signals in ZEPLIN-II: a two phase xenon detector for dark matter detection. arXiv:astro-ph/0701858v2 (2007).
- [36] K. Ni et al., First Results from the XENON10 Dark Matter Experiment at the Gran Sasso National Laboratory. arXiv:0706.0039v1 (2007).
- [37] L. Baudis, The XENON10 WIMP Search Experiment at the Gran Sasso Underground Laboratory. J. Phys. Conf. Series **65**, 2015 (2007).
- [38] C. Montanari et al., First results from a Dark Matter search with liquid Argon at 87 K in the Gran Sasso Underground Laboratory. arXiv:astro-ph/0701286v2 (2007).
- [39] J.-C. Lanfranchi, Development of a New Composite Cryogenic Detection Concept for a Radiochemical Solar Neutrino Experiment, PhD thesis, Technische Universität München, 2005.

- [40] T. Lachenmaier, Messung mit untergrundarmen Temperaturdetektoren zum hocheffizienten Nachweis des ^{71}Ge -Zerfalls, PhD thesis, Technische Universität München, 2005.
- [41] F. Pröbst et al., Model for cryogenic particle detectors with superconducting phase transition thermometers. *J. Low Temp. Phys.* **100**, 69 (1995).
- [42] K. Pretzl, Cryogenic calorimeters in astro and particle physics. *Nucl. Instr. Meth. A* **454**, 114 (2000).
- [43] G. Wendin and V.S. Shumeiko, Superconducting Quantum Circuits, Qubits and Computing. arXiv:cond-mat/0508729 v1 (2005).
- [44] G. Angloher et al., Limits on WIMP dark matter using sapphire cryogenic detectors. *Astropart. Phys.* **18**, 43 (2002).
- [45] (2006).
- [46] P. Meunier et al., Discrimination between nuclear recoils and electron recoils by simultaneous detection of phonons and scintillation light. *Appl. Phys. Lett.* **75**, 1335 (1999).
- [47] L. Stodolsky et al., Interpretation of Light-Quenching Factor Measurements. arXiv:0707.0766 (2007).
- [48] J. Ninković et al., New technique for the measurement of the scintillation efficiency of nuclear recoils. *Nucl. Instr. Meth. A* **564**, 567 (2006).
- [49] T. Jagemann et al., Neutron scattering facility for the measurement of nuclear recoil quenching factors. *Nucl. Instr. Meth. A* **551**, 245 (2005).
- [50] C. Coppi et al., Quenching factor measurement for CaWO_4 by neutron scattering. *Nucl. Instr. Meth. A* **559**, 396 (2006).
- [51] W. Westphal et al., Characterization of the Response of CaWO_4 on Recoiling Nuclei from Surface Alpha Decays. (in *LTD 12: Proc. 12th Int. Conf. on Low Temperature Detectors, to be published in J. Low Temp. Phys.* 2007).
- [52] H. Wulandari et al., Neutron Background Studies for the CRESST Dark Matter Experiment. arXiv:hep-ex/0401032v1 (2004).
- [53] R. C. Richardson and E. N. Smith, Experimental Techniques in Condensed Matter Physics at Low Temperatures. (in *Front. Phys.*, 1989), Vol. 67, p. 5.
- [54] <http://www.cresst.de/facility.php>, 09.08.2007.

- [55] R. Bernabei et al., Search for WIMP annual modulation signature: results from DAMA/NaI-3 and DAMA/NaI-4 and the global combined analysis. *Phys. Lett. B* **480**, 23 (2000).
- [56] A. Benoit et al., Improved exclusion limits from the EDELWEISS WIMP search. *Phys. Lett. B* **545**, 43 (2002).
- [57] D.S. Akerib et al., First Results from the Cryogenic Dark Matter Search in the Soudan Underground Laboratory. *Phys. Rev. Lett.* **93**, 211301 (2004).
- [58] CRESST collaboration, Recent developments on scintillating bolometers for WIMP searches: ROSEBUD status. (in *TAUP 2007: Proc. Tenth Int. Conf. on Topics in Astroparticle and Underground Physics, to be published*, 2007).
- [59] Kaixuan Ni, First Results from the XENON10 Dark Matter Experiment at the Gran Sasso National Laboratory. arXiv:[astro-ph]/0706.0039v1 (2007).
- [60] E. A. Baltz and P. Gondolo, Markov Chain Monte Carlo Exploration of Minimal Supergravity with Implications for Dark Matter. *J. High En. Phys.* **10**, 52 (2004).
- [61] H. Kraus et al., EURECA – the European future of cryogenic dark matter searches. *J. Phys. Conf. Series* **39**, 139 (2006).
- [62] E. Lassner and W.-D. Schubert, Tungsten - Properties, Chemistry, Technology of the Element, Alloys, and Chemical Compounds. (in *Kluwer Academic/Plenum Publishers, New York*, 1999), p. 1.
- [63] C. Cozzini et al., Detection of the natural α decay of tungsten. *Phys. Rev. C* **70**, 064606 (2004).
- [64] T. R. Waite et al., Heat Capacity of Tungsten between 4 and 15°K. *Phys. Rev.* **104**, 1240 (1956).
- [65] W. T. Berg, Heat Capacity of Aluminum between 2.7 and 20°K. *Phys. Rev.* **167**, 583 (1968).
- [66] S. M. Rossnagel et al., Phase transformation of thin sputter-deposited tungsten films at room temperature. *J. Vac. Sci. Technol.* **B 20**, 2047 (2002).
- [67] S. Basavaiah and S. R. Pollack, Superconductivity in β -Tungsten Films. *J. Appl. Phys.* **39**, 5548 (1968).
- [68] P. Petroff et al., Microstructure, growth, resistivity, and stresses in thin tungsten films deposited by rf sputtering. *J. Appl. Phys.* **44**, 2545 (1973).

- [69] P. Collot et al., Physicochemical properties in tungsten films deposited by radio-frequency magnetron sputtering. *J. Vac. Sci. Technol.* **6**, 2319 (1988).
- [70] K. L. Chopra et al., Face-centered-cubic tungsten films obtained by. *Appl. Phys. Lett.* **9**, 402 (1966).
- [71] A. E. Lita et al., Tuning of tungsten thin film superconducting transition temperature for fabrication of photon number resolving detectors. *IEEE trans. appl. supercond.* **15**, 3528 (2005).
- [72] G. M. Mikhailov et al., The effect of growth temperature on electrical conductivity and on structure of thin refractory metal films, grown by laser ablation deposition. *Thin Solid Films* **293**, 315 (1997).
- [73] B. A. Gurovich et al., Controlled ion-beam transformation of electrical, magnetic, and optical materials properties. *Uspekhi Fizicheskikh Nauk* **44**, 95 (2001).
- [74] M. Tinkham, Introduction to superconductivity. (in *Dover Publications, Mineola, New York*, 2004, ed. 2), p. 43.
- [75] B. Lorenz and C. W. Chu, High Pressure Effects on Superconductivity. (in *Frontiers in Superconducting Materials, Springer Berlin Heidelberg*, 2005), p. 459.
- [76] B. A. Young et al., T_c tuning of tungsten transition edge sensors using iron implantation. *Nucl. Instr. Meth. A* **444**, 296 (2000).
- [77] B. A. Young et al., Measurement of T_c suppression in tungsten using magnetic impurities. *J. Appl. Phys.* **86**, 6975 (1999).
- [78] T. J. Vink et al., Stress, strain, and microstructure in thin tungsten films deposited by dc magnetron sputtering. *J. Appl. Phys.* **74**, 988 (1993).
- [79] D. V. SHOPOVA et al., Gauge effects on phase transitions in superconductors. arXiv:cond-mat/0611354v3 (2006).
- [80] S. M. Rossmagel, Sputter deposition for semiconductor manufacturing. *IBM J. Res. Develop.* **43**, 1 (1999).
- [81] E. Hofmann, *Supraleitende Filme als Detektorkomponenten in der Astro-Teilchenphysik*, 2005.
- [82] C. Isaila, Private communication, 2007.
- [83] C. Isaila et al., Application of the Neganov-Luke Effect for Scintillation Light Detection. (in *LTD 12: Proc. 12th Int. Conf. on Low Temperature Detectors, to be published in J. Low Temp. Phys.*2007).

- [84] M. Kiefer, Optimierung szintillierender Tieftemperaturkalorimeter für den direkten Nachweis von Teilchen der Dunklen Materie, Diploma thesis. Bayerische Julius-Maximilians-Universität Würzburg, Max-Planck-Institut für Physik München (2007).
- [85] P. N. Luke, Voltage-assisted calorimetric ionization detector. *J. Appl. Phys.* **64**, 6858 (1988).
- [86] C. Ciemniak, Czochralski Growth of Calcium Tungstate Crystals for the CRESST Experiment, Talk at CryoScint 2007, Lyon, 2007.
- [87] W. Westphal, PhD thesis in preparation, Technische Universität München, 2007.
- [88] M. Stark, Detektoren mit effizienter und schneller Phononensammlung für das CRESST Experiment, PhD thesis, Technische Universität München, 2005.
- [89] J. Schnagl, Entwicklung von Lichtdetektoren mit Phononenkollektoren für das CRESST Experiment, PhD thesis, Technische Universität München, 2001.
- [90] M. Stark et al., Detectors with Ir/Au-thermometers for high count rate tests in the CRESST experiment. *Nucl. Instr. Meth. A* **520**, 197 (2004).

Acknowledgements

An erster Stelle will ich mich bei Herrn Prof. Dr. Franz von Feilitzsch für die überaus freundliche Aufnahme an seinen Lehrstuhl und die interessante Aufgabenstellung danken.

Mein besonderer Dank gilt Herrn Dr. Walter Potzel für unzählige Diskussionen und seine scheinbar unerschöpfliche Fähigkeit, mich immer wieder mit Fragen zu konfrontieren, so dass ich mir über die Korrektheit diverser Hypothesen immer wieder klar werden konnte. Ohne seine unermüdlichen Korrekturen wäre diese Arbeit nicht zu dem geworden, was sie ist.

Bei meinem Betreuer, Dr. Jean-Côme Lanfranchi, möchte ich mich herzlich für seine stete Bereitschaft zu helfen, zu diskutieren und zu erklären, wo auch immer es möglich war, bedanken. Ich möchte ihm ebenfalls für die geduldige Korrektur meiner Arbeit danken.

Ebenso danke ich Prof. Dr. Lothar Oberauer für die Einführung in die Astroteilchen Physik, die mir unter anderem die WIMPs erstmals näher brachte. Ohne die handwerkliche Unterstützung durch das Institutswerkstatt-Team, Harald Hess, Erich Seitz und Thomas Richter, und die Beratung elektronische Fragestellungen betreffend durch Herrn Dipl.-Ing. Hermann Hagn wäre diese Arbeit nicht möglich gewesen. Bei Herrn Norbert Gärtner möchte ich mich für die Unterstützung in Sicherheitsfragen sowie im speziellen für seine Hilfe, wenn es wieder einmal um Vakuumpumpen ging, bedanken. Dr. Andreas Erb und dem Team des Kristalllabors will ich für die Durchführung und Diskussion meiner Theta-2-Theta Messungen danken.

Bei Sebastian Pfister möchte ich mich für nunmehr sechs Jahre des gemeinsamen Studierens und nun auch Zusammenarbeitens bedanken. Ihm verdanke ich die Einführung in den Umgang mit unter anderem der Sputteranlage und den dazugehörigen Vakuumanlagen. Wolfgang Westphal möchte ich für seine stete Hilfsbereitschaft und Geduld danken, ob es nun um einen Cool-Down oder die Diskussion theoretischer Fragen zu Detektoren und ihrer Funktionsweise ging. Bei Christian Isaila möchte ich mich -neben vielen anderen Sachen- im speziellen auch für die Einführung in die Kunst des Bondens auf Wolfram bedanken.

Allen Mitgliedern des Lehrstuhls danke ich für die herzliche Atmosphäre und die vielen netten Kaffeepausen und Diskussionen. Im speziellen gilt mein Dank Beatrice van Bellen und Alexandra Földner für die schier grenzenlose Geduld, wenn es um das Ausfüllen diverser Formulare ging, und für die Versorgung mit der nötigen Ausstattung für die Kaffeepausen.

Einen ganz speziellen Dank möchte ich meiner Familie und insbesondere meinen Eltern aussprechen, dafür, daß sie mich immer bei der Verfolgung meiner Ziele unterstützt haben und permanent hinter mir standen.
